DEVELOPMENT OF NEW ACQUISITION STRATEGIES FOR FAST PARAMETER QUANTIFICATION IN MAGNETIC RESONANCE IMAGING

15 83

Dissertation zur Erlangung des
Naturwissenschaftlichen Doktorgrades
der Julius-Maximilians-Universität Würzburg

vorgelegt von
Philipp Ehses
aus Bonn

Würzburg, Dezember 2011

EINGEREICHT AM: 14. Dezember 2011

BEI DER FAKULTÄT FÜR PHYSIK UND ASTRONOMIE

1. GUTACHTER: Prof. Dr. Peter M. Jakob

2. GUTACHTER: Prof. Dr. Dr. Wolfgang Bauer

DER DISSERTATION.

1. PRÜFER: Prof. Dr. Peter M. Jakob

2. PRÜFER: Prof. Dr. Björn Trauzettel

IM PROMOTIONSKOLLOQUIUM.

TAG DES PROMOTIONSKOLLOQUIUMS: 11. Juni 2012

DOKTORURKUNDE AUSGEHÄNDIGT AM:

CONTENTS

---

1 INTRODUCTION 7

1.1 Magnetic Resonance Imaging 7

1.2 Fast MRI Relaxometry 8

1.3 MRI Thermometry for Implant Safety Investigations 8

2 BASIC PRINCIPLES OF MRI 11

2.1 Nuclear Magnetic Resonance 11

2.2 Bloch Equations and Signal Decay 12

2.3 Spatial Encoding using Magnetic Field Gradients 13

2.3.1 Slice Selection 14

2.3.2 Frequency Encoding 14

2.3.3 Phase Encoding 15

2.3.4 K-space formalism 15

2.4 Pulse Sequences 17

2.4.1 Basic Gradient Echo 17

2.4.2 Balanced Steady-State Free Precession (bSSFP) 18

2.5 Projection reconstruction 22

2.5.1 The Radial Trajectory 23

2.5.2 Image reconstruction 23

I Fast MRI Relaxometry 27

3 IR TRUEFISP WITH A GOLDEN-RATIO BASED RADIAL READOUT 29

3.1 Introduction 29

3.2 Theory 31

3.2.1 IR TrueFISP-based Parameter Estimation 31

3.3 Methods 32

3.3.1 Development of a Radial bSSFP Sequence 32

3.3.2 Centering the Radial Trajectory 33

3.3.3 Golden-ratio based profile order 37

3.3.4 Image reconstruction using a modified k-space weighted image contrast (KWIC) filter 37

3.3.5 Imaging experiments 40

3.3.6 Signal Processing and Parameter Fitting 41

3.4 Results 42

3.5 Discussion 45

3.6 Conclusion 48

4 SLICE PROFILE AND MAGN. TRANSFER EFFECTS ON IR TRUEFISP RELAXOMETRY 49
- 4.1 Introduction 49
- 4.2 Theory 50
  - 4.2.1 Slice profile effects 50
  - 4.2.2 Magnetization transfer effects 51
- 4.3 Methods 52
  - 4.3.1 Imaging experiments 52
  - 4.3.2 Signal Processing and Parameter Fitting 54
- 4.4 Results 55
- 4.5 Discussion 59
- 4.6 Conclusion 62

II Dynamic MRI Thermometry 65

5 DYNAMIC MRI THERMOMETRY DURING RF HEATING 67
- 5.1 Introduction 67
- 5.2 Theory 68
  - 5.2.1 Specific Absorption Rate (SAR) 68
  - 5.2.2 Amplification of Local SAR by Conductive Implants 69
  - 5.2.3 Basic Principles of MRI Thermometry 69
  - 5.2.4 Thermometry based on the water proton resonance frequency (PRF) 70
- 5.3 Methods 71
- 5.4 Results 74
- 5.5 Discussion 76
- 5.6 Conclusion 78

6 IMPROVED MRI THERMOMETRY AND APPLICATION TO 3D 79
- 6.1 Introduction 79
- 6.2 Methods 79
- 6.3 Results 82
- 6.4 Discussion and Conclusion 83

SUMMARY 85

ZUSAMMENFASSUNG 89

III Appendix 93

BIBLIOGRAPHY 95

LIST OF FIGURES 103

LIST OF TABLES 108

CURRICULUM VITAE 111

LIST OF PUBLICATIONS 113

1

INTRODUCTION

> *I have not yet lost a feeling of wonder, and of delight, that this delicate motion should reside in all the things around us, revealing itself only to him who looks for it. I remember, in the winter of our first experiments, just seven years ago, looking on snow with new eyes. There the snow lay around my doorstep - great heaps of protons quietly precessing in the earth's magnetic field. To see the world for a moment as something rich and strange is the private reward of many a discovery.*
>
> — Edward Mills Purcell, Nobel Lecture

1.1 MAGNETIC RESONANCE IMAGING

Magnetic resonance imaging (MRI) is a very versatile imaging modality. Since the MRI signal is dependent on various physical properties of the object being imaged, it provides a wide range of contrast mechanisms, and even the possibility to non-invasively quantify the underlying parameters. The most common contrast mechanisms used in clinical routine depend on MRI-related parameters, namely proton density, which is directly proportional to the water content of the tissue being imaged, as well as longitudinal (T_1) and transversal (T_2, T_2^*) relaxation. Furthermore, it is possible to encode various other physical phenomena in the MRI signal, that seem - at first glance - to be unrelated to MRI: for instance, the velocity of blood flow (e.g. in cardiac MRI) is frequently measured using flow-encoding gradient waveforms. The apparent diffusion coefficient (ADC) can be similarly determined using diffusion-encoding gradients, allowing the tracking of nerve fibers in the brain. In recent years, functional MRI (fMRI) has become increasingly popular in Neuroscience. fMRI detects neural activity by observing local magnetic field changes caused by a change in blood oxygenation (using the blood oxygenation level dependent (BOLD) effect). Additionally, relative and absolute temperature values can be determined by observing changes in the proton resonance frequency, relaxation times, diffusion constant, or other MR related temperature-dependent parameter. In fact, ignoring the signal-to-noise ratio and acquisition time as limiting factors, it is difficult to find *any* macroscopic physical phenomena in aqueous objects that is not within reach of quantification with MRI.

This thesis is divided into two parts; part 1: *Fast MRI Relaxometry* and part 2: *Dynamic MRI Thermometry.* A short motivation to these topics is provided in the following.

1.2 FAST MRI RELAXOMETRY

With the possible exception of cardiovascular blood flow velocity mapping, most of the quantitative techniques mentioned in the previous section have not yet found wide clinical application and are mostly restricted to research studies. Even the mapping of MRI-specific parameters such as T_1 and T_2, which are the basis of most of the contrast used in clinical settings, is not performed routinely. The main reason for this is the long scan time required to accurately map the parameter in question with sufficient resolution. Long scan times directly translate to high costs and reduced patient comfort, and significantly increase the likelihood of severe artifacts due to patient motion. Therefore, the acceleration of quantitative MRI methods is of major interest and essential for wider clinical adoption.

MRI relaxometry involves pixel-wise mapping of proton density, longitudinal relaxation time T_1, and/or transverse relaxation time T_2 (or other relevant parameters) at each location in the tissue to be characterized. There has been significant recent interest in this topic, as it allows one to evaluate pathology using absolute tissue characteristics. In addition, it has long been recognized that, if these parameters can be mapped in a time-efficient manner, theoretically images of any desired contrast could be retrospectively generated.

The aim of this study was to improve a promising MRI relaxometry method that was originally developed here at the Department for Experimental Physics 5 by Peter Schmitt et al.. This technique, the *IR TrueFISP* method allows one to simultaneously quantify proton density, T_1 and T_2 in a single scan. Improvements in speed and accuracy are presented that may help to bring MRI relaxometry closer to clinical adoption.

1.3 MRI THERMOMETRY FOR IMPLANT SAFETY INVESTIGATIONS

With an increasing number of patients with metallic implants and a simultaneously growing number of MRI examinations, development of MRI-safe implants has become increasingly important. Today, MRI examinations of patients with medical implants such as cardiac pacemakers, implantable cardioverter-defibrillators (ICD), or deep brain stimulators are contraindictated in most cases due to associated risks. This prevents a growing number of patients from benefitting from advances in MRI diagnosis.

One of the major safety risks associated with MRI examinations of pacemaker and ICD patients is RF induced heating of the pacing electrodes that lead to the cardiac muscle. Severe heating of the tips of the electrodes can cause burns in cardiac tissue that may result in a transient or permanent increase of the pacing thresholds. Understanding these heating effects is crucial for the development of MRI-safe devices.

Currently, these heating effects can only be observed *in vitro* or in an animal model with the help of a temperature probe.

The aim of this study was to develop an MRI thermometry method that can be used in safety testing environments for the noninvasive monitoring of the heating of metallic implants during MRI examinations.

2

BASIC PRINCIPLES OF MRI

> *In this house, we obey the laws of thermodynamics!*
>
> — Homer Simpson

This chapter will give a short overview of MRI, with the emphasis on topics relevant to this work. For a more complete review see [1, 2].

2.1 NUCLEAR MAGNETIC RESONANCE

Nuclear Magnetic Resonance (NMR) is the underlying phenomenon behind MRI. It was first described in 1946 independently by Felix Bloch and Edward Purcell [3, 4]. NMR can be observed whenever a nucleus possessing non-zero angular momentum is placed into a magnetic field. The magnetic moment $\vec{\mu}$ of a nucleus can be described as

$$\vec{\mu} = \gamma\vec{\mathrm{S}} \tag{2.1}$$

where $\vec{S}$ stands for the spin of the nucleus and the parameter γ is known as the gyromagnetic ratio, specific to the nucleus in question ($\bar{\gamma} = \gamma/2\pi \approx 42.57$ MHz/T for protons). Spin 1/2 systems (such as ^1H, ^{13}C, ^{15}N, ^{19}F, or ^{31}P) will seek to align their spin either parallel (spin up) or anti-parallel (spin down) to the external field, thereby creating two distinct energy levels:

$$E_\uparrow = -\frac{1}{2}\gamma\hbar B_0 \tag{2.2}$$

$$E_\downarrow = +\frac{1}{2}\gamma\hbar B_0 \tag{2.3}$$

where $E_\uparrow$, $E_\downarrow$ denote the energy levels corresponding to the spin up and spin down state, respectively, $\hbar$ is Planck's constant divided by 2π, and B_0 is the absolute strength of the main magnetic field. Here and below, by convention and without loss of generality, the main magnetic field is always pointed in the z-direction.

The energy difference between the two states is then given by

$$\Delta E = E_\downarrow - E_\uparrow = \gamma\hbar B_0 \tag{2.4}$$

In thermal equilibrium, the relative population of the two spin states is governed by the Boltzmann distribution, according to

$$\frac{N_\uparrow}{N_\downarrow} = \exp\left(\frac{\Delta E}{kT}\right) = \exp\left(\frac{\gamma \hbar B_0}{kT}\right) \tag{2.5}$$

with the population of the two spin states $N_\uparrow$ and $N_\downarrow$, the Boltzmann constant $k = 1.38 \times 10^{-23} J/K$, and the temperature of the spin system T. The population difference of these states is usually very small, on the order of 1 ppm at room temperature and for common field strengths ($B_0 \approx 1\,T$).

This phenomenon of energy splitting is called the Zeeman effect [5]. A transition between the two states can be induced by application of a radio-frequency pulse of the characteristic resonance frequency, known as the Larmor frequency:

$$\omega_0 = \gamma B_0 \tag{2.6}$$

Electrons in the molecular orbitals effectively shield the magnetic field to varying degrees, depending on the position of the nucleus in the molecule. As a result, the Larmor frequency of the nucleus under investigation is slightly shifted

$$\omega_0 = \gamma B_0 \left(1 - \delta\right) \tag{2.7}$$

where δ is a shielding constant, known as the *chemical shift*. Therefore, by observing the NMR frequency spectrum of a sample, it is possible to gain knowledge of its chemical composition and structure. This method, known as *NMR spectroscopy* was the first major application of NMR.

2.2 BLOCH EQUATIONS AND SIGNAL DECAY

The bulk magnetization of an object can be described by the vector sum of all the microscopic magnetic moments of its constituents:

$$\vec{M} = \sum_{n=1}^{N_s} \vec{\mu}_n \tag{2.8}$$

where N_s is the total number of spins in the object, and $\vec{\mu}_n$ represents the magnetic moment of the nth nuclear spin. A classical description of the time evolution of $\vec{M}$ is given by the *Bloch equation* [3] (here in its simplest form):

$$\frac{d\vec{M}}{dt} = \gamma \vec{M} \times \vec{B}$$

This equation describes the effect of an applied RF field $\vec{B}$ on the spin-system. In the case of RF excitation, the resulting measurable signal is called the *free induction decay (FID)*. Extending this equation to account for relaxation yields the more general form of the Bloch equation

$$\frac{d\vec{M}}{dt} = \gamma \vec{M} \times \vec{B} - \frac{M_x\vec{i} + M_y\vec{j}}{T_2} - \frac{(M_z - M_0)\vec{k}}{T_1} \tag{2.9}$$

where T_1 and T_2 stand for the time constants of longitudinal and transverse relaxation, respectively, and $\vec{i}$, $\vec{j}$, $\vec{k}$ are unit vectors in x, y, and z direction, respectively. Many additional extensions to the Bloch equation have been proposed, e.g. a term to describe diffusion effects can be included, yielding the popular *Bloch-Torrey equation* [6].

2.3 SPATIAL ENCODING USING MAGNETIC FIELD GRADIENTS

According to Equation 2.6, the Larmor frequency is linearly dependent on the strength of the magnetic field. Thus, by applying a magnetic field gradient along a specific direction, the precession frequencies of the nuclear spins can be directly related to their positions along that direction. A typically used linear gradient has the form

$$G_x = \frac{dB_z}{dx} \tag{2.10}$$

where G_x refers to the gradient strength in x-direction. Together with the static main magnetic field B_0, this results in the following spatially-dependent Larmor frequency

$$\omega_0(x) = \gamma\,(B_0 + xG_x) \tag{2.11}$$

The dependencies in Equation 2.11 highlight the need for a high homogeneity of the main magnetic field (compared to the strength of the magnetic field gradient). Furthermore, the similarity to Equation 2.7 is striking. Therefore, for accurate spatial encoding, the magnetic field gradient also has to be strong compared to chemical shift as well as susceptibility differences that may be present in the object of interest.

2.3.1 *Slice Selection*

Spectrally selective RF pulses can be used to selectively excite certain spin species with a Larmor frequency that lies inside the bandwidth of the pulse. By applying a magnetic field gradient of the form 2.10 (although it can point in an arbitrary direction, the z-direction is assumed in the following) simultaneously with the RF pulse, it is possible to use this spectral selectivity of the RF pulse for *spatially selective* excitation: Assuming a single spin species (e.g. only proton spins of water), according to Equation 2.11, the frequency of the RF pulse only matches the resonance frequency of spins that lie inside a slice, with a thickness Δz which depends on the strength of the gradient G_z and the bandwidth of the pulse Δf:

$$\Delta z = \frac{2\pi \Delta \mathrm{f}}{\gamma G_z} \tag{2.12}$$

When there is more than one spin species (e.g. fat and water), their corresponding slice positions may be slightly shifted due to the chemical shift. This effect can be reduced by increasing the bandwidth of the pulse (requiring an increase of the amplitude of the slice selection gradient when Δz is held constant).

2.3.2 *Frequency Encoding*

By using a linear field gradient during the acquisition of the MR signal, the Larmor frequency of the activated MR signal is, according to Eq. 2.11, linearly dependent on its spatial origin. Assuming the gradient was applied along x-direction, the signal received from the entire object is modulated by the gradient as follows:

$$S(t) = \int_{\text{object}} dS(x,t) = \int_{-\infty}^{\infty} \rho(x)\, e^{-i\gamma(B_0 + xG_x)t} dx = \left[\int_{-\infty}^{\infty} \rho(x)\, e^{-i\gamma G_x x t} dx\right] \mathrm{e}^{-i\omega_0 t} \tag{2.13}$$

This equation is known as the one-dimensional imaging equation. The term $\mathrm{e}^{-i\omega_0 t}$ denotes the carrier frequency, and this equation can be simplified by moving to the rotating frame (i.e. demodulation of the acquired signal by the frequency induced by the main magnetic field):

$$dS(x,t) = \rho(x)\, e^{-i\gamma G_x x t} \tag{2.14}$$

The spatial origin of the signal is now encoded in the time-dependent phase term $\mathrm{e}^{-i\gamma G_x x t}$.

2.3.3 *Phase Encoding*

The principle of phase encoding is very similar to frequency encoding. When, after RF excitation and before signal acquisition, a gradient G_y is turned on for a short interval T_{PE}, the local signal after application of this gradient, observed in the rotating frame, is given by

$$dS(y) = \rho(y)\, e^{-i\gamma G_y y T_{PE}} \tag{2.15}$$

As a result, spins from different positions in the object accumulate different phase angles ϕ

$$\phi(y) = -\gamma G_y y T_{PE} \tag{2.16}$$

This phase modulation can be considered independent of other gradients applied in perpendicular direction during the imaging experiment, making it possible to combine phase encoding with frequency encoding or with itself, applied in multiple directions.

The similarity between equations 2.14 and 2.15 is striking. However, unlike in frequency encoding, where the phase is continuously modulated by a gradient during readout, only a single phase shift can be obtained in one acquisition period. Therefore, in order to obtain enough information for image reconstruction, the experiment has to be repeated with different phase modulations, by altering either the amplitude G_y or the amount of time T_{PE} the phase encoding gradient is applied. Usually, for an image with N_y pixels in phase encoding direction, the experiment has to be repeated the same number of times. This requirement is one of the main reasons for the long scan times that are associated with MR imaging.

2.3.4 *K-space formalism*

The k-space concept, as first introduced by Twieg [7], greatly simplifies the description of gradient encoding in MRI.

According to the one-dimensional imaging equation 2.13, the time-dependent signal (ignoring relaxation effects) during frequency encoding, observed in the rotating frame, can be expressed as

$$S(t) = \int_x \rho(x)\, e^{-i\gamma G_x x t} dx$$

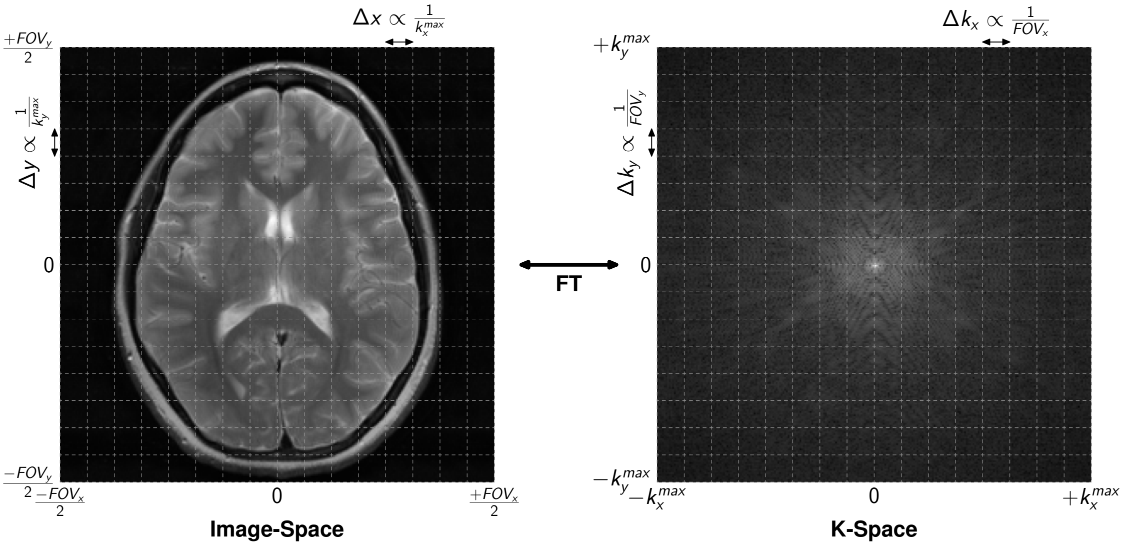
$\Delta x \propto \frac{1}{k_x^{max}}$
$\frac{+FOV_y}{2}$
$\Delta y \propto \frac{1}{k_y^{max}}$
0
$\frac{-FOV_y}{2}$
$\frac{-FOV_x}{2}$
0
$\frac{+FOV_x}{2}$
Image-Space
FT
$\Delta k_x \propto \frac{1}{FOV_x}$
$+k_y^{max}$
$\Delta k_y \propto \frac{1}{FOV_y}$
0
$-k_y^{max}$
$-k_x^{max}$
0
$+k_x^{max}$
K-Space

Figure 1: A representation of the relationships between the image space and k-space domain. The field of view (FoV) of the image is proportional to the inverse of the distance between neighboring k-space points. If the chosen FoV becomes smaller than the object being imaged, i.e. the distance between k-space points becomes too high, aliasing occurs. The achievable resolution is proportional to the inverse of the maximum k-space point sampled.

Substituting $k_x = \frac{\gamma}{2\pi} G_x t = \bar{\gamma} G_x t$ results in

$$S(k_x) = \int_x \rho(x)\, e^{-i2\pi k_x x} dx \tag{2.17}$$

When frequency encoding is combined with phase encoding in y-direction (or more generally with spatial gradient encoding in multiple dimensions), Equation 2.17 takes vector form, resulting in the 2D (or 3D) imaging equation:

$$S(\vec{k}) = \int_{\text{object}} \rho(\vec{r})\, e^{-i2\pi \vec{k}\cdot\vec{r}} d\vec{r} \tag{2.18}$$

where $\vec{r}$ is the position vector and $\vec{k}$ is the k-space vector. This is the definition of the Fourier transform, showing that the signal $S(\vec{k})$ is given by the Fourier transform of the object's spin density (modulated by relaxation and/or other effects). Thus, the $\rho(\vec{r})$ can be obtained from the received signal by simply applying the inverse Fourier transform:

$$\rho(\vec{r}) = \int_{-\infty}^{\infty} S(\vec{k}) \cdot e^{2\pi i \vec{k}\cdot\vec{r}} d\vec{k} \tag{2.19}$$

Therefore, in order to obtain an image (i.e. determine $\rho(\vec{r})$) the inverse Fourier transform is applied to the acquired signal. Because it is not possible to infinitely sample $S(\vec{k})$, only discrete discrete points are sampled in this k-space.

Discrete sampling of k-space relies on several assumptions about the object being imaged: First, the distance between each acquired k-space point is inversely related to the size of the object (or the field-of-view (FoV)) that can be imaged without leading to undersampling (or fold-over) artifacts. This is known as the Nyquist criterion and is generally valid for signal sampling:

$$\text{FoV} \propto \frac{1}{\Delta k} \tag{2.20}$$

In Cartesian imaging, it is straightforward to choose different FoV sizes for each direction, by choosing corresponding values for $\Delta k_{x,y,z}$.

The second assumption is that the object does not contain smaller structures than can be resolved by the maximum acquired k-space value k_{max} (again, $k_{x,y,z}^{max}$ can be chosen independently). Specifically, the maximum achievable resolution in x direction Δx is inversely proportional to $k_{x,max}$:

$$\Delta \text{x} \propto \frac{1}{2k_{x,max}} \tag{2.21}$$

This assumption can always only be approximately fulfilled and its inevitable violation leads to a restriction on the achievable resolution, as well as possible Gibbs ringing due to the sharp cut at the edge of k-space.

The mentioned relations between image space and k-space are illustrated in Figure 1.

2.4 PULSE SEQUENCES

A multitude of pulse sequences have been proposed, which can generally be divided into spin-echo and gradient-echo type sequences (and combinations thereof). This work is exclusively focused on the gradient-echo-type described in the following section. For an extensive overview of commonly used pulse sequences see [2].

2.4.1 *Basic Gradient Echo*

The family of gradient echo sequences (or gradient-recalled echo, GRE) is primarily used for fast scanning [8], often in applications that require T_1 weighting. When rf-spoiling is employed [9, 10, 11], the GRE signal shows pure T_1 and T_2^* weighting.

Without (perfect) rf-spoiling, spin echoes contribute to the signal formation, causing some additional T_2 weighting.

The sequence timing of a basic 2D Cartesian GRE sequence is illustrated in Figure 2. As mentioned in section 2.3.3, this basic sequence kernel has to be repeated multiple times with different phase-encoding parameters in order to fully sample k-space in phase-encoding direction. The time interval between subsequent excitations is referred to as repetition time (TR). After spatially selective signal excitation, the slice rewinder gradient nulls the gradient moment that accumulated during application of the slice selection gradient. Simultaneously, the FID signal is spatially encoded in the phase-encoding direction and prepared for readout by the application of a readout prephasing gradient. During signal acquisition, the readout gradient rephases the spins, causing a gradient-echo in the center of the acquisition window, at the echo time TE. In order to avoid image artifacts due to remaining and improperly phase-encoded signal from previous TRs, the phase-encoding gradient has to be rewound prior to the next excitation. Often, in order to dephase any remaining transverse magnetization prior to the next excitation, a spoiler gradient is applied in the read encoding and/or slice selection direction. However, it is a common misconception that spoiler gradients *destroy* transverse magnetization – spoiled magnetization can and will eventually contribute to the signal at some later TR (assuming $T_2 \gg \mathrm{TR}$ and without strong diffusion weighting). The phase graph formalism and its extension [12, 13] are useful tools for keeping track of possible signal (and relaxation) pathways and for identifying individual contributions to the observed signal.

For an rf-spoiled GRE (or FLASH [8]) sequence, the steady-state signal at the position of the echo is given by the Ernst formula [14] (including an additional term that accounts for T_2^* decay):

$$S_{\text{rf-spoil}} = \frac{M_0 \sin\alpha \left(1 - e^{-\mathrm{TR}/T_1}\right)}{1 - \cos\alpha\, e^{-\mathrm{TR}/T_1}}\, e^{-TE/T_2^*} \tag{2.22}$$

The flip angle that maximizes the signal level for a given T_1 and TR is called the *Ernst angle* α_{Ernst}:

$$\alpha_{\text{Ernst}} = \arccos(e^{-\mathrm{TR}/T_1}) \tag{2.23}$$

2.4.2 *Balanced Steady-State Free Precession (bSSFP)*

The properties of the balanced steady-state free precession (bSSFP) signal in NMR were described in 1958 by Carr [15], but bSSFP imaging was not proposed until 1986 [16]. It took almost another 20 years until bSSFP became popular in the clinic. Currently, the bSSFP sequence is extensively used in cardiac imaging, where it offers

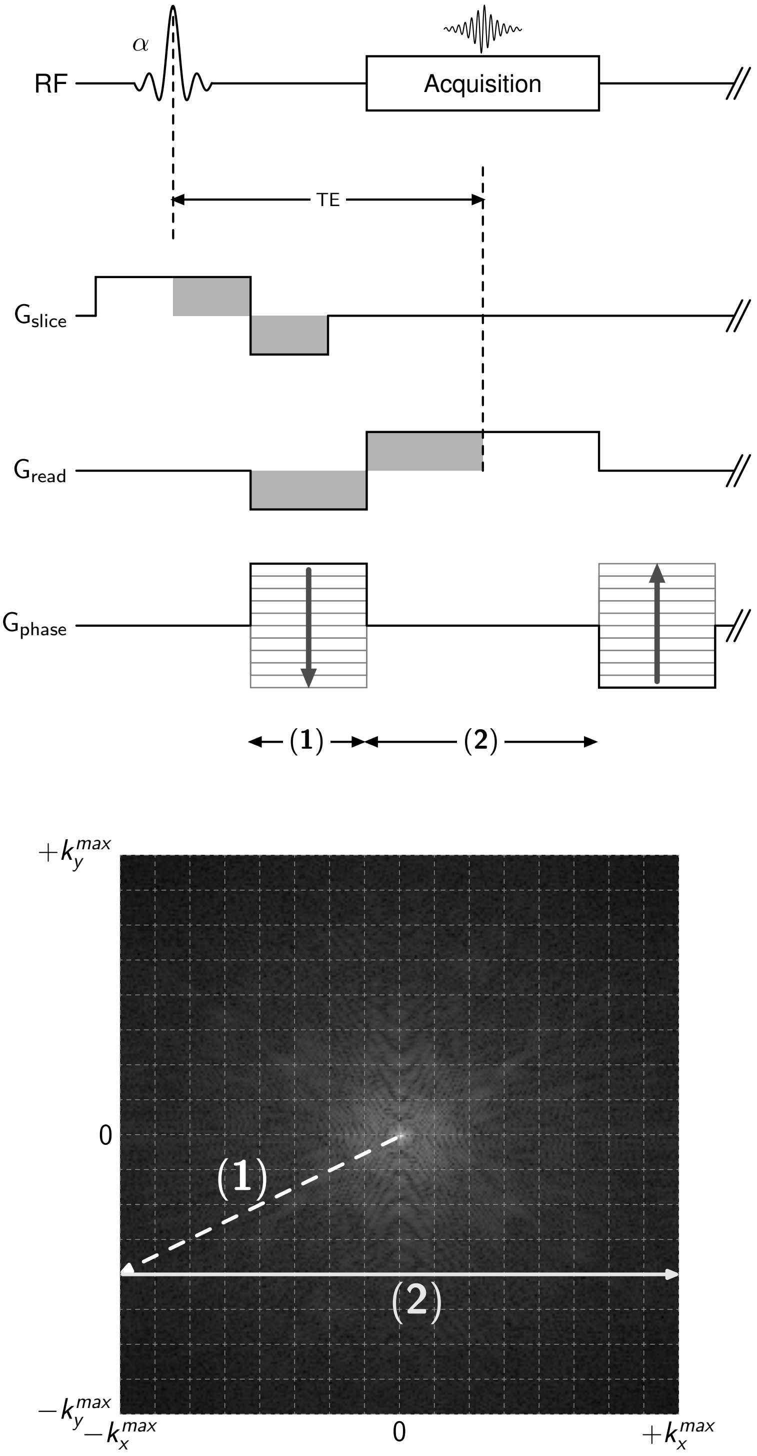
RF
α
Acquisition
TE
G_{slice}
G_{read}
G_{phase}
(1)
(2)
$+k_y^{max}$
0
$-k_y^{max}$
$-k_x^{max}$
0
$+k_x^{max}$
(1)
(2)

Figure 2: Top: Basic Cartesian 2D GRE sequence. Periods of phase-encoding and read dephasing are indicated by (1), the acquisition window by (2). Bottom: The spatial encoding scheme can also be understood by looking at the k-space trajectory: The phase-encoding and read dephasing gradients move the k-space vector to the beginning of a k-space line (1). During signal acquisition, the readout gradient moves the trajectory in k_x direction to the end of the current k-space line (2).

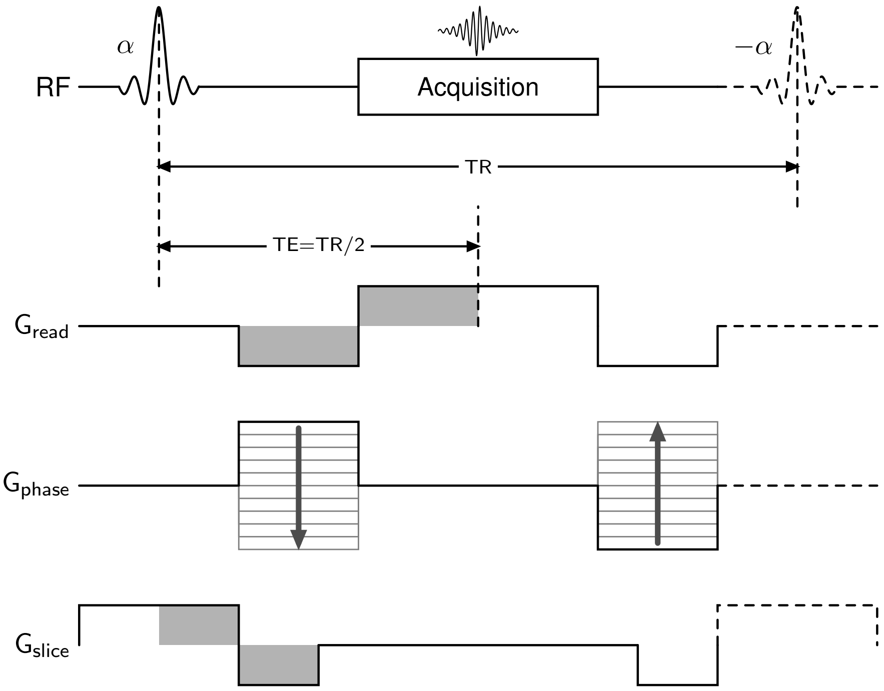

Figure 3: 2D Cartesian fully balanced steady-state free precession (bSSFP) sequence. Gradients on all axes are fully balanced in every TR.

fast, high-SNR scanning with a strong contrast between blood and myocardium. A good overview of bSSFP and its clinical applications is given by Scheffler and Lehnhardt [17]. bSSFP is also known under the names TrueFISP, balanced FFE, and FIESTA.

Like the basic gradient echo sequence, the bSSFP sequence consists of a series of excitation pulses that are separated by a repetition time TR. However, unlike in basic GRE, all imaging gradients are fully balanced in every TR and no spoiling is used, i.e. the net gradient moment at the end of the TR is zero on all gradient axes. Usually the excitation pulses are alternated between $\pm\alpha$, although other phase-cycling schemes are also possible. This creates a high steady-signal level for on resonant spins, which can reach up to 50% of M_0 in some cases. A diagram of a 2D Cartesian bSSFP sequence is shown in Fig. 3.

The steady-state signal of on resonant spins in an ideal bSSFP experiment can be described by

$$S_{\mathrm{bSSFP}} = \sqrt{E_2}\frac{M_0 \sin\alpha(1-E_1)}{1-(E_1-E_2)\cos\alpha - E_1E_2}, \quad \text{with } E_{1,2} = e^{-\mathrm{TR}/T_{1,2}} \qquad (2.24)$$

For TR $\ll T_{1,2}$, E_1 and E_2 can be approximated by the first two terms of the Taylor expansion:

$$E_{1,2} \approx 1 - \frac{\mathrm{TR}}{T_{1,2}} \tag{2.25}$$

Eq. 2.24 becomes

$$S_{\mathrm{bSSFP}} = \frac{M_0 \sin\alpha}{T_1/T_2 + 1 - (T_1/T_2 - 1)\,\cos\alpha} \tag{2.26}$$

For $\alpha = 90°$ this equation simplifies to

$$S_{\mathrm{bSSFP}} = M_0 \frac{T_2}{T_1 + T_2} \tag{2.27}$$

And assuming $T_1 \gg T_2$, we finally get

$$S_{\mathrm{bSSFP}} \approx M_0 \frac{T_2}{T_1} \tag{2.28}$$

This equation indicates that bSSFP images are T_2/T_1 weighted for high flip angles (close to 90°), and that the signal level is independent of TR (and TE), as long as the approximation TR $\ll T_{1,2}$ is valid. This also means that bSSFP shows high signal for tissues with long T_2 and short T_1 values, and explains the relative insensitivity of the bSSFP signal on the concentration of gadolinium based contrast agents: The relaxivity of gadolinium for T_1 and T_2 is very similar, causing an approximately constant T_2/T_1 ratio independent of the contrast agent's concentration. This effect is nicely demonstrated in [17]. Equation 2.27 also shows that the maximum possible signal level approaches 50% of M_0 for $T_2 \approx T_1$, which is extremely high for a short TR pulse sequence and explains the recent popularity of bSSFP.

Frequency Response of the bSSFP sequence

Until now, all considerations assumed that the spins are on-resonant, meaning that they have the same known frequency when no additional field gradients are applied. However, in contrast to spoiled gradient-echo sequences, bSSFP is very susceptible to off-resonances, which can occur due to main magnetic field inhomogeneity or susceptibility. The typical frequency response of bSSFP for different excitation flip angles is shown on the left side of Figure 4. The plot shows the transverse magnetization (i.e. the signal level) as a function of the off resonance angle, which is defined as the amount of dephasing a spin experiences during a TR. It can be seen that the signal level for spins close to on resonance is relatively constant, but drops off rapidly

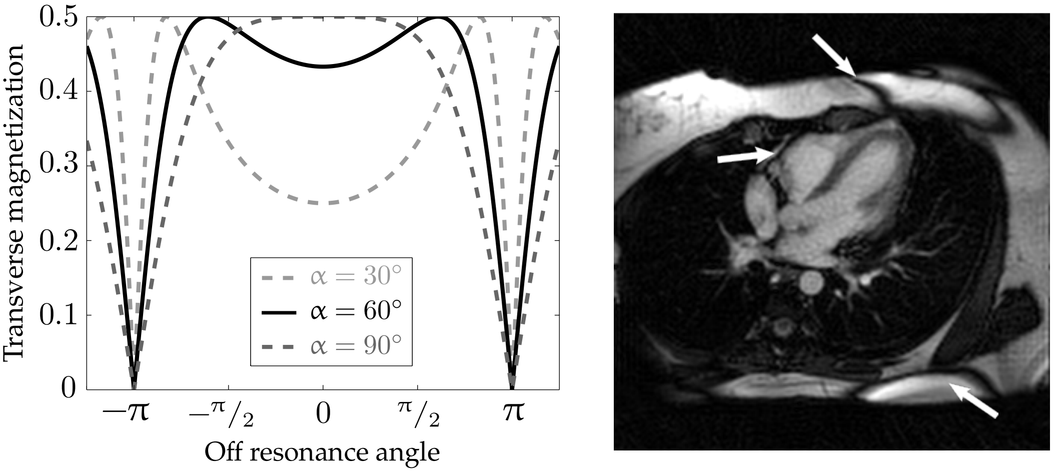

Figure 4: Left: Frequency response of the bSSFP sequence (for three different flip angles). The frequency response is periodic with a periodicity of 2π. Right: Banding artifacts in cardiac bSSFP imaging (bandings indicated by white arrows).

when the spin dephasing approaches $\pm\pi$. This phenomenon is responsible for the well known banding artifacts that often plague bSSFP imaging (an example of typical banding artifacts in cardiac imaging is shown in Fig. 4, right). Since the amount of spin dephasing is proportional to TR, a short TR is crucial in order to avoid severe banding artifacts in bSSFP images. Another possibility to reduce the impact of bandings, is to shift the frequency response by changing the phase cycle of bSSFP, which can help to shift banding artifacts away from areas of interest. For example, using a trivial α/α phase cycle will shift the banding artifacts towards on resonance. Banding artifacts can also be eliminated (with varying results) by combining multiple images that were acquired using different phase cycles [18, 19]. Obviously, this multiple-acquisition bSSFP requires a significant increase in scan time.

2.5 PROJECTION RECONSTRUCTION

Radial imaging or projection reconstruction is the oldest MRI sampling strategy, as it was already used in Lauterbur's original paper [20]. Outside of MRI, it is also the foundation of computed tomography (CT) and several other imaging modalities (PET, SPECT). However, with the introduction of Cartesian Fourier imaging [21, 22] and until recently, the radial trajectory has found very limited application in MRI. This can be mainly attributed to the more complicated reconstruction process (compared to the relatively simple discrete Fourier transform), i.e. computers as well as reconstruction algorithms needed time to mature. Also, the radial trajectory is very susceptible to errors due to gradient imperfections, necessitating very reliable and precise gradient hardware, that was not widely available in the past.

2.5.1 *The Radial Trajectory*

Non-Cartesian sampling of k-space is an alternative to the previously described Cartesian sampling. A variety of Non-Cartesian trajectories have been proposed for different purposes, that show different advantages and disadvantages. Arguably the simplest Non-Cartesian trajectory is the radial trajectory, which, as the name implies, consists of multiple radial spokes that vary in projection angle. Figure 5 shows a radial version of the previously described bSSFP sequence, as well as an example of radial k-space coverage, using a radial trajectory with 16 spokes and linear view-ordering (i.e. the projection angle increases linearly from zero to π).

One of the main advantages of the radial trajectory is that the center of k-space is sampled multiple times during the acquisition. This makes the acquisition relatively robust against motion and flow. In addition, using an interleaved or quasi-random view-order allows for a straightforward combination with view-sharing techniques, which can be used to considerably increase the frame rate in dynamic MRI [23, 24]. Another advantage is that undersampling of the trajectory results in relatively incoherent artifacts, i.e. artifacts that appear similar to noise or as streaks in the reconstructed image. Thus, in many cases, slight undersampling of the trajectory only leads to minor and tolerable artifacts, a fact that can be exploited in order to reduce total acquisition time. However, it is important to note that the number of projections that are required for full Nyquist k-space coverage, is slightly higher than for a standard Cartesian trajectory (by a factor of $\pi/2$ for a 2D radial trajectory). The uniform k-space coverage of the Cartesian trajectory is also somewhat more SNR efficient than radial. Another advantage of the radial trajectory is that the incoherent nature of radial undersampling artifacts is beneficial for sophisticated image reconstruction techniques like HYPR [25] and compressed sensing [26].

2.5.2 *Image reconstruction*

This section will give a brief introduction into the topic of Non-Cartesian image reconstruction. Gridding, in combination with the Fourier transform, is usually used for reconstruction of radial and other non-Cartesian data. Although, radial MRI data can be reconstructed similar to CT using filtered back-projection, direct Fourier reconstruction methods are currently more popular. A good overview of commonly and not-so-commonly used methods for the reconstruction of non-Cartesian data, as well as an extensive explanation of the recently proposed GROG method, is given in [27].

The common steps in a Fourier reconstruction of non-Cartesian data are:

1. Conversion of the acquired non-Cartesian data on a Cartesian grid (gridding procedure)

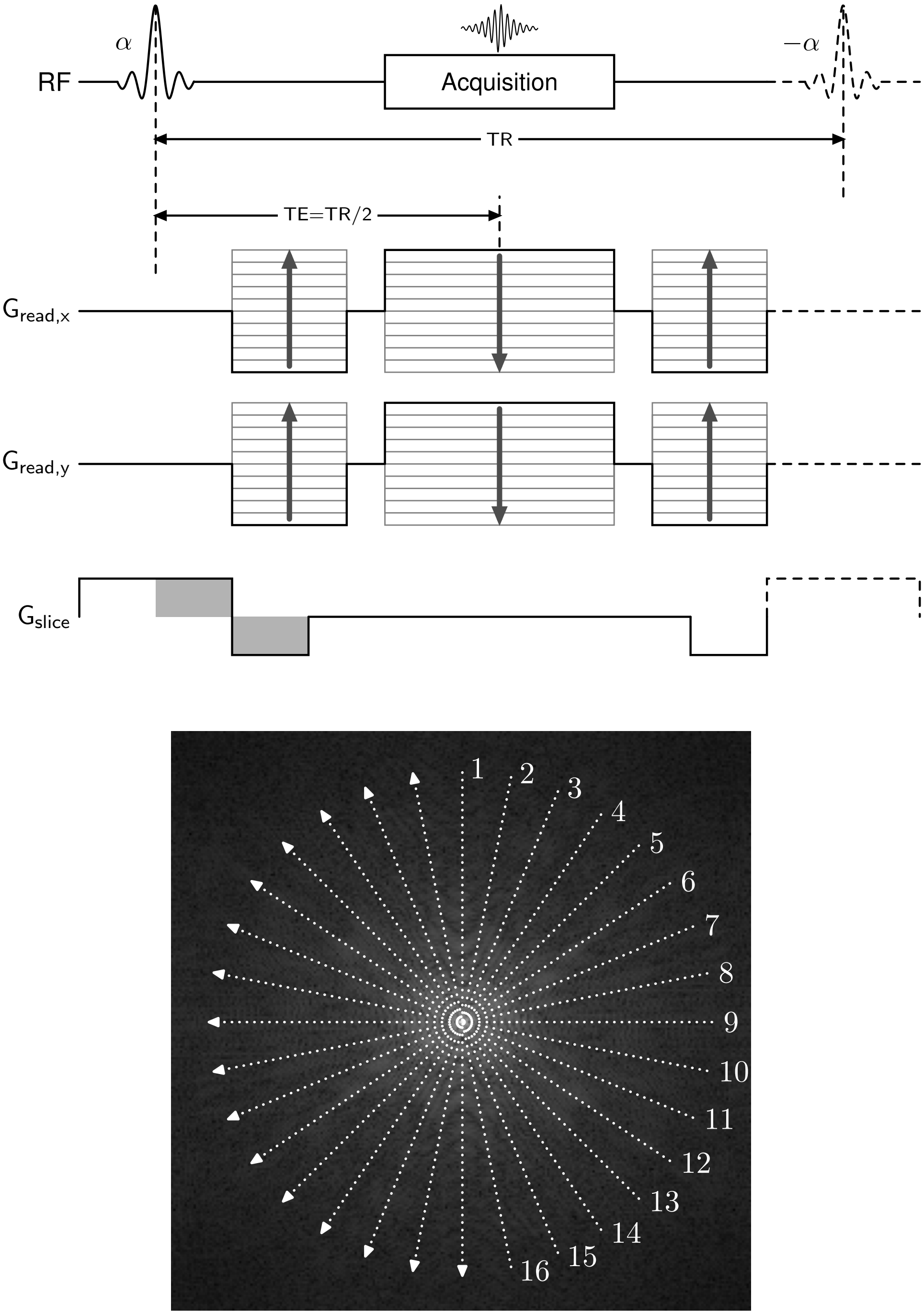
α
RF
Acquisition
−α
TR
TE=TR/2
$G_{read,x}$
$G_{read,y}$
G_{slice}
1
2
3
4
5
6
7
8
9
10
11
12
13
14
15
16

Figure 5: Top: 2D Radial version of the bSSFP sequence (compare to Fig. 3). Bottom: Illustration of radial k-space sampling with 16 equiangular spaced projections and linear view-ordering.

2. Standard uniform Fourier reconstruction

The only difference to reconstruction of Cartesian data is the gridding procedure prior to Fourier reconstruction, which will be elaborated on in the following.

Convolution Gridding

Convolution gridding is currently the gold-standard method in non-Cartesian MRI reconstruction. This method works by convolving each acquired Non-Cartesian point with an interpolation kernel and resampling the result at the locations of the Cartesian grid. While the optimal convolution kernel is a sinc function of infinite extent [28], the use of such a kernel leads to often prohibitively long computation times. Jackson et al. [29] tested a variety of possible convolution kernels and showed that the Kaiser-Bessel window produces the least amount of aliasing out of the tested group of functions. Since then, the standard convolution kernel has been a Kaiser-Bessel window with a width of 3 or 5.

In the next step, after convolving of the data on the Cartesian grid, a Fourier transform yields the image multiplied by the Fourier transform of the convolution kernel. In order to obtain the final image, this intermediate image has to be divided by the Fourier transform of the kernel (roll-off correction).

However, due to the non-uniform sampling density that is usually associated with Non-Cartesian trajectories, the reconstructed image will show blurring or other related image artifacts; the reconstructed image is convolved with the sampling density of the Non-Cartesian trajectory. In order to correct for this, the acquired data has to be properly weighted. This is usually accomplished by multiplying the data by an appropriate *density compensation function (DCF)* prior to gridding. For more exotic trajectories, analytical calculation of the DCF can sometimes be difficult to impossible. In these cases, the DCF is determined iteratively or numerically. The necessity for density compensation is equivalent to the need for proper averaging in Cartesian imaging when some k-space lines are acquired more often than others.

A drawback of convolution gridding is that the outcome depends on a number of parameters that must be determined beforehand (i.e. kernel function, kernel width, grid oversampling factor, DCF). Finally, convolution gridding requires that the region of support is at least one Δk, which makes it impossible to accurately grid Nyquist undersampled data. However, in practice and when the undersampling factor is not too high, convolution gridding works sufficiently well.

Non-Uniform Fourier Transform

Non-Uniform Fourier Transform is another option for the reconstruction of Non-Cartesian data. Since a conventional Non-Uniform Fourier Transform is computationally intensive and can require hours of computation time, a lot of research has been focused on the acceleration of this algorithm towards a *Non-Uniform Fast Fourier*

Transform (NUFFT). Sarty et al. [30] published a 2D implementation of a NUFFT algorithm, which they named *Generalized Fast Fourier Transform (GFFT)*. The authors noted that their algorithm is equivalent to conventional convolution kernel using a Gaussian kernel (instead of the more commonly used Kaiser-Bessel kernel). This equivalence explains the fact that NUFFT and Convolution gridding share similar strengths and weaknesses; both require additional gridding parameters as well as density compensation, and both methods do not allow accurate gridding of Nyquist undersampled data. NUFFT, specifically a Matlab toolbox that is freely available from Fessler et al. [31], was extensively used for the reconstruction of radial data in the first part of this work.

Part I

Fast MRI Relaxometry

3

IR TRUEFISP WITH A GOLDEN-RATIO BASED RADIAL READOUT

3.1 INTRODUCTION

Quantitative MRI involves pixel-wise mapping of proton density, longitudinal relaxation time T_1, or transverse relaxation time T_2 (or other relevant parameters) at each location in the tissue to be characterized. There has been significant recent interest in a quantitative approach to MRI, as it provides a means of evaluating pathology using absolute tissue characteristics rather than a contrast-based approach [32, 33, 34, 35, 36, 37, 38]. In addition, it has long been recognized that, if these parameters can be mapped in a time-efficient manner, theoretically images of any desired contrast could be retrospectively generated, and several groups have contributed to the literature on this long-standing goal in MRI [39, 40, 41, 42]. Standard clinical neurologic MRI examinations include T1- and T2-weighted images, fluid-attenuated inversion recovery (FLAIR) images, and occasionally spin-density contrast. Currently, a separate scan is required for each of these different contrasts, leading to long scan times. Besides possible consequent patient discomfort and higher costs due to longer scan times, there is also the potential of misregistration of clinically relevant anatomic information between different kinds of images due to inter-scan motion.

Many different quantification techniques have been proposed in previous literature. In most cases, T_1 and T_2 values are determined using two separate experiments (proton density is often provided by both). The most common methods for T_1 mapping are either based on the inversion-recovery spin-echo (IR-SE) or gradient-echo (IR-GRE) sequences [43, 44], or rely on multiple scans with variable flip-angle [45, 46] or repetition times (TR). For T_2 mapping, the gold-standard method is to exponentially fit the T_2 decay to the signal from multiple spin-echo experiments with variable echo times (TE). Often, in order to reduce scan time, a multi spin-echo sequence is used instead [47, 48]. Recently, another very fast method for T_1 and T_2 determination that uses the steady state signal level from multiple spoiled and balanced steady state free precession (SSFP) sequences for T_1 and T_2 quantification has been proposed [49]. However, it is not trivial to accelerate this method further using view-sharing techniques, since it does not rely on fine sampling of a transient signal along the temporal dimension, but on several image acquisitions in the steady-state.

Another promising approach for the simultaneous quantification of proton density, T_1 and T_2, that captures a smooth transition after signal preparation, is the inversion-recovery (IR) TrueFISP sequence [50]. This sequence consists of an inversion pulse followed by the acquisition of several balanced steady state free precession (bSSFP) images as the signal time course approaches the steady state. The parameters can then be obtained from a mono-exponential three parameter fit to the series of images. However, for accurate quantification it has been necessary to acquire this time series in a segmented fashion, due to the rapid signal evolution towards the steady state. The need for such a segmented approach considerably increases the required acquisition time. If one were to use this segmented approach for generating synthetic images corresponding to a standard clinical exam, this approach would still be slightly slower than the conventional exam. To facilitate clinical application of this approach, it is therefore desirable to generate the quantitative maps, and by extension all the images needed for a conventional exam, with an outlay of time that is equal to or less than that required presently for the conventional approach of separately acquired image sequences. Our goal was therefore to obtain proton density, T_1 and T_2 maps with a clinically acceptable spatial resolution and in an acceptable time frame. To this end, IR TrueFISP-based parameter mapping was combined with a radial trajectory with golden-ratio based profile order [24]. The advantage of this radial approach is that the center of k-space, and therefore the information about the image contrast, is frequently updated during scanning. Using a suitable view-sharing k-space filter, it is shown that it is possible to characterize the evolution of the signal towards the steady state with high-temporal resolution. As in a conventional IR TrueFISP, proton density, T_1 and T_2 can then be obtained from a fit to the image series.

The aim of this study is to develop an accurate and fast T_1 and T_2 relaxometry method that has the potential for clinical adoption. In this chapter, the generation of proton density, T_1, and T_2 maps from IR TrueFISP data acquired along a golden angle radial trajectory is described. These data can be acquired in approximately 6 seconds per imaging slice, meeting the requirements of short scan time discussed above.

A Full Paper on parts of this work together with results from Chapter 4 is currently under review in the journal *Magnetic Resonance in Medicine.*

In addition to the application of the proposed method to brain parameter mapping, first results of an application to cardiac relaxometry are presented. Another advantage of the golden-ratio based radial trajectory is that it is well suited for retrospective gating applications, e.g. in cardiac imaging: Due to the quasi-random nature of this trajectory, removal of some projections for cardiac or respiratory gating will still lead to a near uniform profile distribution. In this work, results from a retrospectively gated cardiac IR TrueFISP experiment are presented as a proof of principle for the application of this concept to cardiac relaxometry. Furthermore, it is shown that the signal from the center of k-space (the DC signal) that is acquired in every projection can be used for cardiac self-gating of the IR TrueFISP experiment.

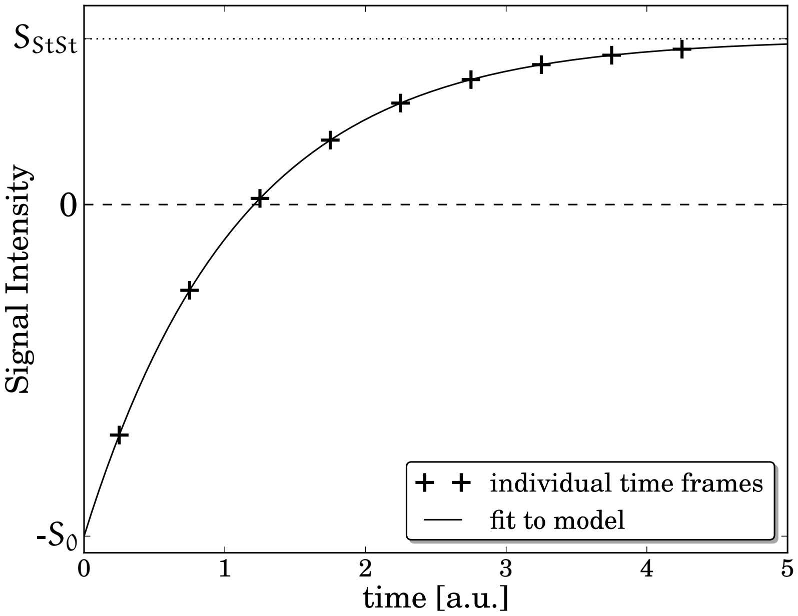

Figure 6: Signal time course of an IR TrueFISP experiment. Following signal inversion, the signal approaches the bSSFP steady state exponentially during a continuous run of bSSFP acquisitions.

3.2 THEORY

3.2.1 *IR TrueFISP-based Parameter Estimation*

The IR TrueFISP experiment consists of an inversion pulse followed by the acquisition of multiple bSSFP images as the signal time course approaches the steady state. For on-resonant spins, the IR TrueFISP signal after n repetition times TR can be described by a 3-parameter exponential, according to [50]:

$$S(n\,TR) = S_{StSt} - (S_0 + S_{StSt}) \cdot \exp((-n\,\mathrm{TR})/T_1^*) \tag{3.1}$$

Where S_{StSt} is the steady state signal; S_0 is the transient state signal extrapolated to $t = 0$; and T_1^* is the apparent relaxation time. The IR TrueFISP signal time course is illustrated in Figure 6.

The signal at the beginning of the IR TrueFISP experiment can be described in good approximation by

$$S_0 = M_0 \sin \alpha/2 \tag{3.2}$$

Using this equation, M_0 can be obtained directly from the fitting parameter S_0. In order to obtain T_1 and T_2 it is necessary to identify their relationships with the other two fitting parameters S_{StSt} and T_1^*. For TR $\ll T_{1,2}$, the bSSFP signal equation for the steady-state (Eq. 2.24) can be written as

$$S_{StSt} = \frac{M_0 \sin\alpha/2}{\left(\frac{T_1}{T_2}+1\right) - \cos\alpha\left(\frac{T_1}{T_2}-1\right)} \tag{3.3}$$

In a standard bSSFP acquisition at zero off-resonance and prepared with an initial $\alpha/2$ pulse, the approach of the bSSFP signal towards the steady state takes the form of an exponential decay with the time constant T_1^*. This exponential decay is a weighted average of T_1 and T_2 relaxation, with the flip angle α determining the weighting [51]:

$$E_1^* = E_1 \cos^2\alpha/2 + E_2 \sin^2\alpha/2 \tag{3.4}$$

Where $E_1^* = \exp(-\mathrm{TR}/T_1^*)$ and $E_{1,2} = \exp(-\mathrm{TR}/T_{1,2})$. Schmitt et al. [50] showed that this equation can be simplified for TR $\ll T_{1,2}$ to

$$T_1^* = \left(\frac{1}{T_1}\cos^2\alpha/2 + \frac{1}{T_2}\sin^2\alpha/2\right)^{-1} \tag{3.5}$$

Using equations 3.2, 3.3 and 3.5, it is now possible to derive expressions for the calculation of T_1, T_2 and M_0 from the three fit-parameters S_{StSt}, S_0 and T_1^*, and the excitation flip angle α, according to [50, 52]:

$$\begin{aligned} T_1 &= T_1^* \frac{S_0}{S_{StSt}} \cos\alpha/2 && (3.6) \\ T_2 &= T_1^* \sin^2\alpha/2 \left(1 - \frac{S_{StSt}}{S_0}\cos\alpha/2\right)^{-1} && (3.7) \\ M_0 &= \frac{S_0}{\sin\alpha/2} && (3.8) \end{aligned}$$

3.3 METHODS

3.3.1 *Development of a Radial bSSFP Sequence*

All sequence development was performed using the standard pulse sequence development environment for Siemens MRI systems (i.e. Integrated Development Environment for Applications (IDEA), Siemens Medical Solutions, Erlangen, Germany). A standard Cartesian FLASH sequence template was converted into a bSSFP se-

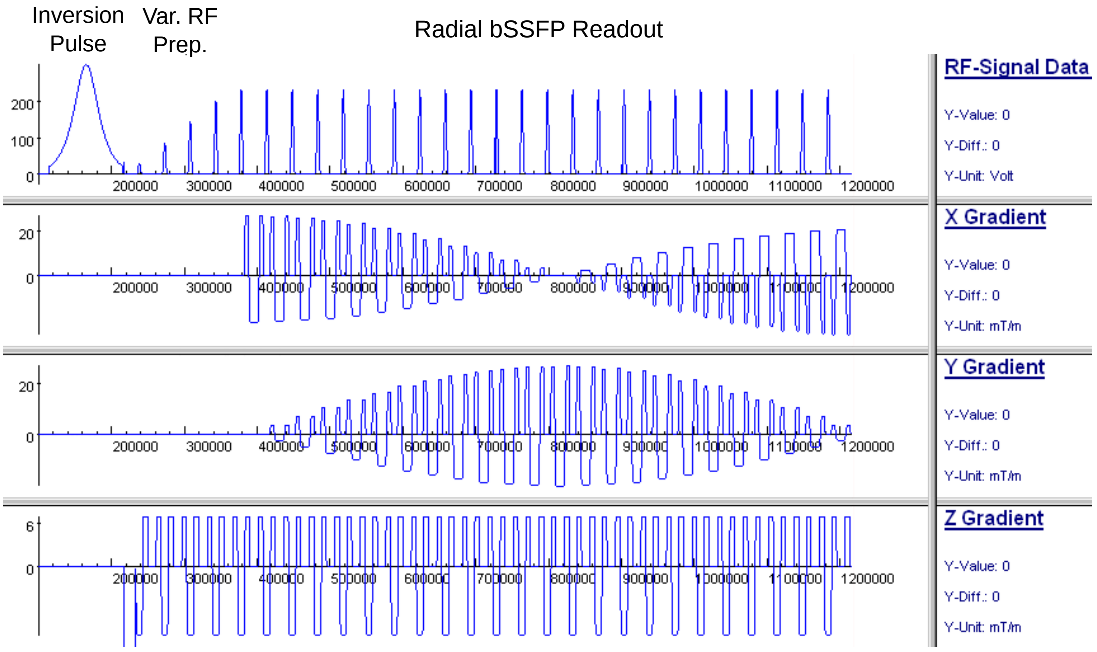

Figure 7: Simulation of the radial bSSFP sequence implemented in IDEA. In this example, signal inversion and a linear increasing flip angle preparation module are followed by a radial bSSFP acquisition with conventional linear ordering of projection angles.

quence by fully balancing the gradient moments on all axes. In a first step towards implementing a radial trajectory, the phase-encoding gradient was removed from this sequence. Acquisition of different projection angles was then achieved by accordingly modifying the rotation matrix that defines the current slice orientation. Multiple radial trajectories were implemented in the sequence, including a golden-ratio profile order, as well as simple linear ordering of projection angles. For non-selective signal inversion, a standard adiabatic inversion pulse followed by a spoiler gradient was included at the beginning of the sequence. This was followed by a linearly increasing flip angle preparation [53] with a configurable number of pulses in order to suppress off-resonance oscillations. A simulation of the finished radial IR TrueFISP sequence (from the IDEA development environment) is shown in Fig. 7.

3.3.2 *Centering the Radial Trajectory*

The magnetic field gradients of an MRI system are created by three separate gradient coils, one for each direction in the Cartesian coordinate system. In order to allow for fast image acquisition, strong gradient fields have to be ramped up and down very quickly, with typical amplitudes and slew rates of about 30 mT/m and 150 mT/(m ms), respectively. Due to electromagnetic induction and other effects, correct timing of gradient switching is very difficult. Although vendors account for these effects, there is usually a remaining delay between the time the gradient is intended to be switched on and the time this actually happens. These *gradient delays* are relatively

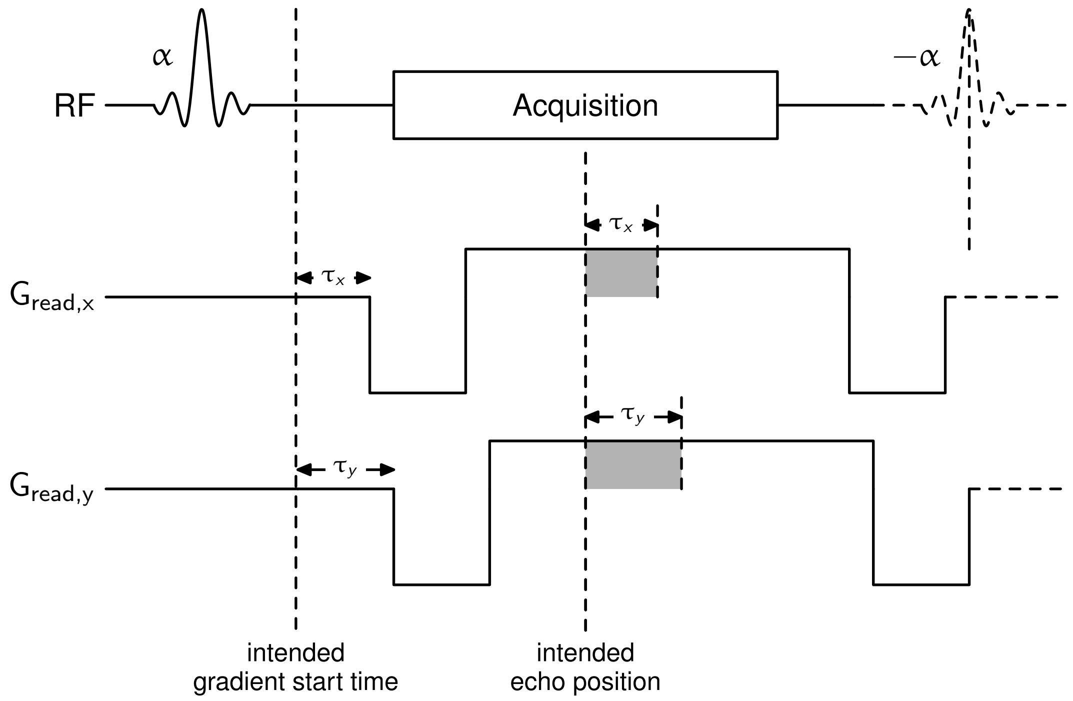
α
RF
Acquisition
$-\alpha$
τ_x
$G_{\mathrm{read,x}}$
τ_x
τ_y
$G_{\mathrm{read,y}}$
τ_y
intended gradient start time
intended echo position

Figure 8: Effect of gradient delays (denoted by τ_x, τ_y) on the timing of a radial bSSFP sequence (for better visualization, gradient delays are highly exaggerated compared to the duration of the acquisition window). The shaded areas correspond to the extra gradient moments in x- and y-direction that have accumulated at the intended echo position, which is equivalent to a shift in k-space. Resulting trajectory errors are illustrated in Figure 9.

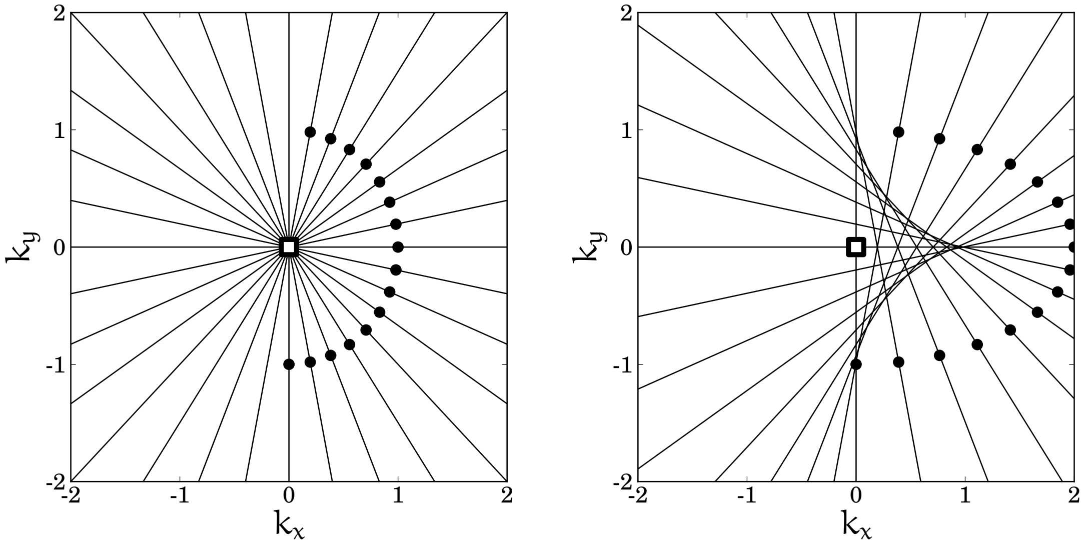

Figure 9: Effect of gradient delays on a 2D radial trajectory with 16 projections (only the center part of k-space is shown). Left: Equal gradient delays in x and y direction lead to a shift between the time of the gradient-echo for each projection (indicated by circles) and the intended echo time in the center of k-space (indicated by a square). Right: Anisotropic gradient delays additionally shift the projections with respect to each other. As a result, the projections do not share a common intersection point anymore. This is the more realistic situation.

unproblematic for most Cartesian imaging methods as they only lead to a slight shift in the echo position. However, for radial and other non-Cartesian trajectories, gradient delays lead to trajectory errors that cause image artifacts if left uncorrected. Figure 8 shows the effect of gradient delays on the timing of a radial bSSFP sequence. Radial trajectory errors due to isotropic (i.e. same delay for all axes) and anisotropic gradient delays are illustrated in Figure 9.

According to the Fourier shift theorem, a shift in the echo position during readout leads to a linear phase in image space:

$$\mathcal{F}\left(S(k-\Delta k)\right) = \mathcal{F}\left(S(k)\right) \cdot \exp\left(\frac{-2\pi i \Delta k \cdot r}{N}\right) \tag{3.9}$$

where $\mathcal{F}$ stands for the discrete Fourier transform, N is equal to the number of acquired data points, r is the position in image space, and k and Δk denote k-space position and shift, respectively. Thus, observing the image space phase presents a convenient way to measure timing errors (e.g. caused by gradient delays) between intended and actual echo position. However, shim inhomogeneities, chemical shift, susceptibility effects and other local Larmor frequency shifts lead to additional static phases that are superimposed on this linear phase. These static phases can be removed by acquiring projections in opposing pairs (e.g. +x- and −x-direction) and subtracting the image phase for each pair of projections. The timing error / gradient delay can

System and Location	τ_x [μs]	τ_y [μs]	τ_z [μs]	dwell time of acq. [μs]
Siemens Avanto 1.5 T, Würzburg	2.98	3.84	3.25	9.8
Siemens Espree 1.5 T, Cleveland	3.42	4.49	2.70	9.8
Siemens Skyra 3 T, Würzburg	-0.45	-0.39	-1.02	7

Table 1: Examples of measured gradient delays for three MRI systems at two locations. Note that these delays are only valid for a specific dwell time and for imaging sequences with similar timing.

then be obtained from a linear fit to the remaining image phase. Specifically, the timing error (from now on referred to as delay τ) is proportional to the fitted slope (m_{phase} in units of radians per pixel):

$$\tau = \frac{m_{\text{phase}}}{2\pi} \cdot N \cdot t_{\text{dwell}} \tag{3.10}$$

Where t_{dwell} denotes the dwell time (i.e. the sampling interval of the analog-to-digital converter). Delays for all three gradient coils can be obtained by acquiring opposing projections in the three directions of the scanner's coordinate system.

Table 1 gives an overview of measured gradient delays for three different MRI systems. Note that gradient delays are not guaranteed to be completely stable over time. Furthermore, measurement of gradient delays also depends on sequence timing and may be slightly different depending on the sequence and sequence parameters used. The values cited here should therefore be taken with a grain of salt and gradient delay measurements should be repeated for each individual sequence (and ideally before every single scan, e.g. as part of a pre-scan).

Peters et al. [54] proposed a simple method to correct radial trajectories for gradient delays. After determination of the gradient delays on all three axes, the radial trajectory can be corrected for these delays by adjusting the gradient moment (i.e. the time integral of a gradient pulse) of the read dephasing gradient for each projection according to the current projection angle. To correct for anisotropic gradient delays, an additional correction gradient is required that is oriented orthogonal to the current projection angle. For further explanation/discussion refer to [54] and [55]. This gradient delay correction method was implemented into the radial IR TrueFISP sequence and used throughout all radial imaging experiments presented in this work.

3.3.3 *Golden-ratio based profile order*

In conventional radial MRI, k-space is sampled with equidistantly spaced radial lines in the order of increasing azimuthal angles from zero to π (or 2π). For dynamic applications this profile order is often interleaved so that view-sharing can be employed [23]. Recently, a quasi-random radial profile order was proposed, with a constant azimuthal angle spacing of approx. 111.246°, or π divided by the golden ratio [24]. This profile order has the advantage of a near-optimal uniform k-space sampling for any number of projections, whereas an interleaved acquisition is only optimal for a predetermined number (specifically the total number of projections divided by the number of interleaves). This flexibility makes it possible to choose the frame rate of a dynamic acquisition retrospectively and/or dependent on the position in k-space. Due to the close relationship between the golden ratio and the Fibonacci series, k-space sampling becomes most uniform whenever the number of projections approaches a Fibonacci number.

3.3.4 *Image reconstruction using a modified k-space weighted image contrast (KWIC) filter*

Using view-sharing, the golden-ratio based profile order makes it possible to generate a large number of images with different contrasts from a single-shot inversion-recovery experiment. To reconstruct a single time-frame, the center of k-space is taken from only a few acquired projections close to the chosen reconstruction time point, whereas the high spatial frequencies are provided by including data from time points further away, as illustrated in Figure 10. Such a k-space filter, as initially proposed by Song et al. [56] by the name of k-space weighted image contrast (KWIC), ideally leads to a uniformly sampled k-space for every time-frame, thereby avoiding undersampling artifacts.

As illustrated in Figure 11, the reconstruction window starts with a given number of projections for the center of k-space (e.g. 8), and increases to the next Fibonacci number when the Nyquist sampling criterion would be violated otherwise. The next time frame is then reconstructed by moving this k-space filter by a chosen number of projections. In this work, the filter was moved in time by the temporal width of the reconstruction window in the center of k-space, so that all acquired data were used at least once in the reconstruction of the time series.

For density compensation, a standard Ram-Lak DCF was used. As illustrated in Figure 11, it was necessary to correct this DCF for angular anisotropy due to the golden-ratio based profile order. To this end, the angular distance to the two next neighboring projections was determined for each projection in each ring of the radial k-space filter and the Ram-Lak DCF was weighted by this distance. After applying this DCF, the image time series was reconstructed using the nonuniform fast Fourier transform (NUFFT) from the image reconstruction toolbox by Fessler et al. [31].

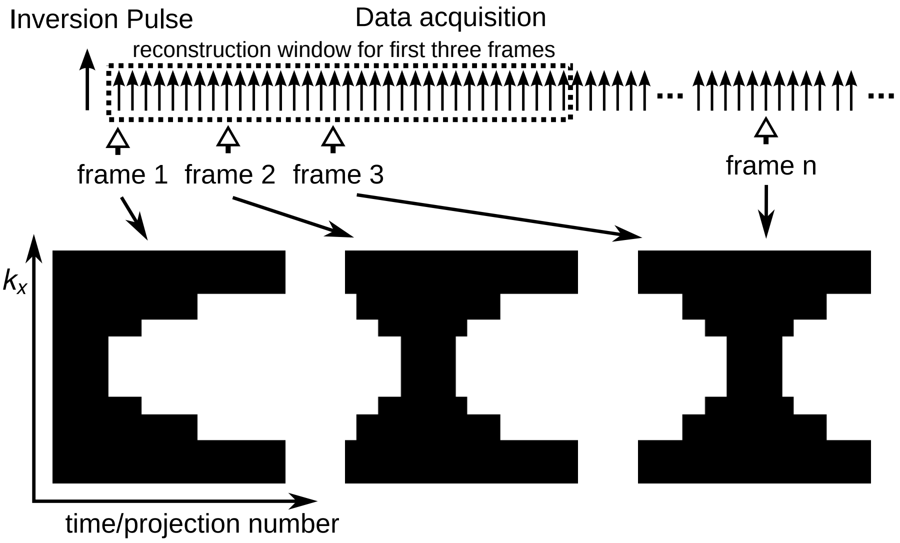
Inversion Pulse
Data acquisition
reconstruction window for first three frames
...
frame 1
frame 2
frame 3
frame n
k_x
time/projection number

Figure 10: Illustration of data selection by temporal k-space filtering. Top: Following inversion, signal evolution towards the bSSFP steady state is observed using a radial readout with golden-ratio based profile order. In a first step towards reconstruction of a single time-frame, a number of projections is selected that sufficiently covers the entire k-space. Bottom: From these projections and depending on the k-space position in read direction (k_x), the filter selects only as many projections close to the chosen reconstruction time point as necessary according to Nyquist (selected projections are indicated in black). Thus, only a few projections need to be selected close to the center of k-space while more and more projections need to be included further out in k-space. This leads to the characteristic hourglass/tornado shape of the filter. Initially, following the inversion pulse, this filter is highly asymmetric, since there is no data from prior time points. Later, the filter becomes more and more symmetric.

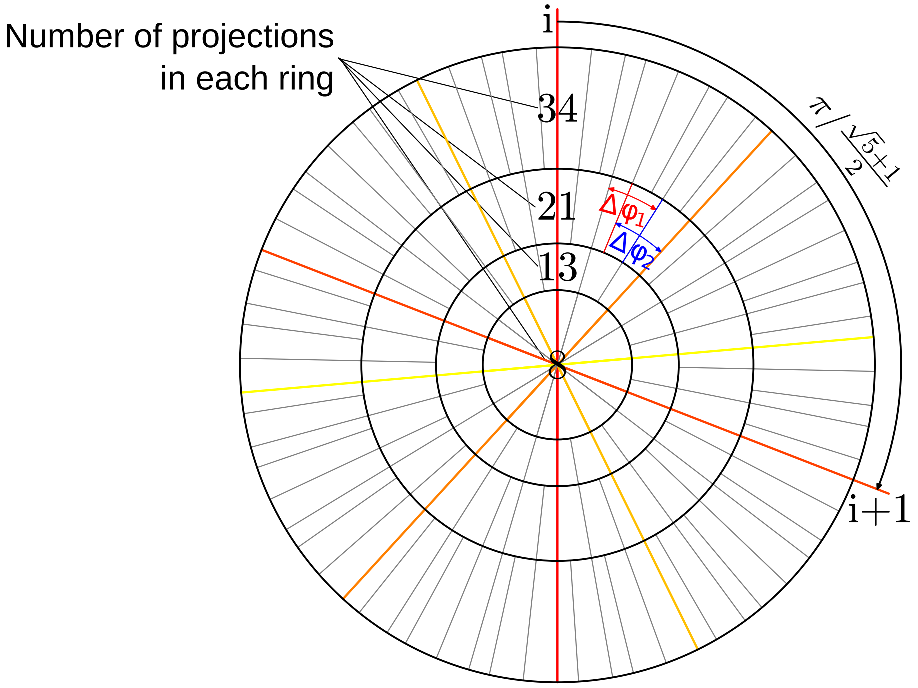

Figure 11: Illustration of golden-ratio based radial profile order and filtering in k-space. Subsequent projections are spaced by an angle increment of π divided by the golden mean (five successive projections are color-coded from red to yellow). For k-space filtering, projections are grouped into rings. The central ring consists of eight projections that were acquired closest to the target time point. In order to fulfill the Nyquist criterion, the included number of projections jumps to the next Fibonacci number further out in k-space, thus forming the next ring. This results in a relatively uniform k-space sampling density. This figure also illustrates that in each ring, the angular distance between the next neighbors of a projection alternates between two possible values (denoted by $\Delta\phi_1$ and $\Delta\phi_2$ in red and blue, respectively). Thus, a density compensation function based on the Ram-Lak filter has to be corrected for this angular anisotropy.

3.3.5 *Imaging experiments*

Brain Imaging

In vivo brain experiments were performed with a healthy volunteer on a 1.5 T whole-body imaging system (Magnetom Espree, Siemens Healthcare, Erlangen, Germany). For signal reception, a 32-element phased-array head receiver coil (Siemens Healthcare) was used. Informed consent was obtained and the project was approved by the local Institutional Review Board (IRB). After non-selective adiabatic inversion, a linearly increasing flip angle preparation consisting of 4 pulses was used to suppress off-resonance oscillations. After this preparation signal evolution towards the steady state was observed using the described radial bSSFP sequence with golden-ratio based profile order and 1300 projections. Other acquisition parameters used are as follows: TR = 4.78 ms, flip angle (FA) = 45°, matrix size: 256x256, field of view (FoV) = 220x220 mm^2, slice thickness = 6 mm, receiver bandwidth = 650 Hz/pixel, acquisition time (TA) = 6 s.

As references for artificial contrast generation, a T_1-weighted spin-echo (TR = 500 ms, TE = 9.5 ms, TA = 2 min 10 s), a T_2-weighted turbo spin-echo (TR = 4 s, TE = 96 ms, echo train length (ETL) = 11, TA = 1 min 40 s) and a fluid attenuated inversion recovery (FLAIR) [57] turbo spin-echo sequence (TR = 9 s, TE = 112 ms, inversion time (TI) = 2.5 ms, ETL = 21, TA = 2 min 6 s) were run with the same resolution and slice position as the IR TrueFISP scan.

Cardiac Imaging

In vivo cardiac experiments were performed with a healthy volunteer on a 1.5 T whole-body imaging system (Magnetom Espree, Siemens Healthcare, Erlangen, Germany). Informed consent was obtained and the project was approved by the local Institutional Review Board (IRB). For signal reception, a six-element body matrix array was used in combination with a six-element spine array (Siemens Healthcare). The coils were used in circularly polarized (CP) matrix mode, i.e. every three elements of the body array and every two elements of the spine array were combined using a smart combiner network [58] and only the primary mode signals were acquired and stored to disk, resulting in a total of five coil channels (two and three channels for the body array and spine array, respectively). The volunteer was instructed to hold his breath during a radial IR TrueFISP experiment with golden-ratio based profile order in short axis orientation of the heart. The electrocardiography (ECG) signal was recorded simultaneously and used to trigger the start of the experiment to the beginning of the diastole. After application of an adiabatic inversion pulse, the radial bSSFP experiment ran uninterrupted for 7.5 s (corresponding to 2560 acquired projections). Individual time frames were reconstructed from this data using retrospective gating, as explained in the next section. Other sequence parameters were as follows: TR =

2.9 ms, FA = 45°, matrix size: 144x144, FoV = 300x300 mm^2, slice thickness = 6 mm, receiver bandwidth = 1000 Hz/pixel.

3.3.6 *Signal Processing and Parameter Fitting*

Brain Imaging

In a first reconstruction step, adjacent projections were selected for each individual time frame and filtered using the KWIC filter described above. Each frame contained 8 projections in the center of k-space and reconstruction windows for consecutive frames were separated by these 8 projections. Moving further out in k-space, the number of projections jumps to the next Fibonacci number (i.e. 13, 21, 34, 55, etc., up to a maximum of 233 projections), whenever the Nyquist criterion would be violated otherwise. Images were reconstructed from these filtered projections using NUFFT gridding [31] and an analytically calculated density compensation function as described in the theory section. Multi-channel images were combined using the adaptive combine method of Walsh et al. [59]. The resultant time series of images was used to determine values for the parameters M_0, T_1 and T_2 by fitting the data pixel-wise to equation 3.1.

Cardiac Imaging

Radial trajectories are well suited for cardiac and/or respiratory self-gating since each projection travels through the center of k-space. The center of k-space (the *DC signal*) reflects the total signal of the excited volume convolved with the sensitivities of the receiver coil array. It was shown in previous work that DC signal fluctuations can be used for cardiac and/or respiratory self-gating [60, 61].

To assess DC signal fluctuations resulting from cardiac motion, all coil channels were analyzed separately. The coil channel providing highest sensitivity towards cardiac motion (one channel of the body matrix) was selected manually and used for retrospective cardiac self-gating. This signal was low-pass filtered in order to remove high-frequency signal components caused by noise and trajectory errors. Furthermore, in order to remove the general dynamics of the IR TrueFISP experiment (the relaxation curve) from the DC signal, a biexponential version of Equation 3.1 was fit to this time series and the fitted time curve was subsequently subtracted from the DC signal. The gating window was then manually determined from this self-gating signal.

Retrospective gating of the cardiac IR TrueFISP experiment was achieved by excluding projections from the reconstruction that were not acquired during the diastolic phase of the cardiac cycle, i.e. outside of the gating window. For each individual time frame, the remaining projections were then sorted by their temporal distance from the target time point. An asymmetric KWIC filter, similar to the filter shown on the

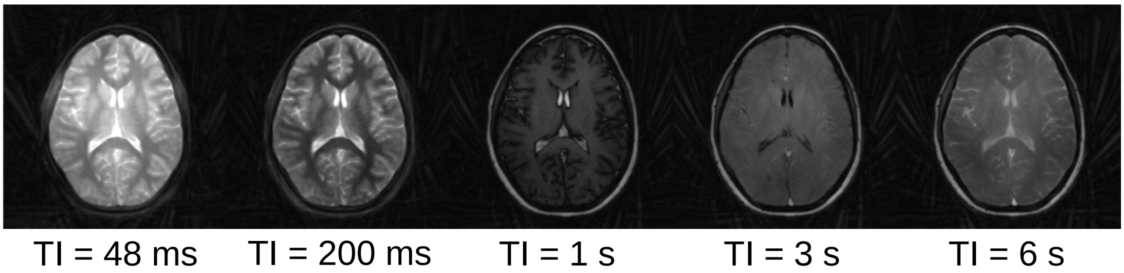

Figure 12: Five representative time frames from the IR TrueFISP experiment with inversion times (TI) ranging from 48 ms to 6 s.

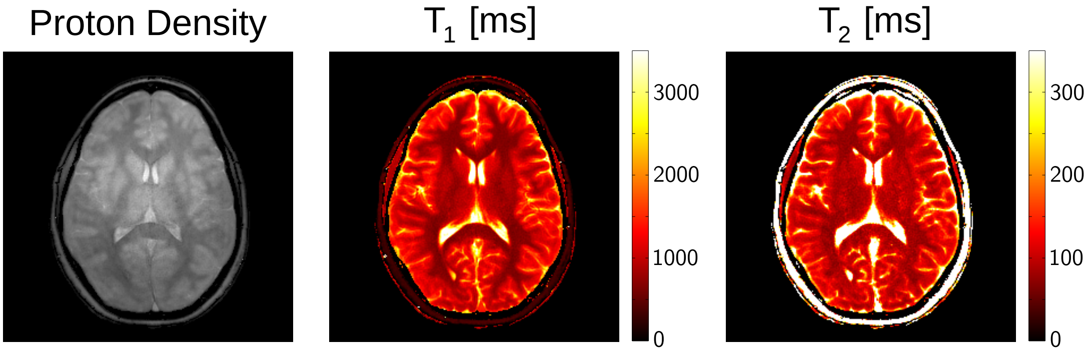

Figure 13: Proton density, T_1 and T_2 maps, determined from a fit to the reconstructed time series.

far left of Figure 10, was used to select a full Nyquist-sampled data set that consisted of projections that were acquired closest to the target time point. The form of this KWIC filter and the rest of signal processing and parameter fitting was the same as for the brain imaging experiments, described above.

3.4 RESULTS

Figure 12 shows five representative time frames from the radial IR TrueFISP experiment with inversion times ranging from 48 ms to 6 s. The first image of the time series is mostly proton density-weighted, whereas following time frames display the signal evolution towards the steady state and show a combination of T_1- and T_2-weighting. Resulting parameter maps are shown in Fig. 13.

Typical clinically used image contrasts were artificially generated from these parameter maps. Figure 14 shows synthetic T_1-weighted, T_2-weighted and FLAIR images next to their respective references, obtained from a conventional scan. Although general contrast information is very similar between the two sets of images, there are some differences evident. First, ventricles and venous sinuses appear brighter in the synthetic images compared to the reference. Furthermore, white/gray matter contrast is a little off, especially apparent in the FLAIR and T_2-weighted images.

The determination of the gating window from the DC signal for the reconstruction of the cardiac IR TrueFISP data is illustrated in Figure 15. The unfiltered and low-pass

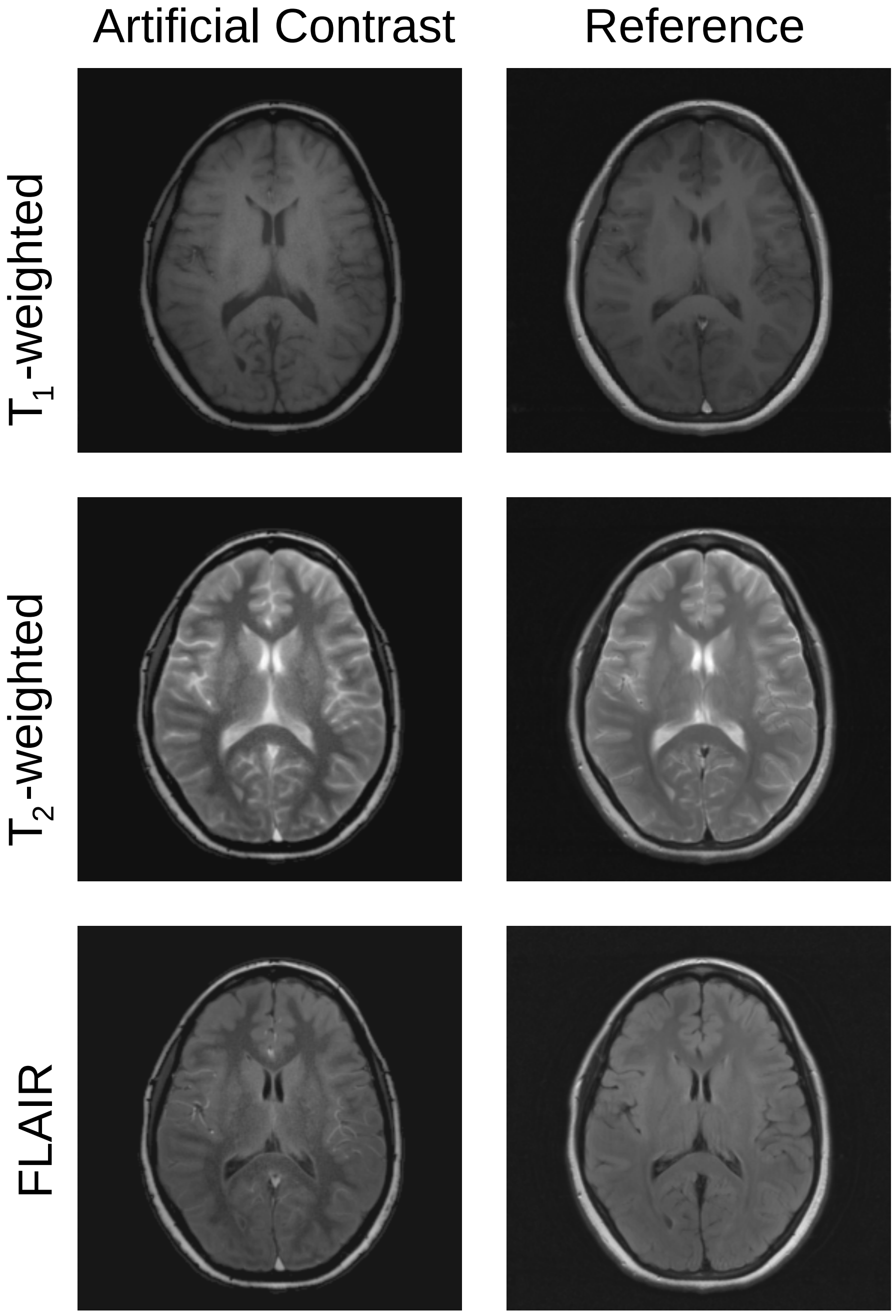
Artificial Contrast
Reference
T1-weighted
T2-weighted
FLAIR

Figure 14: Artificially generated images compared to standard clinical MRI reference images. Although general contrast information is closely reproduced, there are some differences evident: Ventricles and venous sinuses appear brighter than in the standard images and gray/white matter contrast is a little different, especially apparent in the FLAIR and T_2-weighted images.

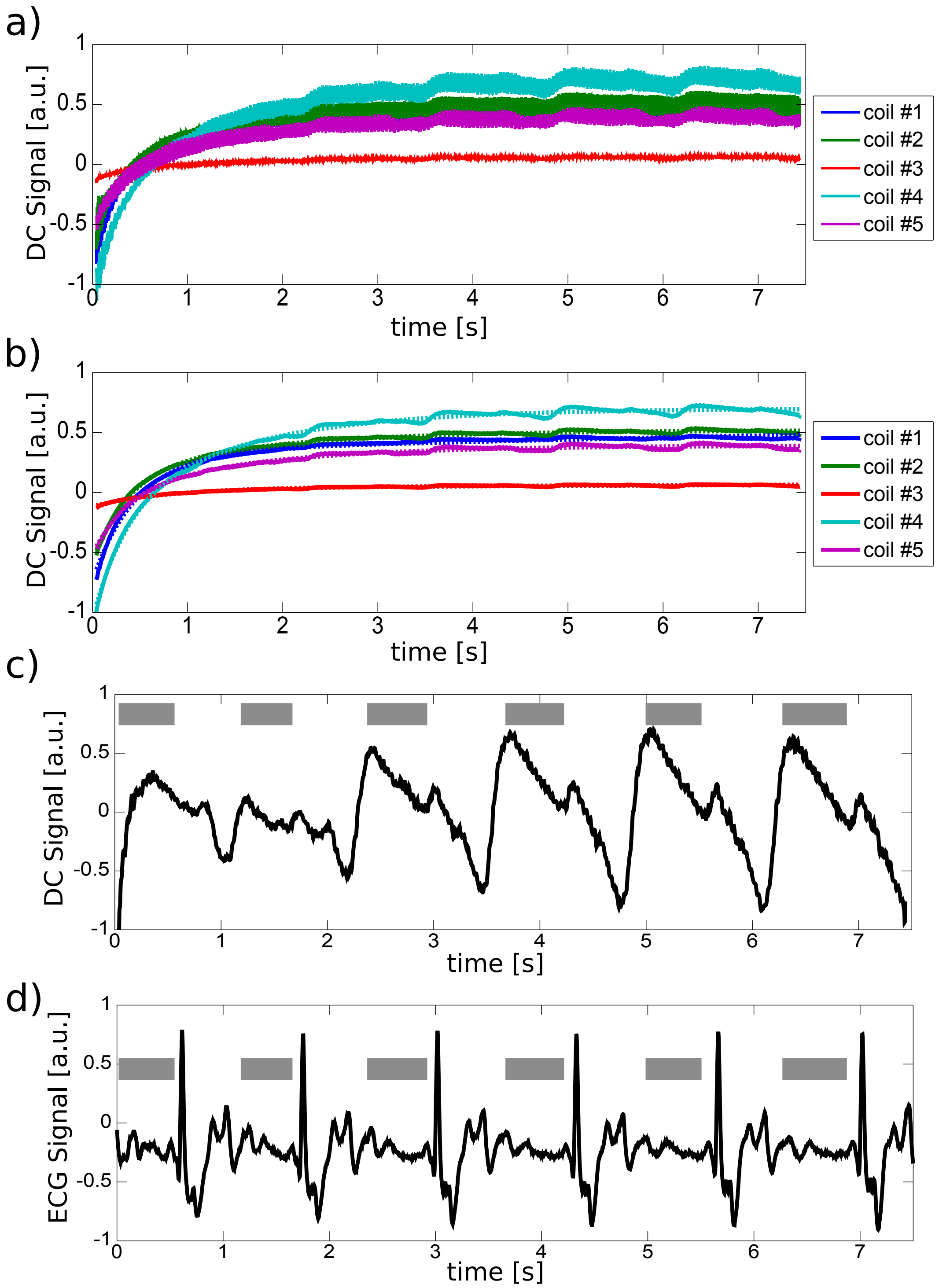

Figure 15: a) Unfiltered DC signal for all five coil channels. High-frequency signal components due to noise and trajectory errors are removed from this signal using low-pass filtering. The resulting filtered DC signal is shown in b). A biexponential version of Equation 3.1 is then fit to this time series, as shown by dotted lines in b). This fitted time course was then subtracted from the DC signal in order to remove the relaxation dynamics of the IR TrueFISP experiment. The remaining DC signal nicely shows signal fluctuations due to cardiac motion, as demonstrated in c) for one of the coil channels (#4). This cardiac self-gating DC signal shows a high correlation with the recorded ECG signal (d). The gating window was manually determined from this self-gating signal, as indicated by gray-shaded boxes in c) and d). Only projections that were acquired in the corresponding time intervals were included in the reconstruction of the time series (shown in Figure 16).

filtered DC signal for all five coil channels is shown in Figure 15a and 15b, respectively. A biexponential version of Equation 3.1 is fit to the filtered DC signal, as shown by dotted lines in Figure 15b. This fitted time course was then subtracted from the DC signal in order to remove the relaxation dynamics of the IR TrueFISP experiment. The remaining DC signal shows high correlation with the recorded ECG signal (Figure 15d), as demonstrated in Figure 15c for the coil channel that was most susceptible to cardiac motion (coil #4).

Figure 16 shows representative time frames from the radial IR TrueFISP experiment that was acquired in short axis orientation of the heart. Resulting parameter maps are shown in Fig. 17.

3.5 DISCUSSION

While parameter mapping with an IR TrueFISP based scheme has been previously demonstrated [50, 52], the introduction of a golden-ratio based radial readout with a temporal k-space filter greatly accelerates this technique, bringing the time required for parameter estimation down to 6 s/slice. This represents a 20-fold improvement over the previously reported, 2 min/slice obtained with a segmented Cartesian acquisition [50, 52]. This critical improvement in the speed of the parameter mapping experiment allows whole head coverage (20-30 slices) in 2-3 minutes, making quantitative and synthetic imaging clinically viable.

Figure 14 demonstrates that the contrast information for a standard neurologic clinical MRI examination (T_1-weighted, T_2-weighted, spin-density-weighted, and FLAIR images) is closely reproduced in the synthetic images generated from the single-shot IR TrueFISP dataset. Image contrast is very similar between the two sets of images. However, there are some differences evident. First, the inherent flow sensitivity of the single-slice TrueFISP sequence causes the ventricles and the venous sinuses to appear brighter than in the standard images. This can be explained by higher flow sensitivity of the single-slice IR TrueFISP scan compared to the references. Furthermore, parts of the cerebrospinal fluid (CSF) in the calculated FLAIR image are more prominent than in the reference image. This appears to be the result of different responses of the two acquisition methods on partial volume effects, as previously shown by Gulani et al. [52]. Finally, the T_1 and especially the T_2 contrast of the two image sets are not completely identical. This is most evident in the T_2-weighted and the FLAIR image (that is also highly T_2-weighted); gray/white matter contrast in the synthetic FLAIR is much higher than in the reference. This hints to systematic T_1 and T_2 quantification errors that are further investigated in Chapter 4.

Although only three artificially generated contrasts are shown in this work, synthetic imaging allows the generation of any desired contrast and any number of images. Physicians may retrospectively adjust T_1- and T_2-weighting to their liking, as illustrated as a graphical user interface example in Figure 18. This is similar to

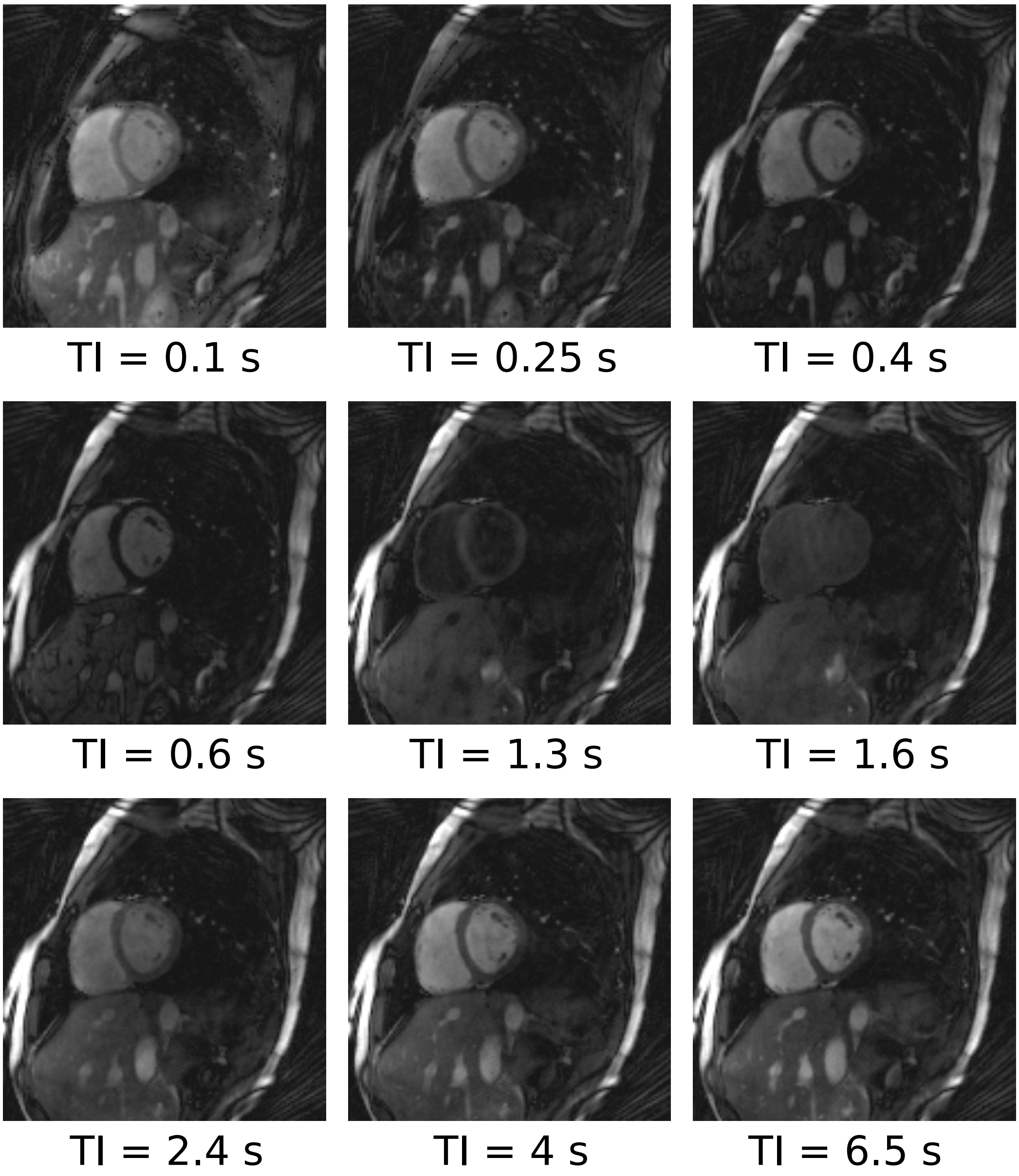
TI = 0.1 s
TI = 0.25 s
TI = 0.4 s
TI = 0.6 s
TI = 1.3 s
TI = 1.6 s
TI = 2.4 s
TI = 4 s
TI = 6.5 s

Figure 16: Representative time frames from the cardiac IR TrueFISP experiment.

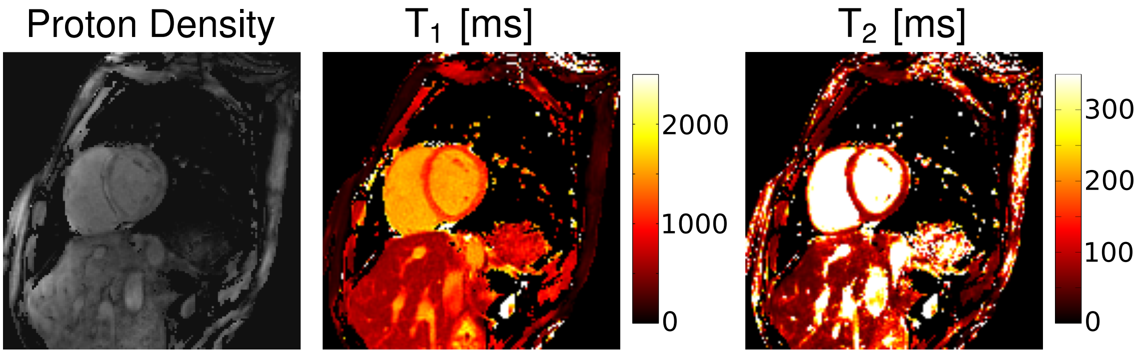
Proton Density
T1 [ms]
2000
1000
0
T2 [ms]
300
200
100
0

Figure 17: Proton density, T_1 and T_2 maps, as obtained from a fit to the reconstructed time series of the cardiac IR TrueFISP experiment.

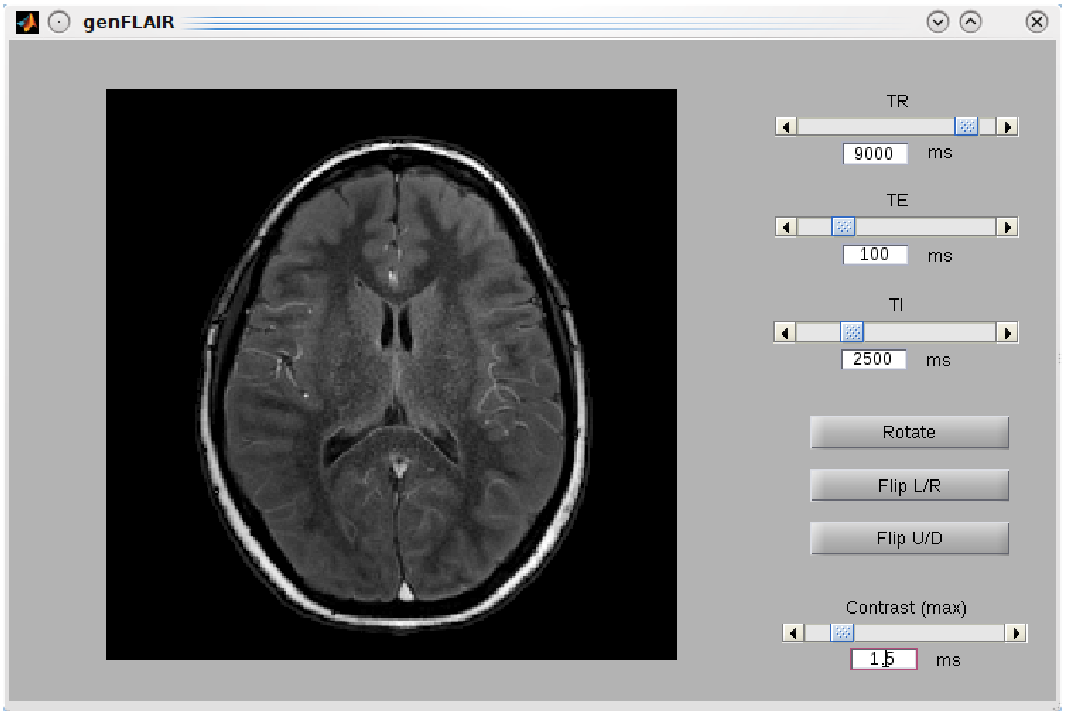

TR 9000 ms

TE 100 ms

TI 2500 ms

Contrast (max) 1.5 ms

Figure 18: Illustration of synthetic imaging in MRI. Based on a full set of relaxometry data (proton density, T_1 and T_2), the user can retrospectively adjust image contrast by selecting repetition time (TR), echo time (TE) and inversion time (TI) that are then used for synthetic image generation.

the current situation in computed tomography (CT), in which the physician can adjust windowing of the quantitative Hounsfield unit. Further discussion of synthetic imaging is provided in [52].

The results from the cardiac experiment show that the proposed radial IR TrueFISP method is well suited for cardiac relaxometry. It was possible to obtain proton density, T_1 and T_2 from a single-shot IR TrueFISP experiment by excluding projections that were not acquired during diastole from image reconstruction and parameter fitting. Furthermore, it was shown that the DC signal can be used for retrospective cardiac self-gating. Admittedly, the ECG signal that was recorded during the experiment was still used to trigger the IR TrueFISP experiment at the beginning of the diastole. In a future study, a prospective implementation of the self-gating procedure may potentially be used instead. However, as can be seen in Figure 15c and although the temporal dynamics of the IR TrueFISP experiment are largely removed from the DC signal by the biexponential fitting procedure, very fast dynamics make the determination of the gating window early in the beginning of the experiment difficult. Nevertheless, the DC self-gating signal quickly improves making it possible to determine the gating window for earlier time points by extrapolation from the more reliable self-gating signal later in time.

In addition to the T_1 and T_2 quantification errors that were noticed in the results of the brain experiments, the cardiac IR TrueFISP experiment suffers from another systematic quantification error: Through plane motion during the systolic phase can lead to a violation of the steady state condition of the IR TrueFISP experiment in some parts of the cardiac muscle. The relative signal change caused by this depends on the slice thickness as the effect of through plane motion on imaging is expected to scale inversely with slice thickness. Further observation and investigation of through plane motion effects on the IR TrueFISP quantification method is left for a future study.

3.6 CONCLUSION

The results show that it is possible to derive T_1, T_2 and relative proton density from a single radial IR TrueFISP experiment of the human brain in about 6 s per slice by using a golden-ratio-based profile order in combination with view-sharing. This represents a 20-fold improvement over the previously reported, 2 min/slice obtained with a segmented Cartesian acquisition [50, 52]. This critical improvement in the speed of the parameter mapping experiment allows whole head coverage (20-30 slices) in 2-3 minutes, making quantitative and synthetic imaging clinically viable. However, differences in contrast between synthetically generated images and their respective reference images hints to systematic T_1 and T_2 quantification errors that require further investigation.

Furthermore, the results from the cardiac experiment show that the proposed radial IR TrueFISP method is well suited for cardiac relaxometry. It was possible to obtain proton density, T_1 and T_2 from a single-shot IR TrueFISP experiment in combination with a retrospective gating technique.

4

EFFECTS OF SLICE PROFILE AND MAGNETIZATION TRANSFER ON IR TRUEFISP RELAXOMETRY

4.1 INTRODUCTION

It was shown in Chapter 3 that the IR TrueFISP method can be significantly accelerated using a radial readout with golden-ratio based profile order in combination with view-sharing. However, the presented results indicate that IR TrueFISP generally suffers from systematic quantification errors. Specifically, gray/white matter contrast in FLAIR and T_2-weighted images, synthetically generated from the IR TrueFISP relaxometry data, was found to be different from corresponding spin-echo reference images. The aim of the work presented in this chapter is to provide explanations and correction strategies for this deviation. Particularly, two major sources of error for IR TrueFISP relaxometry are examined and addressed.

A potential problem in mapping proton density, T_1 and T_2 with an IR TrueFISP experiment is that on-resonant magnetization transfer (MT) effects can have a significant influence on the steady state signal of bSSFP sequences [62], and can thus potentially confound the experiment. In this work, MT effects on parameter quantification are examined by variation of the RF pulse duration, as previously proposed by Bieri et al. [63]. A strategy is presented that partially corrects the obtained parameter maps for MT effects by extrapolation of the results from multiple IR TrueFISP experiments towards a MT-free.

Additionally, deviations of the excited slice profile from a perfect rectangular form pose another serious problem for accurate quantification, since the IR TrueFISP method relies on the correct knowledge of the excitation flip angle. In order to correct for non-rectangular slice profiles, an effective flip angle is introduced, derived from a simulation of the IR TrueFISP experiment.

With these corrections, the technique has been tested in a phantom and in *in vivo* experiments and shown to yield parameters which are similar to those derived using standard quantification experiments. This work shows that the golden angle radial IR TrueFISP method is a viable option for quantitative MRI due to significantly shorter scan times while still allowing accurate parameter quantification.

A Full Paper on this work together with results from Chapter 3 is currently under review in the journal *Magnetic Resonance in Medicine.*

4.2 THEORY

4.2.1 *Slice profile effects*

As discussed in Section 2.3.1, selective excitation of an imaging slice in MRI is achieved by simultaneous application of a frequency-selective RF pulse and a magnetic field gradient. However, in reality, slice selection does not lead to perfectly homogeneously excited slices. The nominal flip angle is only reached in the center of the excited slice (assuming a perfectly homogeneous B_1 field); the actual flip angle in most parts of the slice is significantly smaller. In first approximation, and for small flip angles ($\alpha \ll 90°$), the profile of the excited slice is given by the Fourier transform of the RF pulse waveform. The waveform of a sinc pulse can be described by the product of its duration and its bandwidth (time-bandwidth product TBW):

$$B_1(t) = \begin{cases} A \cdot \frac{T_{RF}}{TBW} \cdot \frac{\sin(\pi t \cdot TBW/T_{RF})}{\pi t} & -\frac{T_{RF}}{2} < t < \frac{T_{RF}}{2} \\ 0 & \text{otherwise} \end{cases} \tag{4.1}$$

where the amplitude in the center of the RF pulse is denoted as A and the RF pulse duration as T_{RF}. Note that the sinc pulse waveform is usually filtered by a Hamming or Hann window function. For even integer values, the TBW is equal to the number of zero crossings of the RF pulse waveform. Thus, a sinc pulse with a high TBW includes many sidelobes, leading to a slice profile that approaches a rectangular form. However, increasing the TBW of the RF pulse increases the bandwidth of the pulse (assuming constant RF duration), leading to two major disadvantages: First, it requires an increase of the slice selection gradient's amplitude, which may cause problems with gradient amplitude overflow and general sequence timing. Second, it leads to an approximately linear increase of the specific absorption rate (SAR) of the sequence. Thus, in many clinically used fast 2D imaging sequences, a sinc pulse with a very low TBW (between 2 and 3) is used, leading to slice profiles that are far from rectangular.

Using the nominal flip angle for 2D IR TrueFISP quantification will therefore obviously lead to errors as the underlying assumption of a perfect rectangular slice profile is significantly violated. This work shows that it is possible to correct for non-rectangular slice profiles by introducing an effective flip angle. The effective flip angle is defined as the flip angle that best describes the IR TrueFISP signal evolution for a given T_1 and T_2, assuming a perfect rectangular pulse profile ($\alpha_{effective}(T_1, T_2) < \alpha_{nominal}$). This parameter can be obtained from a simulation of the IR TrueFISP experiment using a known (i.e. calculated or experimentally determined) slice profile, as described in the methods section.

4.2.2 *Magnetization transfer effects*

Another potential problem in mapping M_0, T_1 and T_2 with an IR TrueFISP experiment is that on-resonance magnetization transfer effects can have a significant influence on the steady state signal of bSSFP sequences [62], and can thus potentially confound the experiment.

Magnetization transfer effects on MRI were first reported by Wolff and Balaban in 1989 [64]. Macromolecules (such as proteins in the human brain) are not directly detectable by most MR imaging methods. Typical RF excitation pulses are much longer than the transverse relaxation time (T_2) of typical macromolecules so that no detectable transverse magnetization is created in the macromolecular spin pool. However, RF pulses lead to a saturation of the longitudinal magnetization which is indirectly detectable: Saturation of longitudinal magnetization is transferred to observable spins (e.g. in water) via dipolar coupling or chemical exchange, leading to a signal loss in MR images. Henkelman et al. [65] provide an elaborate review of magnetization transfer and common methods for its qualitative and quantitative detection.

The effects of magnetization transfer on an IR TrueFISP experiment are twofold: First, it leads to a reduction of the apparent relaxation time (and fit parameter) T_1^*. Second, it reduces the steady state signal S_{StSt}. Quantification of proton density and of the signal magnitude directly after inversion, S_0, should not be significantly affected by MT since the saturation of the semi-solid spin pool at the beginning of the experiment is effectively zero. Thus, in order to correct T_1 and T_2 for MT effects, it is necessary to extrapolate S_{StSt} and T_1^* to a MT-free state.

As previously proposed [63], reducing RF power by prolonging the RF pulse in a bSSFP acquisition can be effective in reducing MT related signal loss. Stretching the RF pulse by a factor of β reduces the MT saturation rate per pulse by $1/\beta^2$, provided that the bandwidth of the pulse is much smaller than the bandwidth of the restricted spin pool causing MT (and assuming a constant flip angle) [63].

Gloor et al. [66] recently presented a modified bSSFP steady state signal equation based on a two-pool MT model. However, full quantification of all relevant MT parameters using this model requires a large number of bSSFP scans in the steady state. The associated increase in scan time may be acceptable if the quantified MT parameters are of further interest, but would otherwise largely diminish the speed advantage of the IR TrueFISP method. Bieri et al. [63] used a simple exponential model to describe the MT induced steady state signal change, and showed the experimental data are well-described using this model. Thus, the steady state signal can be partially corrected for MT using an exponential saturation model of the same general form:

$$\begin{aligned} S_{StSt}(\beta) &= \left(S_{StSt}^{\text{no MT}} - S_{StSt}^{\text{full MT}}\right) \cdot \left(1 - e^{-k\beta}\right) + S_{StSt}^{\text{full MT}} \\ &= \Delta S_{StSt} \cdot \left(1 - e^{-k\beta}\right) + S_{StSt}^{\text{full MT}} \end{aligned} \tag{4.2}$$

$S_{StSt}^{\text{no MT}}$ denotes the steady state signal extrapolated to an RF pulse of infinite duration ($\beta \to \infty$, free of MT effects), and $S_{StSt}^{\text{full MT}}$ denotes the signal arising from a fully saturated semi-solid spin pool, i.e. the remaining observable signal depends primarily on the exchange rate between the spin pools and the T_1 relaxation time of the free spins. The empirical rate constant k describes the exponential relaxation towards $S_{StSt}^{\text{no MT}}$ with increasing β. Thus, this simple model describes an exponential transition from the steady-state signal with fully saturated semi-solid spin pool ($S_{StSt}^{\text{full MT}}$) to the MT-free signal ($S_{StSt}^{\text{no MT}}$). The empirical rate constant k of this transition is determined by MT-related parameters, mainly the exchange rates between the spin pools and their relaxation properties. By acquiring bSSFP images with at least three different pulse durations, it is possible to determine all three relevant parameters $S_{StSt}^{\text{no MT}}$, $S_{StSt}^{\text{full MT}}$, and k by performing a fit to the equation shown above. MT-related effects on the IR TrueFISP method can be reduced by using the extrapolated steady state signal $S_{StSt}^{\text{no MT}}$ in the calculation of T_1 and T_2.

The effect of MT on T_1^* is generally smaller than on S_{StSt}. Additionally, slight T_1^* deviations are less problematic for IR TrueFISP quantification. Since each additional degree of freedom in the quantification leads to noise amplification, MT-related effects on T_1^* are simply reduced in this work by using T_1^* from the experiment that was least affected by MT (i.e. from the scan with the highest β).

Since S_0 should not be affected by MT, it is possible to use S_0 from any of the IR TrueFISP experiments for the final calculation of the relaxation parameters. In this work, S_0 from the shortest TR scan is used, since it shows the least blurring due to the higher sampling rate.

4.3 METHODS

4.3.1 *Imaging experiments*

Phantom experiments were performed on a 1.5 T whole-body imaging system (Magnetom Avanto, Siemens Healthcare, Erlangen, Germany) with a six-channel phased-array body matrix in combination with a spine matrix coil (Siemens Healthcare). Phantom experiments were performed in order to examine the validity of the radial IR TrueFISP and the slice profile correction method. To this end, seven 150 ml plastic bottles were filled with tap water and different amounts of a superparamagnetic iron oxide (SPIO) based contrast agent (Resovist, Bayer Schering Pharma AG, Berlin, Germany). The concentration of the contrast agent was varied between 0 and $256 \cdot 10^{-6}$ M to yield T_1

values ranging from 316 to 2440 ms, and T_2 values ranging from 15 to 1680 ms. In order to reduce susceptibility related artifacts, the phantom bottles were placed in a water-filled basin. A radial IR TrueFISP experiment with a golden-ratio based profile order was performed with the following parameters: TR = 3.12 ms, flip angle (FA) = 45°, RF pulse duration (T_{RF}) = 0.8 ms, TBW = 2, matrix size = 128x128, field of view (FoV) = 200x200 mm^2, slice thickness = 10 mm, receiver bandwidth = 1000 Hz/pixel, total number of projections acquired = 1800, total experiment time = 5.7s.

As a reference, the longitudinal and transversal relaxation times of the phantoms were measured with a Cartesian spin-echo (SE) sequence. Longitudinal relaxation was assessed from images acquired at five different inversion times (TI = 25/100/400/1200/5000 ms, TR = TI + 10 s, TE = 15 ms, 4/5 rectangular FoV = 200x159 mm^2, matrix size = 128x77 (75% phase resolution)). After adiabatic inversion and subsequent inversion delay TI, a single k-space line was acquired, followed by a relaxation delay of 10 s before the next TR. Transverse relaxation was assessed from SE images acquired with five different echo times (TE = 13/50/150/400/800 ms, TR = 5 s, 4/5 rectangular FoV = 200x159 mm^2, matrix size = 128x77 (75% phase resolution)). Reference values for T_1 and T_2 were calculated from the corresponding phase-corrected real-part image series by three- and two-parameter fitting, respectively. For further analysis, a region-of-interest was drawn in each phantom bottle. Mean and standard deviation of T_1 and T_2 were then determined from these ROIs for the reference and the IR TrueFISP experiment, with and without correction for slice profile imperfections, which are described below.

In order to correct for slice profile imperfections, quantitative slice profiles for a sinc pulse (TBW = 2, FA = 45°, 60°) were obtained using a phantom containing a solution of 1.25 g NiSO4x6H2O and 0.5 g NaCl per 1000 g distilled water (T_1 = 300 ms). The signal time course for the IR TrueFISP experiment was simulated for different T_1 and T_2 combinations using Eq. 3.1 (nominal flip angle = 45°, 60°; TR = 5 ms) and different positions in the experimentally determined slice profiles. The effective flip angle for a given T_1, T_2, and slice profile was then obtained by fitting the sum of the signal over the slice to Eq. 3.1, with the effective flip angle as the only fitting parameter. To reduce computation time, a look-up table of effective flip angles was then generated for a wide range of T_1 and T_2 values (T_1 = 20 to 8000 ms; T_2 = 5 to 2000 ms). This table was used to correct the phantom and *in vivo* data for imperfect slice profiles, as described below.

In vivo experiments were performed on a 1.5 T whole-body imaging system (Magnetom Espree, Siemens Healthcare, Erlangen, Germany) with a 32-element phased-array head receiver coil (Siemens Healthcare). IR TrueFISP experiments were performed on six asymptomatic volunteers. Informed consent was obtained and the project was approved by the local Institutional Review Board (IRB). After non-selective adiabatic inversion, a linearly increasing flip angle preparation consisting of 4 pulses was used to suppress off-resonance oscillations [53]. After this preparation the return to

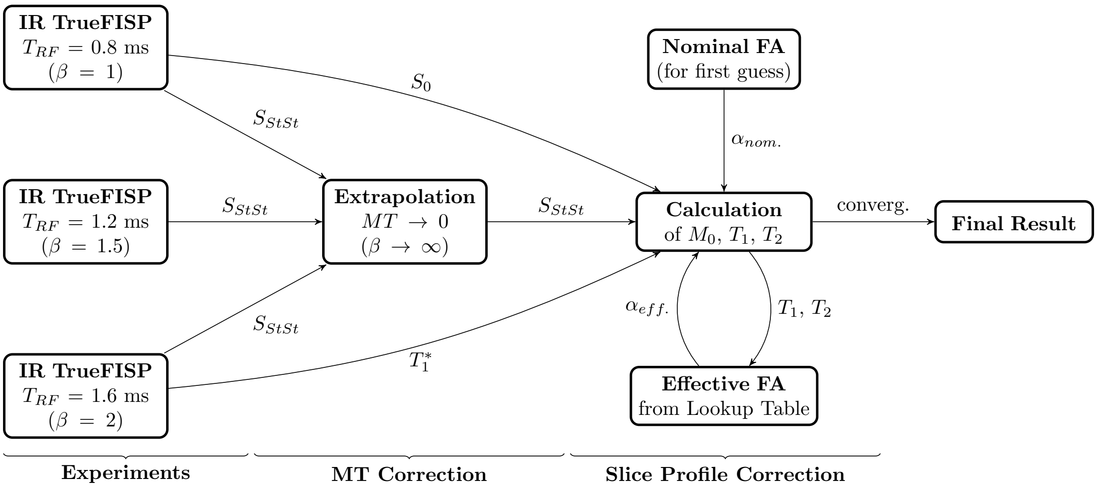
IR TrueFISP
T_{RF} = 0.8 ms
(β = 1)
IR TrueFISP
T_{RF} = 1.2 ms
(β = 1.5)
IR TrueFISP
T_{RF} = 1.6 ms
(β = 2)
S_0
S_{StSt}
S_{StSt}
S_{StSt}
S_{StSt}
T_1^*
Extrapolation
$MT \to 0$
($\beta \to \infty$)
Nominal FA
(for first guess)
$\alpha_{nom.}$
Calculation
of M_0, T_1, T_2
converg.
Final Result
$\alpha_{eff.}$
T_1, T_2
Effective FA
from Lookup Table
Experiments
MT Correction
Slice Profile Correction

Figure 19: Flow chart of the proposed corrections for IR TrueFISP quantification: After running three separate IR TrueFISP experiments with varying RF pulse durations and after performing fits to Equation 3.1, the steady state signal is extrapolated to the MT-free state. Using this extrapolation together with T_1^* from the scan that was least affected by MT, and S_0 from one of the scans (using S_0 from the scan with shortest TR reduces blurring), first estimates of T_1 and T_2 are obtained, that are iteratively corrected for slice profile imperfections using a lookup table in the following. Convergence is achieved when the mean change of the effective flip angle is below 1 % between iterations.

equilibrium was observed using a radial bSSFP sequence with a golden-ratio based profile order.

In order to examine the influence of magnetization transfer on parameter quantification, the IR TrueFISP experiment was repeated with different pulse durations and repetition times. To keep the recently reported effect of finite RF excitation on the bSSFP signal [67] constant for all scans, the ratio between pulse duration and TR was kept fixed at 20%. The acquisition parameters used are as follows: TR = 4, 6, 8 ms, pulse duration T_{RF} = 0.8, 1.2, 1.6 ms (rf-scaling factor β = 1, 1.5, 2), TBW = 2, FA = 60°, matrix size: 256x256, FoV = 220x220 mm^2, slice thickness = 6 mm, receiver bandwidth = 890 Hz/pixel. The total number of projections was adjusted so that the total acquisition time was just under 6 s for each experiment.

4.3.2 *Signal Processing and Parameter Fitting*

After the data were acquired, they were used to determine the first estimates of T_1, T_2 and M_0. First, for each individual time frame, adjacent projections were selected and filtered using the KWIC filter described in chapter 3. Each frame contained 8 projections in the center of k-space and reconstruction windows for consecutive frames were separated by these 8 projections. Moving further out in k-space, the number of projections jumps to the next Fibonacci number (i.e. 13, 21, 34, 55, etc., up to a maximum of 233 projections), whenever the Nyquist criterion would be violated otherwise. Images were reconstructed from these filtered projections using NUFFT gridding [31] and an analytically calculated density compensation function. Multi-channel images were combined using the adaptive combine method of Walsh et al [59]. The resultant time series of images was used to determine values for the parameters M_0, T_1 and T_2 by fitting the data pixel-wise to equation 3.1. After the determination of the values of M_0, T_1 and T_2 for each of the different pulses described above, the next step is to correct for MT effects and slice profile imperfections. A flow chart showing how these corrections were performed is given in Figure 19. Using the steady state signals from the three different pulse lengths, the MT-free signal $S_{StSt}^{\text{no MT}}$ was determined using the exponential model (Eq. 4.2). MT-corrected T_1 and T_2 maps were then calculated as described in the theory section, using the corrected steady state signal $S_{StSt}^{\text{no MT}}$, T_1^* from the scan that was least affected by MT ($\beta = 2$), and the proton density map from the scan with the shortest TR (TR = 4 ms). The result of this correction is a set of M_0, T_1 and T_2 maps that are less affected by magnetization transfer. After these initial estimates of the MT-free T_1 and T_2 values are determined using the nominal flip angle, parameter maps were iteratively corrected to account for the imperfect slice profile. Using the initial fit, an estimate of the effective flip angle is obtained from the look-up table. Proton density, T_1 and T_2 were then corrected and the effective flip angle was updated using the corrected T_1 and T_2 values. This procedure was iterated four times until convergence was achieved (mean effective flip angle changes by less than 1 %). Total computation time for the iterative slice profile correction was under 0.1 s per slice on a standard desktop computer running unoptimized Matlab code.

4.4 RESULTS

In order to correct for slice profile imperfections, the signal evolution for an IR TrueFISP experiment was simulated using the experimentally determined slice profile arising from a sinc pulse ($\alpha_{nominal} = 60°$, TBW = 2) for spins with the following relaxation times: T_1 = 600 ms, T_2 = 60 ms. The signal time course as a function of the position in the slice is shown in Figure 20a. Figure 20b depicts the integral of this signal over the slice, as well as an exponential fit used to determine the effective flip angle. The effective flip angle for a nominal flip angle of 60° and the range of relaxation times described above, derived from performing the simulation with different relaxation parameters, is shown in Figure 22a. Figure 22b shows the iteratively determined map of effective flip angles for one of the six volunteers. As can be seen, the variations of the effective flip angle between different brain tissue types are relatively small.

Figure 21 gives an overview of the results from the IR TrueFISP phantom experiments, shown in more detail in Table 2. In this figure, the reference T_1 and T_2 values are plotted against the T_1 and T_2 values derived from the IR TrueFISP experiment. Re-

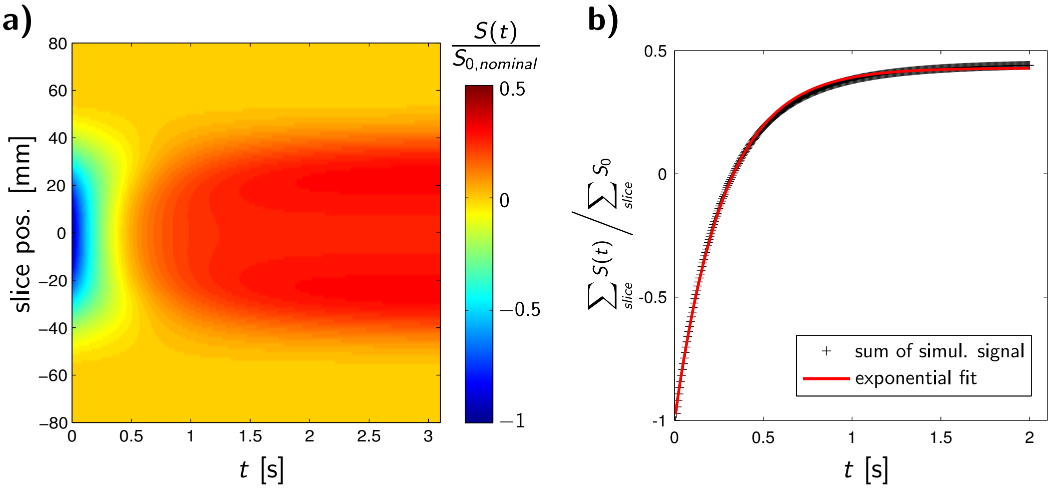

Figure 20: a) Simulated signal evolution for an IR TrueFISP experiment depending on slice position (T_1/T_2 = 600/60 [ms], sinc pulse with TBW = 2; slice thickness = 50 mm; nominal flip angle = 60°), b) sum over slice of simulated signal and exponential fit through simulated data points.

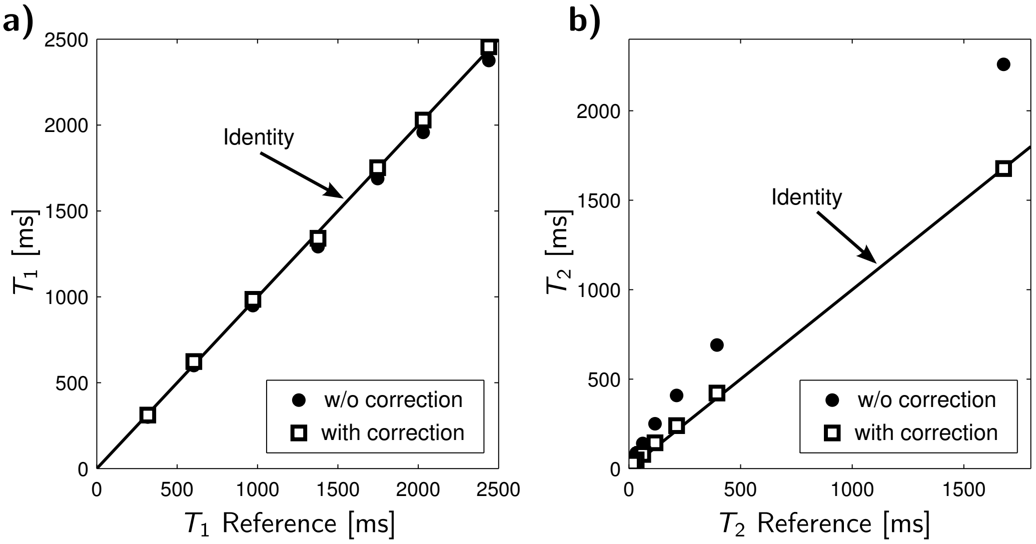

Figure 21: Phantom results: T_1 and T_2 values from all phantoms with and without correction for imperfect slice excitation over the corresponding reference values (for a better distinction of short T_2 species, see Table 2). Magnetization transfer plays no role in the phantom experiments, so there was no need for a MT correction.

	T_1 [ms]			T_2 [ms]		
	w/o corr.	*with corr.*	*reference*	*w/o corr.*	*with corr.*	*reference*
Bottle 1	2376 ± 12	2456 ± 12	2439 ± 16	2260 ± 250	1680 ± 240	1678 ± 59
Bottle 2	1958 ± 11	2029 ± 11	2030 ± 18	691 ± 21	420 ± 20	349.2 ± 7.7
Bottle 3	1689 ± 11	1752 ± 11	1747 ± 8	409 ± 13	240.1 ± 8.1	213.4 ± 4.8
Bottle 4	1292 ± 13	1341 ± 13	1376 ± 8	251 ± 10	144.3 ± 6.1	116.6 ± 2.4
Bottle 5	949 ± 14	985 ± 14	971 ± 9	140.6 ± 5.3	79.2 ± 3.1	61.7 ± 1.6
Bottle 6	600 ± 14	623 ± 14	604 ± 12	87.1 ± 4.8	48.7 ± 3.8	32.2 ± 1.2
Bottle 7	300.0 ± 9.3	312 ± 10	317 ± 15	53.4 ± 6.5	30.4 ± 4.1	15.4 ± 1.9

Table 2: Phantom data: T_1 and T_2 for all seven phantom bottles, with and without correction for imperfect slice excitation, and corresponding reference values. (Mean ± SD).

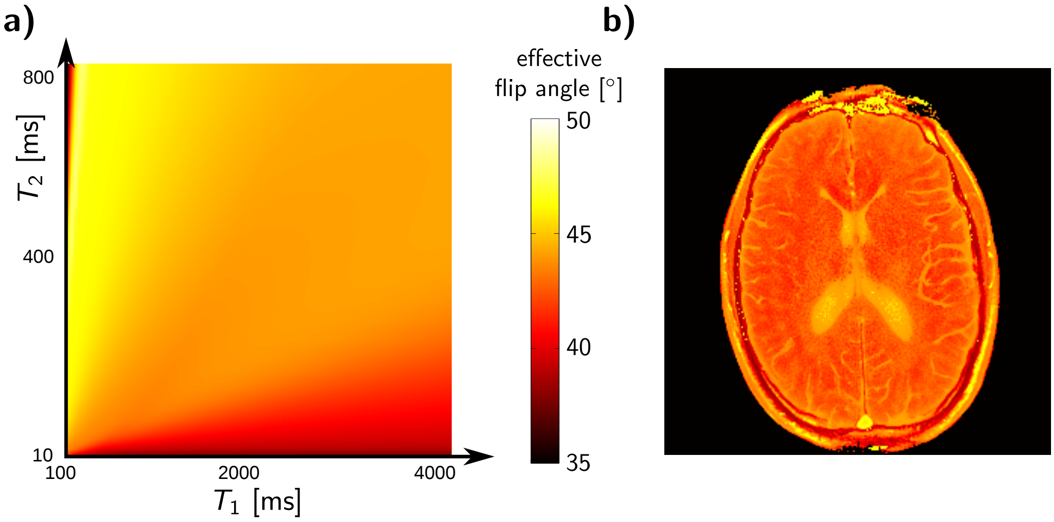

Figure 22: a) Effective flip angle lookup table determined from the fit for different T_1, T_2 combinations. b) Iteratively determined map of effective flip angles for one of the volunteers (same scaling as b).

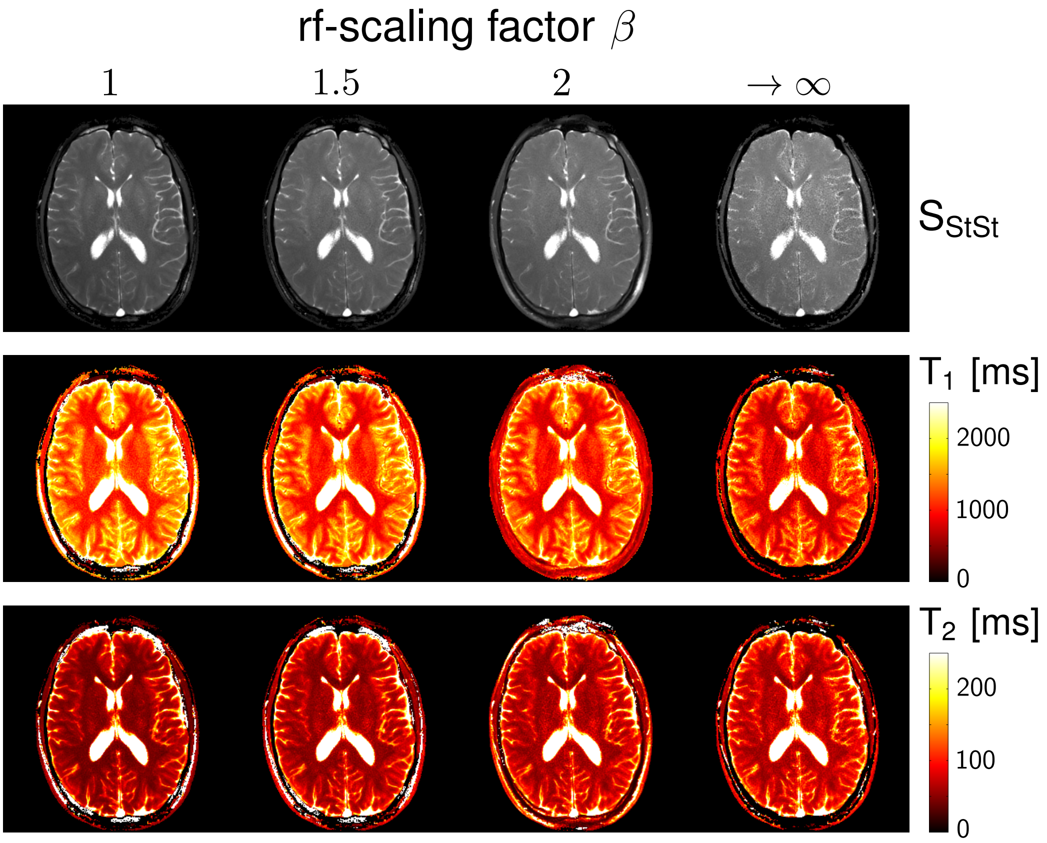

Figure 23: From top to bottom: steady state signal, T_1, and T_2 maps, as obtained from a 3-parameter fit, for three experiments with different rf-scaling factors β and thus MT levels (first three columns), as well as extrapolated to $\beta \rightarrow \infty$ (far right column). Short pulses (small β) lead to a severe attenuation of the steady state signal due to an increased MT effect, which translates into an overestimation of T_1, and underestimation of T_2. Quantification of M_0 is not affected by MT (and is thus not shown in this figure).

sults with and without slice profile correction are shown to demonstrate the effects of including this correction method. No MT correction was required for these phantom data, and thus it was not applied.

The effect of MT on parameter quantification is illustrated in Fig. 23. The top row shows steady state images for all three IR TrueFISP experiments, as well as a theoretically MT-free steady state image, obtained by extrapolation. The two bottom rows show the resultant T_1 and T_2 maps, which illustrates that magnetization transfer leads to an overestimation of T_1 and underestimation of T_2. In white matter, T_1 is overestimated by up to 30%, and T_2 underestimated by up to 50% (depending on RF power).

Figure 24 shows the result of the parameter mapping with corrections for the slice profile and MT effects for two of the normal volunteers. To provide a quantitative comparison, white matter, gray matter, and cerebral spinal fluid (CSF) regions of interest in each volunteer were selected (shown in red in the proton density map of Figure 24; similar regions of interest were selected for maps generated from the other

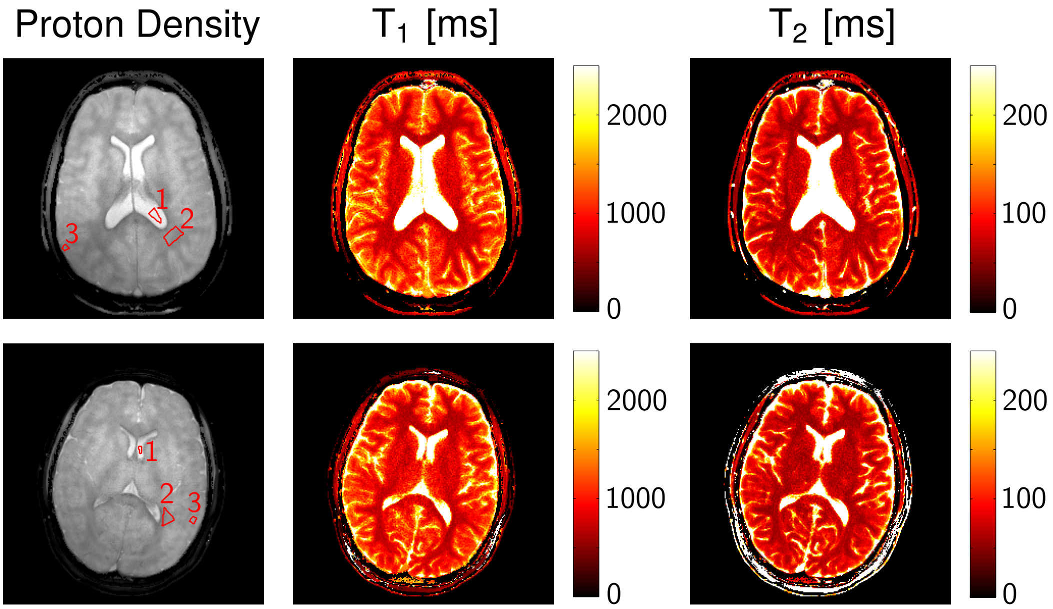

Figure 24: Parameter maps, corrected for slice profile and MT, for two of the normal volunteers. Regions of interest used for further analysis (see Table 3) are shown in the proton density maps in red; 1: CSF; 2: white matter; 3: gray matter.

volunteers). The obtained T_1 and T_2 values, corrected for slice profile and MT, for each region are detailed in Table 3. In one case it was not possible to find a region-of interest containing pure CSF due to through-plane partial volume effects, leading to the exclusion of this dataset in the calculation of the mean CSF relaxometry data.

4.5 DISCUSSION

While parameter mapping with an IR TrueFISP based scheme has been previously demonstrated [50, 52], the introduction of a golden-ratio based radial readout with a temporal k-space filter, as presented in Chapter 3, greatly accelerates this technique, bringing the time required for parameter estimation down to 6 s/slice. However, deviations from traditional theory due to magnetization transfer effects and imperfect slice profiles leads to considerable quantification errors independent of the chosen k-space sampling scheme. Thus, corrections for these two effects must be included in the IR TrueFISP quantification technique, which increases the scan time from 6 to 28 s/slice, including a relaxation delay of 5 s between IR TrueFISP experiments. The extra time due to the relaxation delay can be avoided by using an interleaved multi-slice acquisition, reducing the scan time to 18 s/slice.

The influence of magnetization transfer on parameter quantification is especially apparent when using high-power pulses (high flip angle and high bandwidth) and short repetition times. In an IR TrueFISP experiment, the magnetization transfer builds up simultaneously with the relaxation of the signal towards the steady state, potentially distorting parameter quantification. The effect of MT on parameter quantification

	T_1 *[ms]*	T_2 *[ms]*
White matter (dorsal)	716 ± 23	65.0 ± 3.5
previously reported	$608 - 756$	$54 - 81$
Gray matter	1123 ± 36	88.0 ± 4.5
previously reported	$998 - 1304$	$78 - 98$
CSF	4200 ± 400	2100 ± 360
previously reported	4103 ± 904	
	5127 ± 350	

Table 3: Volunteer data: Parameters obtained from ROIs positioned in different parts of the brain (Mean ± SD over six volunteers / 5 volunteers in case of CSF), corrected for slice profile inaccuracies and magnetization transfer. References for previously reported T_1 values are: [37, 49, 68, 69, 70, 71, 72]; and for T_2: [37, 49, 72, 73].

was examined in this work by varying the duration of the RF pulse, as proposed previously [63]. However, in order to limit the recently reported influence of finite RF excitation on bSSFP [67, 74], it was necessary to keep the T_{RF}/TR ratio fixed at a relatively low value, which limited the feasible range of T_{RF} values and thus the dynamic range that was available for MT extrapolation. Nonetheless, extrapolation of the steady state signal towards the MT-free state was relatively stable, although it did lead to a noticeable noise increase in the MT-corrected parameter maps (compare raw parameter maps with corrected (extrapolated) maps on the far right of Figure 23). The influence of finite RF excitation on parameter quantification (and thus the necessity to keep the TRF /TR ratio low) may be avoided in a future study using the very recently proposed concept of superbalanced SSFP [75]. This concept allows the use of much longer RF pulses by overcoming the problem of finite RF effects, potentially eliminating the need for MT correction based on an extrapolation from multiple experiments.

Due to the relatively low influence of MT-related T_1^* deviations on parameter quantification and in order to avoid further SNR loss as a result of additional degrees of freedom, T_1^* was not extrapolated to a MT-free state. MT effects on T_1^* were simply reduced by using the value from the scan that was least affected by MT (highest β). In principal, this approach requires only two traditional bSSFP acquisitions in the steady state with different RF pulse durations, in addition to the fit parameters from a single IR TrueFISP experiment. This strategy is more time-efficient than performing three separate IR TrueFISP experiments, reducing the acquisition time penalty of the proposed MT correction method: Assuming that one steady-state image can be acquired in 3 s, this decreases the required imaging time per slice from 18 s to 12 s. In many cases, it may also be viable to simply limit MT related quantification errors by running a single IR TrueFISP experiment with relatively long RF pulses and low flip angles.

MT and slice-profile corrected quantitative results for ROIs in white matter (WM), gray matter (GM), and CSF are detailed in Table 3. This table shows that the T_1 values in white and gray matter obtained from the radial IR TrueFISP method were 716 ± 23 ms and 1123 ± 36 ms (mean ± standard deviation between data from six volunteers), respectively, which are in good agreement with the published literature [37, 49, 68, 69, 70, 71, 72]. Similarly, measured T_2 values were 65.0 ± 3.5 ms and 88.0 ± 4.5 ms in white and gray matter, respectively, again consistent with those reported previously in the literature [37, 49, 72, 73]. The obtained T_1 and T_2 values in CSF were 4200 ± 400 ms and 2100 ± 360 ms, respectively.

Figure 21 and Table 2 show that the values of the parameters obtained using this method in a phantom study are generally consistent with the values derived from spin-echo sequences. However, in vials with very high contrast agent concentrations and very low T_1 and T_2 values, T_2 is increasingly overestimated, even after correcting for slice profile imperfections (see Table 2). This may be explained by the fact that the faster dynamics due to the shortened T_1^* (induced by short T_1 and T_2) cannot be fully captured by the temporal k-space filter. Additionally, the very fast dynamics directly after the inversion pulse are temporally smoothed, leading to an underestimation of S_0. This then causes an underestimation of M_0 and overestimation of T_2 during the calculation of the relaxation parameters. In contrast, the influence of an underestimated proton density on the quantification of T_1 is rather small. Another potential contributing factor to the overestimation of T_2 in short T_2 species is the deviation of the bSSFP signal from traditional theory, derived using the assumption of instantaneous RF excitation [67, 74]. It is important to note that magnetization transfer does not affect the phantom experiments since there is no restricted spin pool (the phantom did not contain a significant quantity of macromolecules).

The proposed correction for slice profile imperfections relies on the assumption that the sum of exponentials from different parts of the slice can be described by a single exponential. Simulation results show that this assumption holds true in good approximation for typical excitation profiles and physiological T_1/T_2 combinations (an example is shown in Fig. 20b). The validity of the slice profile correction is further supported by the results from the phantom experiments. As shown in Figure 21a and Table 2, T_1 values obtained from the IR TrueFISP experiment are in excellent agreement with the reference at all seven contrast agent concentrations. After correcting for slice profile imperfections, the agreement is further improved. The necessity for slice profile correction is particularly obvious when looking at T_2 values in Figure 21b. Without correction, T_2 values are substantially overestimated compared to the reference values. The proposed slice profile correction reduces this deviation from the reference, particularly for long T_2 species. It was observed that the effective flip angle shows only a small T_1/T_2 dependence in tissue. In this study, the effective flip angle was found to be between 42 to 44° for white and gray matter, and between 44 to 45° in CSF (for a nominal FA = 60°, TBW = 2, see Figure 20d). Since the effective flip angle is essentially constant regardless of tissue type, it could be reasonable to use a predetermined single effective flip angle for slice profile correction, instead of the iteratively determined map of effective flip angles. An alternative to slice profile correction is to move to a true 3D acquisition. The flip angle that is used in parameter calculation can then be adjusted for every voxel according to its position inside the excited slice (taking advantage of the additional spatial encoding in slice direction), making slice profile correction unnecessary.

An inhomogeneous B_1 excitation field will result in quantification errors that are similar to those discussed in the case of imperfect slice profiles (i.e. the errors will mainly be notable in the quantification of T_2 values). Fortunately, the B_1 excitation field is expected to be relatively homogeneous over the whole brain for the body coil (a typical birdcage coil) at field strengths of 1.5 T ($\approx$64 MHz) and below [76]. Thus, observation of quantification errors due to B_1 field inhomogeneity was not a focus of this study. However, at higher field strengths, an additional B_1 field mapping scan may be necessary in order to achieve accurate T_2 quantification.

It is widely known that bSSFP is very susceptible to off-resonance frequencies. In addition to the obvious problem of banding artifacts, off-resonances can lead to errors in parameter quantification, by altering the steady state signal and the transient signal response of the bSSFP sequence [77]. This can be problematic for slices that are placed in the lower part of the brain, close to the nasal cavities and the ear canal. In this case, additional field mapping scans may be required to account for off-resonance effects. In the experiments shown in this work the shim was relatively homogeneous throughout the slice, with an off-resonance frequency range of approximately $\pm$20 Hz in brain tissue.

4.6 CONCLUSION

As shown in Chapter 3, the IR TrueFISP method can be significantly accelerated using a radial readout with golden-ratio based profile order in combination with view-sharing. The proposed method allows the quantification of a full set of relaxometry data (proton density, T_1 and T_2) in 6 s per slice. However, the work presented in this chapter shows that corrections are necessary to improve the accuracy of values determined using this method. The proposed corrections increase the total scan time per slice from 6 s to 12-18 s.

Magnetization transfer leads to a considerable overestimation of T_1 and underestimation of T_2 in these experiments. These errors can be effectively reduced by lengthening the RF pulse or partially compensated using the corrections shown here. Although this correction requires multiple scans and can lead to a loss in SNR due to the additional degrees of freedom, the resulting scan time and image quality are still acceptable. Additionally, slice profile imperfections can lead to a significant overestimation of T_2. This effect was corrected by introducing an effective flip angle, derived from simulations of the experiment. With these corrections, the technique has been tested in a phantom and in *in vivo* experiments and shown to yield parameters which are similar to those derived using standard quantification experiments.

This work shows that the golden angle radial IR TrueFISP method is a viable option for quantitative MRI due to significantly shorter scan times while still allowing accurate parameter quantification.

Part II

Dynamic MRI Thermometry

5

DYNAMIC MRI THERMOMETRY DURING RF HEATING

5.1 INTRODUCTION

Radio frequency (RF)-induced heating of tissue adjacent to conductive medical implants is a growing concern in magnetic resonance imaging. RF-induced currents in the elongated electrodes of cardiac pacemakers, implantable cardioverter-defibrillator, or deep brain stimulators are especially problematic, as they can lead to severe tissue burns close to the tips of the electrodes. Currently, these heating effects can only be observed *in vitro* or in an animal model with the help of a temperature probe. Fluoroptic thermometers and thermocouple wires are commonly used to measure the RF-induced temperature increase in MR-safety studies [78, 79]. A major drawback of these probes is that they only provide a local temperature reading, making it difficult and time-consuming to investigate heating effects of implants with complex geometries. Another problem is that the exact position of the probe can have a high impact on the observed temperature increase. It has been shown that relatively small positioning changes can lead to temperature deviations of up to 45%, even if the probe is directly attached to the heating source [80].

An alternative to this local thermometry approach, is to use MRI for the temperature measurement. In a prior study, the MRI-induced temperature increase was observed by a separate MRI thermometry sequence [81]. Specifically, a HASTE imaging sequence was followed by MRI thermometry. This approach has several drawbacks; temperature dynamics are almost impossible to monitor, and heat dissipation following the interruption of the heat-inducing MR imaging sequence leads to an underestimation of the observed temperature increase. Using an external RF transmitter for RF-heating, while monitoring the temperature increase with a standard MRI thermometry sequence, can solve these issues [82]. However, this approach makes it impossible to monitor the heating effects of an MRI sequence or of the RF transmitter coil of the MRI system.

In this chapter, a new approach for MRI thermometry is described, that allows MRI thermometry during RF heating caused by the MRI sequence itself. Specifically, a proton resonance frequency (PRF) shift MRI thermometry method [83] was combined with an MRI heating sequence. This method provides a map of temperature changes induced by the heating part of the sequence, with a, within limits, freely adjustable RF power. The method was validated in a gel phantom, with a copper wire serving as a simple model for a medical implant. The results were compared with the readings from a fluoroptic temperature probe.

Site	**Dose**	**Time (min)** *equal to or greater than*	**SAR (W/kg)**
whole body	averaged over	15	4
head	averaged over	10	3
head or torso	per gram of tissue	5	8
extremities	per gram of tissue	5	12

Table 4: List of FDA recommended SAR Limits during an MRI scan [85].

This work has been published as a Technical Note in the journal *Magnetic Resonance in Medicine* [84].

5.2 THEORY

5.2.1 *Specific Absorption Rate (SAR)*

As a result of the dielectric and resistive properties of biological tissue, most of the transmitted RF energy during an MRI examination is absorbed by the body of the patient and transformed into heat. For safety reasons, these heating effects have to be restricted. The Specific Absorption Rate (SAR) is commonly used as a measure to impose limits on the transmitted RF power. The SAR is defined as the total dissipated RF energy E over exposure time t_{exp} and unit mass M:

$$\mathrm{SAR} = \frac{E}{t_{exp} M} \tag{5.1}$$

SAR is usually differentiated into local and global SAR. Global SAR is averaged over the whole (or parts of the) body, while local SAR is given by the maximum of the SAR in the affected body region, averaged over a small sample volume (typically 1 or 10 g of tissue).

When multiple high-power RF pulses are played over a very short amount of time, as common in turbo-spin echo and bSSFP acquisitions, local and global SAR can be particularly high. In order to avoid severe heating of the human body during an MRI examination, the United States Food and Drug Administration (FDA) published recommendations for local and global SAR limits [85], summarized in Table 4.

5.2.2 *Amplification of Local SAR by Conductive Implants*

Global SAR restrictions are very effective in preventing dangerous levels of whole-body heating. However, local SAR depends on a number of factors that are sometimes difficult to control. A major safety concern is that conductive objects can amplify the local electric field. Local SAR hot spots can lead to severe burns of the skin (when the object is on the skin or lies on the patient, e.g. ferromagnetic tattoo pigments, RF coils, ECG leads) or burns in inner tissues (in case of conductive implants) [86].

It has been shown that, under normal circumstances, no dangerous heating is expected in patients with large compact metallic implants (e.g. prostheses, osteosynthetic plates, clips, or surgical nails) at common clinical field strengths [87]. However, elongated implants, like ICD or pacemaker leads, are of serious concern. The length of a pacemaker lead is often very close to the resonance length at the frequency of interest ($\lambda/2 = 26.3$ cm at 1.5 T and in aqueous tissue). It is important to note that the actual resonance length also depends on other factors; its orientation and its ohmic and capacitive contact to the medium, among others. Insulation of the lead ensures that most of the absorbed RF energy will concentrate at the tip of the lead, which is in direct contact with the myocardium and uninsulated for obvious reasons. The relatively high ohmic resistance of the cardiac muscle (compared to the lead) causes the induced current to be rapidly transformed into heat. This can lead to severe burns in the myocardium, that can result in a transient or permanent damage of the cardiac muscle and an increase of the pacing threshold.

5.2.3 *Basic Principles of MRI Thermometry*

MRI Thermometry relies on the fact that several MRI related parameters show a temperature dependency. The most obvious candidate is the steady state population of the two spin states (for spin 1/2 nuclei), which is directly governed by the Boltzmann distribution. However, at room temperature, the variations of the population of the spin states due to relatively small temperature variations are almost negligible. Other temperature dependent parameters are (without any claim of exhaustiveness)

- T_1 relaxation time
- T_2 relaxation time
- Diffusion constant in the medium
- Chemical shift

However, T_2 based thermometry is unfeasible due to its high non-linearity. Table 5 gives an overview of the advantages and disadvantages of commonly used MRI thermometry methods.

	Absolute or relative temperature	Linearity	Sensitivity	Spatial resolution	Temporal resolution (acq. time)	Motion artifacts	Field dependency
Diffusion	Relative	-	-/+	+	+	--	Negligible
T_1	Relative	-	-	+	+	-/+	Less at high field
PRF	Relative	++	+	+	++	-/+	Linear increase with field
Spectroscopy	Absolute possible	++	-/+	--	--	-	Linear increase with field

++ = excellent; + = good; -/+ = average; - = poor; -- = very poor

Table 5: Comparison of different MRI temperature mapping techniques [88]. Note that the PRF shift method, as well as spectroscopic MRI thermometry rely both on the temperature dependence of the chemical shift of water.

5.2.4 *Thermometry based on the water proton resonance frequency (PRF)*

According to Equation 2.7, the Larmor frequency of a spin species depends on its chemical shift δ:

$$\omega_0 = \gamma B_0 (1 - \delta)$$

The chemical shift can be separated into a temperature dependent and independent part:

$$\delta(T) = \delta_0 + \delta_T(T) \tag{5.2}$$

Fortunately, the chemical shift of water is nearly linearly dependent on temperature, allowing the following linear approximation:

$$\delta(T) \approx -\alpha T \tag{5.3}$$

with the PRF shift coefficient α (≈ -0.01 ppm/K in water and aqueous tissue). Thus, in a gradient-echo (FID) acquisition, a small change in temperature dT leads to a proportional change in image phase $d\phi$, depending on the echo time (TE) of the sequence [83]:

$$d\phi = \frac{dT}{\alpha\gamma B_0 TE} \tag{5.4}$$

It is now possible to calculate the temperature change that occurred between the acquisition of two gradient-echo images:

$$\Delta T = T - T_{ref} = \frac{\Delta\phi}{\alpha\gamma B_0 TE} \tag{5.5}$$

When the temperature of the first *reference image*, referred to as T_{ref}, is known, it is possible to obtain the absolute temperature T in the second image by a simple summation of the reference temperature and the obtained temperature change. Equation 5.5 exemplifies the need for long echo times, in order to allow accurate temperature quantification. However, long echo times result in a strong signal decay due to T_2^* relaxation. The phase difference signal-to-noise ratio $SNR_{d\phi}$ is thus dependent on the relaxation time T_2^* [89]:

$$SNR_{d\phi} \propto TE \cdot e^{-TE/T_2^*} \tag{5.6}$$

Differentiating this equation with respect to TE yields the echo time that optimizes SNR at $TE = T_2^*$.

Furthermore, when the phase changes between the two gradient-echo acquisitions become too high, phase-wrapping occurs; the effect of phase-wrapping is a direct consequence of the fact that phase changes of multiplies of 2π are indistinguishable from another. Therefore, the echo time should be chosen so that the maximum expected temperature change leads to a phase-change of less than 2π (or π in case the general direction of temperature change is unknown). Phase-unwrapping techniques [90, 91], which generally rely on some sort of prior knowledge, can help to alleviate this restriction.

5.3 METHODS

Modified rf-spoiled GRE sequence

In order to allow the adjustment of the SAR independent from the imaging protocol, a second RF pulse (sinc profile) was added in each TR of a rf-spoiled gradient-echo sequence. This *heating pulse* pulse was placed directly after refocusing of the slice gradient of the excitation pulse, inside the echo time. To assure that the heating pulse

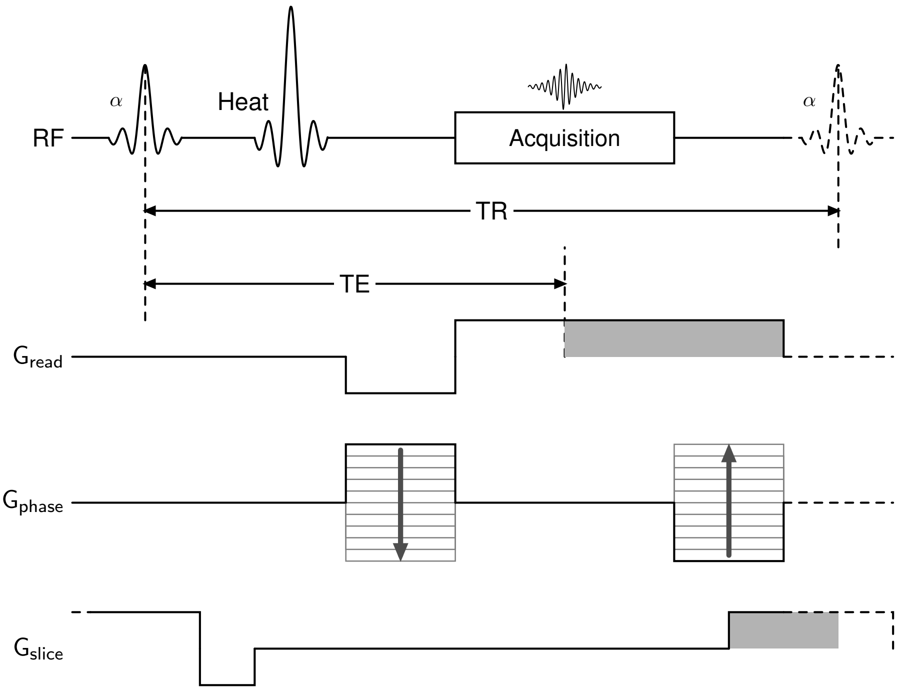

Figure 25: Diagram of GRE heating sequence. To allow long echo times while keeping TR as short as possible, the heating pulse was included inside TE, directly after slice refocusing of the excitation pulse. Shaded areas represent spoiling moments in read and slice direction, respectively.

did not affect imaging, its frequency was set off-resonant to the proton resonance frequency of water ($\nu_{\text{heating}} = \nu_{\text{water}} - 128$ kHz). It was now possible to adjust the SAR of this sequence freely (within limits) by variation of the RF power of the heating pulse. A graphical representation of this pulse sequence is given in Figure 25.

General setup

All experiments were performed on a 1.5 T whole-body imaging system (Magnetom Vision; Siemens Medical Solutions, Erlangen, Germany) with a gradient field strength of 25 mT/m and a maximum slew rate of 83 mT/m/ms. Maximum output power of the RF tube was 15 kW. For signal detection, a four-channel phased-array surface coil was used. The 350x450x160 mm^3 polyvinyl chloride phantom was filled with 20 liter hydroxyethyl-cellulose (HEC) gel (Sigma Aldrich, Steinheim, Germany). A 5% concentration of the HEC gelling agent was chosen to minimize convection effects. The gel was doped with CuSO4 (5 mmol/liter) to reduce the T_1 relaxation time to approximately 220 ms, in order to increase the signal-to-noise ratio (SNR) for short repetition times. Additionally, 1.0 g/l cooking salt (NaCl) was added to reach the desired conductivity of 0.47 S/m, which has been proposed as a reasonable value for MRI heating experiments to match organic tissue [92].

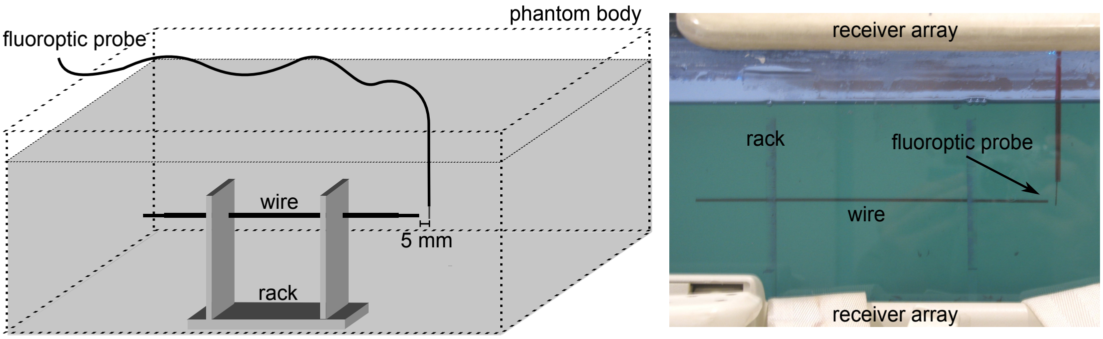

Figure 26: Left: Illustration and Right: Photo of the experimental setup. A copper wire was placed 40 mm from the left wall of a 20 l gel phantom. As a reference for temperature mapping, a fluoroptic temperature probe was positioned 5 mm in front of one of the wire tips.

Determination of the PRF change coefficient α

A fluoroptic probe was placed into the 20-liter gel phantom. The temperature of the gel inside the phantom was approximately 18°C at the beginning of the experiment. A 50-ml syringe, filled with the doped HEC gel, was heated to 50°C and then injected at the location of the fluoroptic probe, thereby forming a bubble of heated gel around the probe. Multiple repetitions of a gradient-recalled echo (GRE) sequence were running during the whole operation. Sequence parameters were as follows: FA $= 50°$, TR $= 50$ ms, TE $= 15$ ms, field of view (FoV) = 350 mm, matrix size $= 48 \times 128$ (3/8 rectangular FoV), slice thickness $= 10$ mm, acquisition time (TA) per image $= 6$ s, receiver bandwidth (BW) $= 390$ Hz/pixel.

MR Thermometry of a RF-Heated Copper Wire

A conductive wire was placed in the gel phantom, 40 mm from the left wall. The wire had a diameter of 1.2 mm and a length of 200 mm, of which the inner 180 mm were insulated by a silicone tube. To avoid susceptibility artifacts, a copper wire was chosen as a model for a medical implant. The magnetic susceptibility of copper is close to that of water (-9.63×10^{-6} vs. -9.05×10^{-6} [93]), so that no major susceptibility artifacts should be expected. For validation purposes, a fluoroptic thermometer was used (Model m3300; Luxtron, Santa Clara, CA, USA), as recommended by the American Society for Testing and Materials (ASTM) [94]. According to the manufacturer, the fluoroptic probe has an accuracy of 0.5°C within 50°C of the calibration point and a response time of 0.25 s. The probe was attached to the wire such that the end of the probe was 5 mm beyond the tip of the wire (head side of the phantom). The experimental setup is illustrated in Figure 26.

Temperature mapping was performed using the combined MRI thermometry/heating sequence, containing an off-resonant high-power RF pulse that served to heat the phantom filling. A total of 100 phase-contrast images were acquired consecutively. The slice was positioned in sagittal orientation, directly through the wire.

Other sequence parameters were as follows: FA = 30°, TR = 30 ms, TE = 20 ms, FoV = 400 mm, matrix size = 96×256 (3/8 rectangular FOV), slice thickness = 5 mm, acquisition time (TA) per image = 3.9 s, BW = 390 Hz/pixel. The averaged RF power of the experiment was set to 9 W/kg bodyweight by adjusting the flip angle of the heating pulse while observing the system's specific absorption rate (SAR) monitor. This resulted in a FA of 520°. The temperature rise was obtained by subtracting each phase-contrast image from a reference image, which yielded the change of the image phase $\Delta\phi$ in every pixel. To simplify the measurement protocol, the first acquired phase contrast image served as the reference image, so that a total of 99 temperature maps were obtained. It is important to note that there is a slight underestimation of the temperature increase because the temperature had already begun to increase during the acquisition of this reference. The temperature changes ΔT were then obtained by using Equation 5.5, using the PRF change coefficient as determined from the previous experiment.

5.4 RESULTS

The PRF change coefficient was calculated by subtracting each phase image acquired after injection of the heated gel from a reference image, acquired before the injection. The phase difference was averaged over a region of interest in the center of the "heat bubble", where the temperature distribution was expected to be uniform. The fluoroptic probe was used as a reference and provided the temperature difference between the before and after state. The PRF change coefficient was determined to be 0.00971 ppm/°C with a mean standard deviation of 0.00081 ppm/°C. This is in agreement with values for water from previous publications [83, 95].

An overlay of the last frame of the series of temperature maps, after seven minutes of RF heating, and a scout image (GRE sequence) is shown in Fig. 3. The heating effect of the wire can be clearly recognized by a temperature increase at both wire tips. Figure 28 shows the temperature of the gel as measured by a fluoroptic probe in comparison to the results of the MRI temperature measurements averaged over a region of interest. The fluoroptic probe was placed 5 mm beyond the wire tip and the region of interest consisted of two pixels approximately 4 mm beyond the tip of the wire. The exact position of the fluoroptic probe had to be excluded from the region of interest, as the probe led to signal losses at its location due to partial volume effects. The total size of the chosen region of interest was $5.0 \times 1.56 \times 3.13$ mm^3 (x, y, z axis of the scanner) compared to the diameter of the sensor of 1 mm and its sensitive length of 4 mm in the y-direction. Despite these differences in orientation and size of their respective sensitive regions, the measurements from the fluoroptic probe and MRI thermometry led to qualitatively comparable results but show quantitative differences.

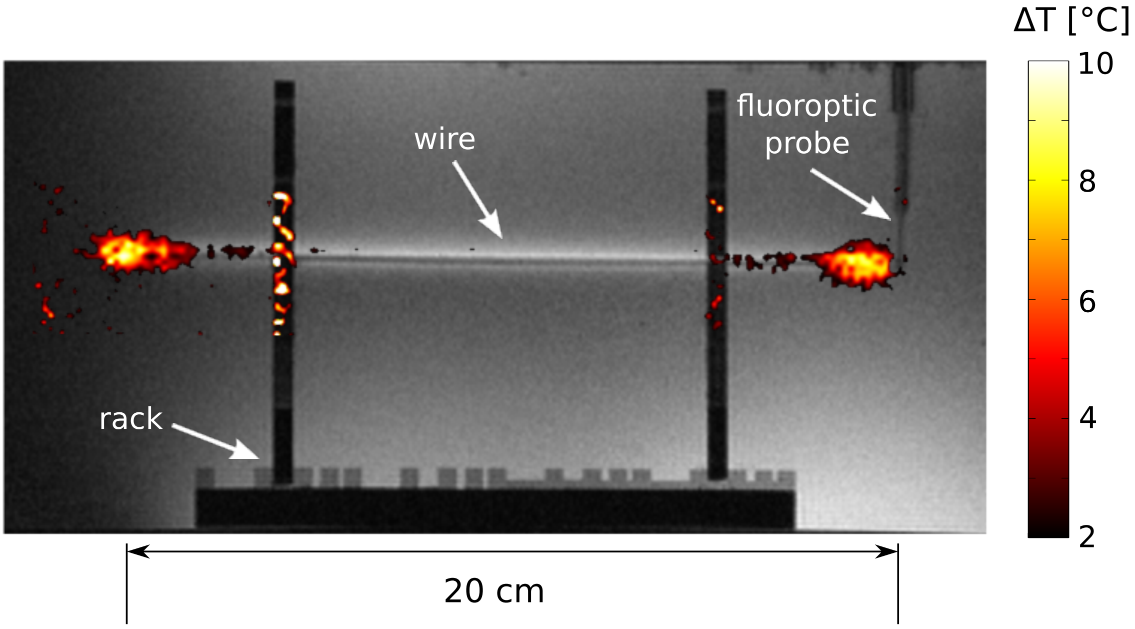

Figure 27: Overlay of a scout image and the PRF shift temperature map after the 7-min heating period. Both images were interpolated to a matrix size of 384 x 1024 (two-fold interpolation of the scout and four-fold interpolation of the temperature map). Only temperature differences larger than 2°C and in an area 20 mm adjacent to the wire are shown. Pronounced hot spots are visible at both tips of the wire.

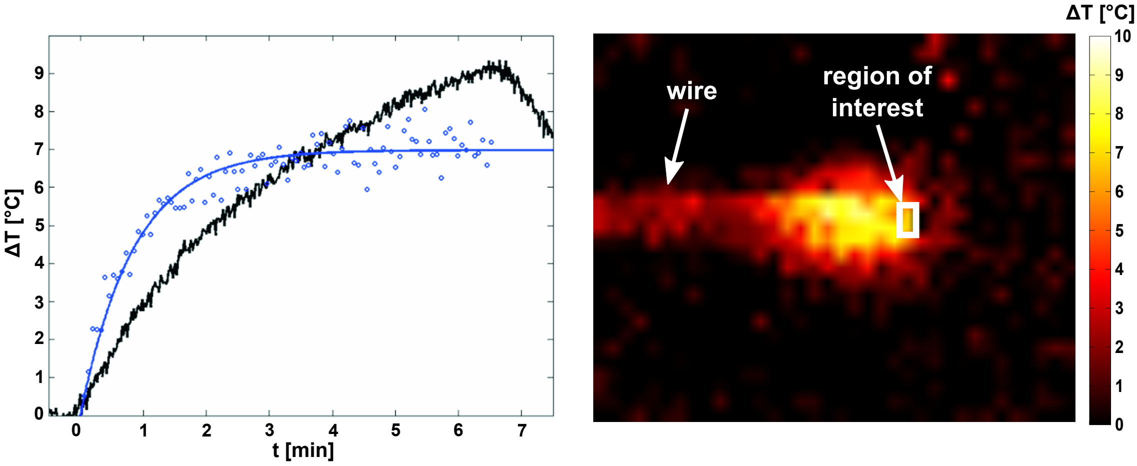

Figure 28: Temperature from the MRI temperature maps averaged over a two-pixel region of interest (in blue) in comparison to the readings from a fluoroptic probe (in black). The MRI measured temperature close to the wire tip is depicted on the right. The temperature was averaged over the two pixels in the region indicated by the white rectangle (approximately 4 mm beyond the tip of the wire).

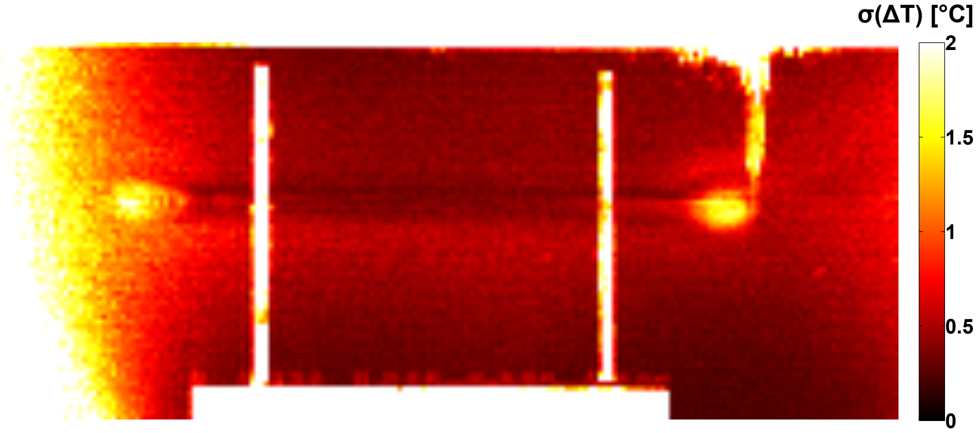

Figure 29: Map of mean standard deviation, calculated pixel-wise from the set of phase-contrast images and translated into temperature values using Equation 5.5.

Averaged MRI temperature values were fit to the following simple temperature model:

$$T(t) = T(0) + (T(\infty) - T(0)) \cdot \left(1 - \mathrm{e}^{-const \cdot t}\right) \tag{5.7}$$

where the baseline temperature was set to $T(0) = 0$, and the theoretical temperature in an infinitely large phantom after an infinite period of heating is given by $T(\infty)$. The temperature increase during the acquisition of the first phase-contrast image (reference) was estimated from this fit to be approximately 0.3°C (in the chosen region of interest). To adjust for the slight underestimation of the temperature increase due to the first acquisition serving as the reference image, this value was added to the MRI measured temperature.

The pixel-wise calculated standard deviation of the dynamic thermometry data set is shown in Figure 29. Areas of heating, as well as areas of low SNR (away from the receiver coil), can be identified by an increased standard deviation.

5.5 DISCUSSION

In this work, a new method that combines MRI heating and MRI thermometry for use in an MRI safety phantom study is presented. This combined method overcomes the disadvantage of a single point temperature measurement by a fluoroptic probe. The accuracy achieved in this study was sufficient for observing the temperature increase qualitatively. Further work is required in order to achieve a measurement precision comparable to fluoroptic probe thermometry.

Comparing the readings from the fluoroptic probe with the MRI measured temperature increase, it is perceivable that the MRI measurement reaches equilibrium earlier and shows a smaller maximum temperature increase. The former is easily explainable as the chosen region of interest is closer to the tip of the wire, so that inertia is expected to be smaller. However, there is no simple explanation for the smaller maximum value of the MRI measured temperature, as one would expect just the opposite. A possible explanation for this is RF shielding effects from the wire and eddy currents may have caused imaging artifacts and signal drop-outs, leading to systematic quantification errors in the immediate vicinity of the wire. As the intention of the shown experiments was to identify possible hot spots rather than to accurately quantify the temperature rise, this effect was not investigated in detail.

To estimate the error due to imaging noise in the modified MRI thermometry experiment, a map of the local mean standard deviation was calculated from the set of acquired phase-contrast images (Fig. 29). As expected, the mean SD is high in areas close to the wire tips where RF induced heating is expected, as the image phase changed over time. The location of the wire rack and the fluoroptic probe are also recognizable by an increased SD, since their material provides no measurable MRI signal. Outside these areas, the mean SD is much smaller and depends on the position and geometry of the receiver coil. The coil position was optimized for high SNR at one wire tip. As a consequence, the noise at the other tip was significantly higher. The mean SD caused by image noise in the chosen region of interest was extrapolated from the surrounding to be approximately 0.5°C. The associated error is too small to explain the discrepancy mentioned in the previous paragraph.

There are several more reasons why a quantitative comparison of the measurements from the probe and MRI is complex. The degree of agreement is highly dependent on the choice of the region of interest over which the measured temperature is averaged and on the positioning of the fluoroptic probe. In addition, it is impossible to obtain an MRI signal from the exact location of the fluoroptic probe at all. Therefore, an unflawed quantitative comparison is not viable. Additionally, it is possible that the probe may interfere with the local temperature increase as an additional artificial structure is put directly into the region in question. The value of the probe in temperature measurement is diminished if it changes the system to be observed significantly and unpredictably. Conversely, the effect of MRI thermometry on the implant heating can be easily quantified. It depends solely on the power contribution of the MRI thermometry module in the imaging sequence. Since this contribution is two orders of magnitude smaller than that of the heating pulse, it can be neglected. This highlights the main advantages and disadvantages of these two methods: MRI thermometry in the immediate vicinity of the wire (or other implants) is difficult to perform. However, even though a fluoroptic probe might in general be sensible to achieve very accurate measurement results, the temperature readings are highly dependent on its position. Even small displacements of the sensor can strongly influence the measured temperature values, especially in close vicinity to a hot spot [80]. Good reproducibility is therefore hard to achieve. The dependency of MRI thermometry on slice positioning is not so problematic at the current, relatively low, spatial resolution, as the temperature measured originates from a relatively large voxel and the region of interest can be chosen retrospectively (e.g., with the help of a high-resolution magnitude image). Furthermore, possible hot spots along large implants with a complex shape can be easily identified in one MRI temperature measurement. However, for this strategy to fully succeed and for a true global map of the temperature increase, it is necessary to extend the proposed method to three dimensions. A major hurdle is that this requires a significant increase in scan time, making it difficult to capture the dynamics of the temperature increase. An accelerated three-dimensional version of the proposed method is presented in the next chapter.

The method of using an RF pulse that does not influence the spin system for heating can be combined with any MRI temperature mapping technique, or more generally, with any MRI sequence. Changing the frequency of the heating pulse by a few tenths of a percent renders MRI thermometry possible without changing its heating capabilities. An improved version, which is less motion sensitive, such as one that is based on referenceless PRF shift thermometry [96] or using an appropriate T_1-based sequence [97], may have the potential for *in vivo* and noninvasive temperature monitoring of an MRI examination in an animal model.

A major drawback of the proposed technique is that accurate MRI thermometry on most standard implants is nearly impossible due to severe susceptibility artifacts. It is then necessary to use specially fabricated implants that are susceptibility-matched to the surrounding material (water and organic tissue). Fortunately, there are appropriate diamagnetic materials available, such as copper or carbon, if biocompatibility is essential. Konings et al. [98] have already stated that heating capabilities mainly depend on the conductivity of the material and not on the type of material itself. Therefore, replacing the material of the original implant by one that is susceptibility-matched to organic tissue would allow MRI thermometry without a major influence on its heating capabilities.

5.6 CONCLUSION

The method presented in this chapter can be used in safety testing environments for the noninvasive monitoring of the heating of implants during MRI examinations. A combination of MRI thermometry and local temperature probes may be very beneficial in MRI safety investigations. A sensible course of action may be to identify occurring hot spots in a preliminary experiment using MRI thermometry. The most prominent spots can then be further investigated in a second experiment using a suitable temperature probe.

6

IMPROVED MRI THERMOMETRY AND APPLICATION TO 3D

6.1 INTRODUCTION

A method that combines an MRI RF-heating protocol with an MRI thermometry sequence has been introduced in Chapter 5. It was possible to capture the temperature dynamics during MRI induced heating of a copper wire in a gel phantom. However, in order to obtain a more complete picture of the temperature increase around the wire, it is necessary to extend this method to three dimensions. Additionally, it is beneficial to increase the spatial resolution, in order to better resolve the temperature increase close to the wire. A major obstacle to the fulfillment of these goals is that both require additional phase-encoding steps, leading to a significant increase in scan time. Therefore, it was necessary to search for strategies to accelerate the three-dimensional MRI thermometry sequence. Another problem that had to be addressed, is the decrease in available signal-to-noise ratio due to the increase in spatial resolution (and due to the later mentioned reduction of TR). In order to alleviate this problem, a small water-proof loop coil was built, which was placed into the gel phantom, directly next to the wire, thereby increasing the available SNR considerably.

This work has been presented as an electronic poster at the 17th annual meeting of the *International Society for Magnetic Resonance Imaging (ISMRM)* in Honolulu, USA [99].

6.2 METHODS

Echo-Shifted MRI Heating/Thermometry Sequence

A straightforward approach to reduce the scan time of an MRI sequence is to simply reduce the repetition time. However, reducing TR usually requires a reduction of the echo time as well. Recalling from Equation 5.5 that the accuracy of the PRF shift thermometry method relies on relatively long echo times, this is obviously unfavorable. Fortunately, Moonen et al. developed a technique that allows for short repetition times while maintaining a long TE [100]. In an *echo shifted* sequence echo collection is delayed by one or more TRs, allowing for TE $>$ TR. This is achieved by applying a spoiler gradient directly after signal excitation and rephasing the magnetization not until a subsequent TR. Multiple modifications to this sequence have been proposed; an overview is given by Chung and Duerk [101].

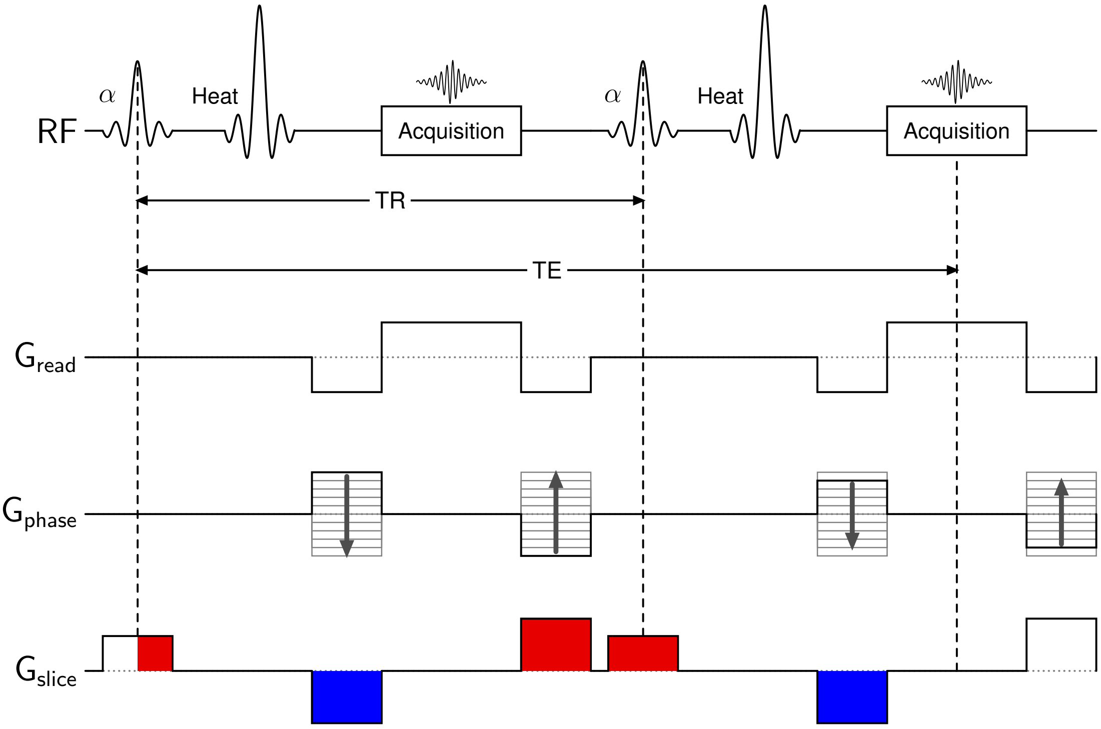

Figure 30: Diagram of the improved GRE heating/thermometry sequence (the 2D version is shown here for simplicity). Echo shifting is achieved by adequately dephasing the magnetization after excitation and rephasing it in the subsequent TR. The areas of gradients along the slice direction that are switched during the echo time are indicated in red and blue for gradients with positive and negative magnitude, respectively. The sum of these areas (and thus the corresponding gradient moment) is zero. Read and phase encoding gradients are fully balanced in every TR.

The improved echo shifted GRE heating/thermometry sequence is illustrated in Figure 30. As in the sequence introduced in the previous chapter, the off-resonant heating pulse is inserted between signal excitation and readout. In order to further reduce scan time, the sequence was programmed to allow for *elliptical scanning.* In an elliptical scanning acquisition, the phase-encoding steps in the "edges" of the 3D Cartesian k-space are skipped, resulting in a scan time reduction of 10-20 % (depending on the geometry of the chosen FoV).

General Setup

All experiments were performed on a Siemens Avanto 1.5 T imaging system. An insulated conductive copper wire with a length of 25 cm was placed on the left side of a 20 l gel phantom (5% Hydroxyethylcellulose (HEC) with a supplement of NaCl and CuSO4; conductivity = 0.47 S/m, T_1 = 280 ms). A custom-made loop coil (Ø=7cm) was placed near the left inside wall of the phantom (approx. 3 cm from the wire tip). The experimental setup is illustrated in Figure 31.

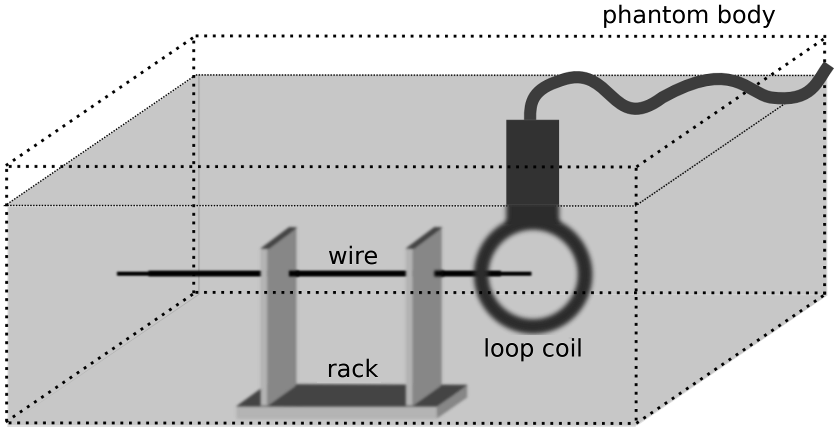

Figure 31: Experimental setup. In order to optimize SNR, a dedicated loop coil with a diameter of 7 cm was placed approximately 3 cm from the wire tip, directly into the gel.

Temperature mapping was performed using the described modified PRF (proton resonance frequency) method containing an off-resonant high power RF pulse, with its frequency set to 128 kHz below the resonance frequency of water. Averaged RF power of the sequence was set to 2.6 W/kg bodyweight (52 W) by adjusting the flip angle of the off-resonant pulse. A series of sixteen images was recorded consecutively. Other sequence parameters were as follows: $\alpha_{excitation} = 30°$ ($\alpha_{heating} = 111°$), TR/TE = 13.1/20 ms (echo shifting factor = 1), acq. bandwidth = 50 kHz, matrix size = 128 × 128 × 12 (with elliptical scanning), FoV = 110 × 110 × 10.9 mm^3, voxel size = 0.86 × 0.86 × 0.86 mm^3, acquisition time per frame = 15 s (total acquisition time = 4 min).

In contrast to the Siemens Vision imaging system that was used in the experiments from the last chapter, it was noticed that phase drifts were a serious problem for accurate MRI thermometry at the Avanto scanner. Phase drifts were determined by

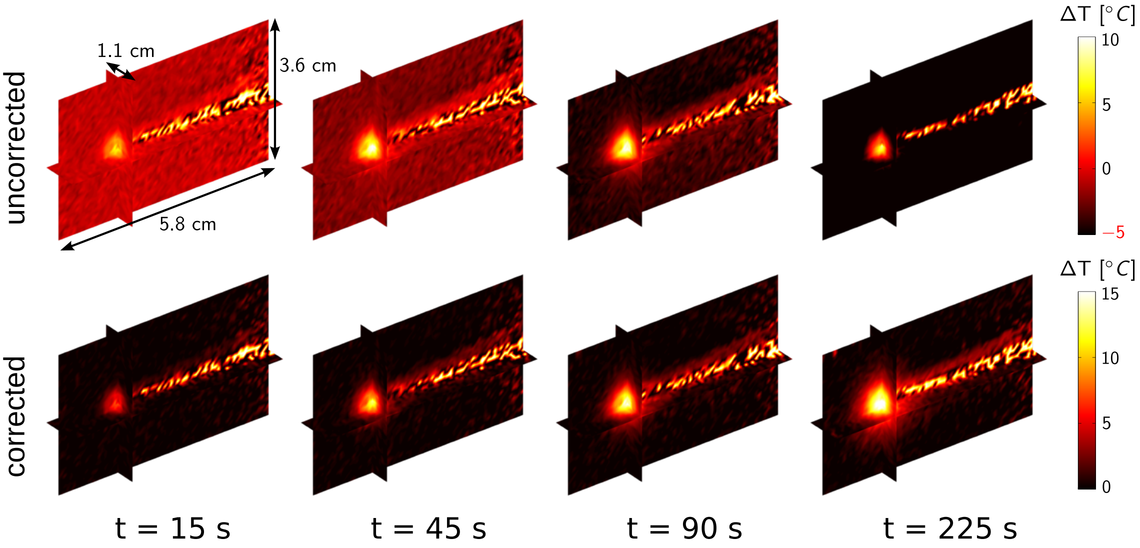

Figure 32: 3D depiction of the temperature increase close to the wire tip (interpolation), without (upper row) and with (lower row) correction for phase drifts. Without phase drift correction, the temperature in the periphery of the wire seems to decrease over time. Correcting the temperature maps with the help of a polynomial fit of the background phase leads to a visible improvement. Four out of sixteen reconstructed time frames are shown.

an 8th-order polynomial fit of the phase outside of the suspected heating area and the phase images were corrected accordingly. Temperature difference maps were calculated by subtracting each phase image from a reference image and utilizing the near-linear temperature-dependency of the resonance frequency for water protons. The generated heat at the wire tip was calculated from a sum over the difference temperatures in a region of interest around the wire tip with a total volume of 4.2 ml, by assuming that the heat capacity of the gel was comparable to that of water (specific heat capacity at constant pressure $c_p = 4.18$ kJ/(kg K) at room temperature) and neglecting volume expansion of the gel due to the temperature increase.

6.3 RESULTS

Four time frames of the reconstructed time-series, showing the heating of the wire tip, are displayed in Figure 32. In the upper row, the obtained temperature without phase-drift correction is shown. Phase drifts lead to an apparent cooling of the surrounding of the wire, especially visible in the later frames (negative ΔT in the periphery). Temperature maps in the lower row were corrected for phase drifts by subtracting a polynomic extrapolation of the change in background phase to the location of the assumed area of heating.

The calculated heat and heating power, obtained from a region of interest around the wire tip, are shown in Figure 33.

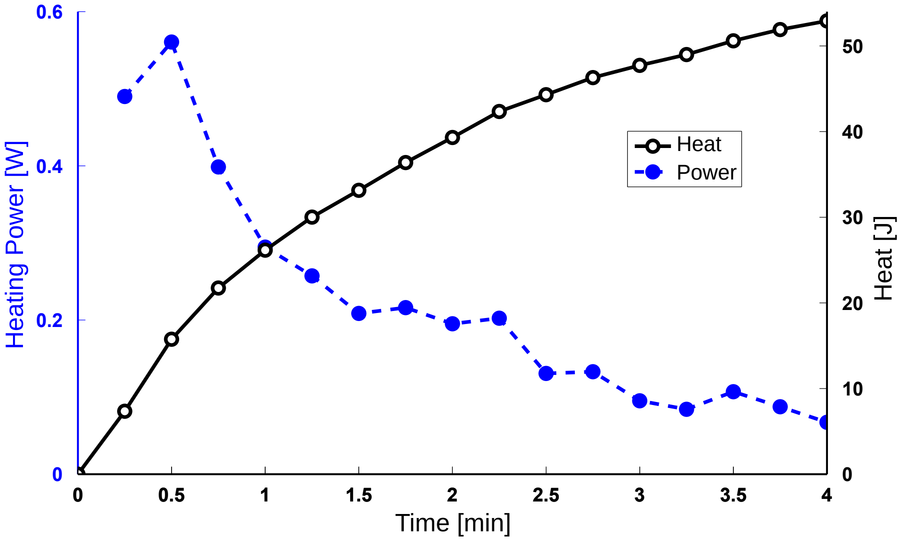

Figure 33: Heat and its first temporal derivative, i.e. heating power, at the wire tip, as calculated from a region of interest (with a volume of 4.2 ml around the wire tip). The observed heating power decreases over time, due to dissipation of heat outside of the chosen region of interest.

6.4 DISCUSSION AND CONCLUSION

This work shows the feasibility of three-dimensional MRI thermometry of the MRI-induced heating of a conductive wire, used as a model for a medical implant. By using a dedicated loop coil in combination with echo-shifting, it was possible to observe the temperature increase in high detail with a sub-millimeter resolution and an acquisition time of 15 s per volume. The presented results were obtained without the use of any data (or view) sharing between reconstructed time frames, which offers a potential for further imaging acceleration in case a higher frame rate, an increase in spatial resolution, or a better volume coverage is desired.

The experiment suffered from a severe phase drift between subsequently acquired images, making a correction of this effect absolutely necessary (compare Fig. 32). To this end, the phase drift was determined from a polynomic extrapolation of the background phase (outside of the suspected heating area) and subtracted from each individual phase image prior to temperature calculation. This correction method relies on the assumption that the temperature outside of the suspected area of heating is relatively constant during the experiment, which should hold true in good approximation for the relatively short scan time of the presented experiment. When this assumption is violated, temperature readings from multiple temperature probes may be used to correct the extrapolated background phase for temperature effects. It is important to note that the amount of observed phase drift depends on the scanner model and may also be influenced by the experimental setup. Thus, a phase drift correction may not always be required. For instance, the results shown in the previous chapter, acquired at a different scanner, suggest that a phase drift correction was not necessary (no significant change of the background phase was noticed during the experiment).

As illustrated in Figure 33, volume coverage of the temperature increase allows the calorimetric determination of the total heat absorption at the wire tip, as well as the calculation of the associated power. The presented results show that the measured heating power drops considerably during the course of the experiment. An explanation for this is that heat dissipates outside of the region of interest, which is especially restricted in the partition encoding direction; the presented results were acquired with a slice thickness of only 10.9 mm. Other potential "heat sinks" are regions close to the wire, where it is sometimes hard to determine the temperature due to RF shielding and/or susceptibility effects.

One of the main advantages over the two-dimensional approach, that was presented in Chapter 5, is the virtual elimination of problems associated with positioning errors. Therefore, this method presents a convenient way to determine local hot spots near implants quickly as a part of an MRI safety phantom study. As already suggested in the previous chapter, a sensible course of action may be to quickly identify hot spots with the proposed method and then further investigate the identified hot spots using more accurate, but local, fluoroptic thermometers or other temperature probes.

SUMMARY

Magnetic resonance imaging (MRI) is a medical imaging method that involves no ionizing radiation and can be used non-invasively. Another important - if not the most important - reason for the widespread and increasing use of MRI in clinical practice is its interesting and highly flexible image contrast, especially of biological tissue. The main disadvantages of MRI, compared to other widespread imaging modalities like computed tomography (CT), are long measurement times and the directly resulting high costs.

In the first part of this work, a new technique for accelerated MRI parameter mapping using a radial IR TrueFISP sequence is presented.

Standard clinical neurologic MRI examinations include the acquisition of several different image contrasts. Currently, a separate scan is required for each of these different contrasts, leading to long scan times. Besides possible consequent patient discomfort and higher costs due to longer scan times, there is also the potential of misregistration of clinically relevant anatomic information between different images due to inter-scan motion. One approach to avoid this is to directly quantify the underlying MR parameters that are responsible for image contrast. After successful quantification, synthetic images with any desired contrast can be retrospectively calculated from these parameter maps. Furthermore, there has been significant recent interest in a quantitative approach to MRI, as it provides a means of evaluating pathology using absolute tissue characteristics rather than a contrast-based approach.

A very fast method for the simultaneous quantification of proton density, the longitudinal relaxation time T_1, and the transverse relaxation time T_2, was developed several years ago here at the Department for Experimental Physics 5. The inversion recovery (IR) TrueFISP sequence consists of an inversion pulse, followed by a series of balanced steady-state free precession (bSSFP) images as the signal time course approaches the steady state. The relaxometry parameters can then be obtained from a mono-exponential fit to the series of images. However, for accurate quantification it has been necessary to acquire this time series in a segmented fashion, due to the rapid signal evolution towards the steady state. The need for such a segmented approach considerably increases the required acquisition time. Chapter 2 presents speed improvements to the original IR TrueFISP method that make segmentation unnecessary.

To this end, IR TrueFISP-based parameter mapping was combined with a radial trajectory with golden-ratio based profile and view-sharing. This profile order has the advantage of a near-optimal uniform k-space coverage for any number of projections. This makes the trajectory particularly well suited for view-sharing methods. View-

sharing accelerates imaging by sharing k-space data between adjacent time frames. In combination with a golden-ratio based profile order this makes it possible to generate a large number of images with different contrasts from a single-shot inversion-recovery experiment. To reconstruct a single time-frame, the center of k-space is taken from only a few acquired projections close to the chosen reconstruction time point, whereas high spatial frequencies are provided by including data from time points further away in order to avoid violation of the Nyquist sampling criterion. Compared to a conventional segmented IR TrueFISP experiment, a significant scan time reduction was achieved (approximately 6 s vs. 120 s for the segmented approach) at the expense of reduced signal-to-noise ratio and slightly increased blurring. Application of this method is demonstrated in relaxometry experiments of the human brain. Synthetic images with different contrasts are generated from the resulting parameter maps and compared to reference images. Slightly different image contrasts in these two sets of images hints to systematic quantification errors of the IR TrueFISP method. Furthermore, a retrospectively gated version of the proposed method is demonstrated for cardiac relaxometry.

Further investigation presented in Chapter 3 suggests two major sources of error for IR TrueFISP relaxometry. First, it was found that deviations of the excited slice profile from a perfect rectangular form leads to erroneous results since the IR TrueFISP method relies on the correct knowledge of the excitation flip angle which is only reached in the center of the slice. In order to correct for non-rectangular slice profiles, an effective flip angle is introduced, derived from a simulation of the IR TrueFISP experiment.

Another major source of error in protein-rich environments, like brain and muscle tissue, is magnetization transfer (MT). Magnetization transfer leads to a significant reduction of the bSSFP steady-state signal and the apparent relaxation time T_1^*. In an IR TrueFISP experiment, this results in a significant overestimation of T_1 and underestimation of T_2. This effect was investigated by varying the power of the RF excitation pulse and partially corrected by an extrapolation to a MT-free state.

In the second part of this work, a new MRI thermometry method is presented that can be used in MRI-safety investigations of medical implants, e.g. cardiac pacemakers and implantable cardioverter-defibrillators (ICDs). Currently, MRI examinations of patients with medical implants such as cardiac pacemakers, implantable cardioverter-defibrillators (ICD), or deep brain stimulators are contraindictated in most cases due to associated risks. This prevents a growing number of patients to benefit from advances in MRI diagnosis.

One of the major safety risks associated with MRI examinations of pacemaker and ICD patients is RF induced heating of the pacing electrodes that lead to the cardiac muscle. Severe heating close to the tips of the electrodes can cause burns in cardiac tissue that can result in a transient or permanent increase of the pacing thresholds. This heating strongly depends on the electrode's geometry, the exact location and orientation of the electrode in the patient and the imaging sequence used. Thus, the design of MRI-safe (or MRI-conditional) pacing electrodes requires elaborate testing. In a first step, many different electrode shapes, electrode positions and sequence parameters are tested in a gel phantom with its geometry and conductivity matched to a human body. The resulting temperature increase is typically observed using temperature probes (e.g. fluoroptic thermometers) that are placed at various positions in the gel phantom. However, thermometers only provide a locally restricted observation of the temperature increase. As a result, the observed temperature increase depends on the exact position of the probes.

An alternative to this local thermometry approach is to use MRI for the temperature measurement. In a prior study, a high-power MRI sequence (causing RF-induced heating) was followed by MRI thermometry. However, this approach has several drawbacks; temperature dynamics are almost impossible to monitor, and heat dissipation following the interruption of the heat-inducing MR imaging sequence leads to an underestimation of the observed temperature increase. Chapter 5 describes a new approach for MRI thermometry that allows MRI thermometry during RF heating caused by the MRI sequence itself. Specifically, a proton resonance frequency (PRF) shift MRI thermometry method was combined with an MR heating sequence. This method provides a map of temperature changes induced by the heating part of the sequence, with a, within limits, freely adjustable RF power. The method was validated in a gel phantom, with a copper wire serving as a simple model for a medical implant.

Chapter 6 describes further improvements to the proposed method. The first implementation of this combination of MRI induced heating and MRI thermometry was limited to a two dimensional acquisition. However, in order to obtain a more complete picture of the temperature increase, it is necessary to extend this method to three dimensions. Additionally, an increased spatial resolution is beneficial in order to better resolve the temperature increase. A major obstacle to the fulfillment of these goals is that both require additional phase-encoding steps, leading to a significant increase in scan time. This made it necessary to search for strategies to accelerate three-dimensional MRI thermometry. To this end, the concept of *echo shifting* was employed to allow for a reduction of the repetition time (TR) while maintaining a relatively long echo time (TE) which is required for accurate PRF shift thermometry. In an echo shifted sequence, echo collection is delayed by one or more TRs, resulting in an echo time that exceeds the repetition time. Furthermore, loss in signal-to-noise ratio (SNR) due to the increased spatial resolution was partially compensated by using a dedicated receiver coil that was directly placed into the gel. With these improvements to the original method it was possible to obtain a three-dimensional map of the temperature increase in the vicinity of a copper wire placed in a gel phantom at high spatial and temporal resolution (1 mm isotropic resolution with a scan time of 15 s per temperature map).

ZUSAMMENFASSUNG

Die Magnetresonanztomographie (MRT) zeichnet sich als medizinisches Bildgebungsverfahren dadurch aus, dass sie ohne ionisierende Strahlung auskommt und nicht-invasiv einsetzbar ist. Ein weiterer wichtiger - wenn nicht der wichtigste - Grund für die weite und wachsende Verbreitung der MRT in der klinischen Praxis ist ihr interessantes und hoch-flexibles Kontrastverhalten, und damit die gute Darstellbarkeit biologischen Gewebes. Die Hauptnachteile der MRT sind die, verglichen mit z.B. Computer-Tomographie (CT), langen Messzeiten und die damit direkt verbundenen hohen Untersuchungskosten.

Der erste Teil dieser Arbeit beschäftigt sich mit der beschleunigten MR-Parameterbestimmung mittels einer radialen IR TrueFISP Sequenz.

Bei neurologischen MRT Untersuchungen werden meist mehrere Bilder mit unterschiedlichen Kontrasten aufgenommen. Dies verlängert die benötigte Untersuchungszeit erheblich. Ein Ansatz um dies zu vermeiden, ist die direkte Quantifizierung der den Kontrastmechanismen zugrunde liegenden MR Parameter. Nach erfolgreicher Quantifizierung lassen sich nachträglich synthetische Bilder mit jedem beliebigen Kontrast erzeugen. Eine weitere Möglichkeit ist die quantitative Erfassung von Krankheitsverläufen direkt über die gemessenen MR Parameter.

Eine sehr schnelle Methode zur gleichzeitigen Quantifizierung der Protonendichte, der longitudinalen Relaxationszeit T_1, sowie der transversalen Relaxationszeit T_2, wurde vor einigen Jahren hier am Lehrstuhl entwickelt. Die *Inversion Recovery (IR) TrueFISP* Sequenz besteht aus einem Inversionspuls, gefolgt von einer Reihe von *balanced steady-state free precession* (bSSFP) Akquisitionen. Der Signalverlauf folgt dabei einer exponentiellen Relaxation in Richtung der bSSFP-Gleichgewichtsmagnetisierung. Aus einem drei-Parameter-Fit lassen sich dann (Wasserstoff-)Protonendichte, sowie die T_1- und T_2- Relaxationszeit bestimmen. Allerdings erfordert die herkömmliche IR TrueFISP Sequenz eine starke Segmentierung der Messung, was zu einer deutlichen Verlängerung der Messzeit führt. Ein Ziel dieser Arbeit war es daher, eine Methode zur Beschleunigung der IR TrueFISP Quantifizierung zu entwickeln und so eine Segmentierung der Messung überflüssig zu machen.

Zu diesem Zweck wurde eine radiale IR TrueFISP Sequenz mit radialer k-Raum Trajektorie entwickelt, bei der die Projektionsreihenfolge mit Hilfe des Goldenen Schnittes quasi-zufällig verteilt wird. Dies hat den Vorteil das der k-Raum mit jeder beliebigen Anzahl aufeinander folgender Projektionen nahezu symmetrisch abgetastet wird. Daher eignet sich diese Trajektorie besonders gut für sogenannte *view sharing* Verfahren, bei der sich aufeinander folgende Bilder einer Zeitserie k-Raum Daten teilen, um so eine Beschleunigung der Messung zu erreichen. Hierzu wurde

zunächst ein k-Raum Filter (basierend auf dem sogenannten KWIC-Filter) entwickelt, mit der sich die Zeitserie rekonstruieren lässt. Dazu wählt der Filter im Zentrum des k-Raums einige wenige Projektionen zur Bildrekonstruktion aus und kann so die Kontraständerung mit hoher zeitlicher Auflösung abbilden. Im äußeren k-Raum nimmt der Filter zunehmend Projektionen in die Rekonstruktion auf, um Einfaltungsartefakte aufgrund der Verletzung des Nyquist-Kriteriums zu vermeiden. Im Vergleich zum segmentierten, herkömmlichen IR TrueFISP Experiment konnte eine erhebliche Messzeitreduktion erreicht werden (ca. 6 s gegenüber 120 s für die segmentierte Messung), auf Kosten eines verringerten Signal-zu-Rausch Verhältnisses und leicht erhöhter Bildunschärfe (*blurring*). Die Anwendung des vorgestellten Verfahrens wird am menschlichen Gehirn demonstriert und aus den resultierenden Parameterkarten synthetisch erzeugte Bildkontraste werden mit Referenzmessungen verglichen. Außerdem wird eine erste Anwendung der Methode am menschlichen Herzen demonstriert.

Im Verlauf der Arbeit hat sich gezeigt, dass die genaue Quantifizierung mit IR TrueFISP, unabhängig vom verwendeten Bildrekonstruktionsverfahren, durch eine Reihe von Effekten beeinträchtigt wird, die einer genaueren Betrachtung bedürfen. Zunächst wurde festgestellt, das die Quantifizierung in einer 2D Messung von der Form des durch den Hochfrequenz-Puls angeregten Schichtprofils abhängt. Dieser Effekt lässt sich durch Einführung eines effektiven Flipwinkels korrigieren, der aus einer Simulation des Signalverlaufs bestimmt wird. Das in dieser Arbeit vorgestellte Korrekturverfahren wurde an einer Phantom- und einer *in vivo* Messung überprüft.

Besonders im Gehirn (aber auch in Muskelgewebe) tritt ein weiterer Effekt auf, der die korrekte Parameterquantifizierung erheblich erschwert: Der kürzlich gezeigte Einfluss von Magnetisierungstransfer (MT) auf die bSSFP Sequenz führt zu einer deutlichen Reduktion der bSSFP-Gleichgewichtsmagnetisierung sowie der apparenten Relaxationszeit T_1^*. Im IR TrueFISP Experiment führt dies zu einer erheblichen Überschätzung von T_1 und Unterschätzung von T_2. Dieser Effekt wurde durch Variation der HF-Pulsleistung und der Repetitionszeit untersucht und durch Extrapolation auf den Magnetisierungstransfer-freien Fall teilweise korrigiert.

Im zweiten Teil dieser Arbeit werden neuartige MR-Thermometrie Methoden vorgestellt, die sich besonders zur Untersuchung der MR-Sicherheit von medizinischen Implanten, insbesondere Herzschrittmachern und implantierbaren Kardioverter-Defibrillatoren (ICDs), eignen. Momentan sind in den allermeisten Fällen MRT Untersuchungen an Herzschrittmacher- und ICD-Patienten aufgrund der damit verbundenen Risiken kontraindiziert, so dass viele Patienten von den Vorteilen einer MR-Untersuchung nicht profitieren können.

Das am schwierigste in den Griff zu bekommende und damit größte Risiko ist die mögliche Schädigung des Myokards, hervorgerufen durch die von den geschalteten HF-Feldern induzierten Ströme in den Schrittmacherelektroden. Aufgrund des Leitfähigkeitsgefälles beim Übergang von der Elektrodenspitze in das Myokard bewirken diese Ströme eine stark konzentrierte Gewebeerhitzung, die zu Verbrennungen und damit zur einer transienten oder permanenten Reizschwellen-Erhöhung führen können. Die Gewebeerhitzung hängt stark von der Elektrodengeometrie, der genauen Lage und Orientierung der Elektrode im Patienten und im MRT sowie von den MR-Messparametern ab. Beim Design einer MR-sicheren Elektrode und sicherer Messprotokolle werden daher häufig viele verschiedene Elektroden, Elektrodenpositionen und Messparameter-Einstellungen in einem körperähnlichen (ähnliche Geometrie und Leitfähigkeit) Gel-Phantom untersucht. Die bei der jeweiligen Messung auftretenden Erhitzungen werden dabei meist mit Hilfe fiberoptischer Thermometer an verschiedenen Positionen im Gel gemessen. Allerdings hängt die gemessene Maximaltemperatur nun zusätzlich von der genauen Lage der Thermometer ab.

Eine Alternative ist die Aufnahme einer globalen Karte der Temperaturerhöhung mit Hilfe der MR-Thermometrie. Eine sehr beliebte MR-Thermometriemethode basiert auf der Temperaturabhängigkeit der chemischen Verschiebung (*proton resonance frequency (PRF) shift thermometry*), die für wässriges Gewebe und im Bereich der Raumtemperatur/Körpertemperatur nahezu linear verläuft. Durch Subtraktion der Bildphase nach MR-induzierter Erhitzung und einer Referenzphase, aufgenommen vor MR-induzierter Erwärmung, lässt sich so die relative Temperaturänderung bestimmen. Verwendet man dabei eine von der MR Thermometrie getrennte *HF-Heizsequenz* (Einstrahlung hoher HF Leistung zur HF induzierten Erwärmung), lässt sich der Temperaturanstieg allerdings nicht oder nur schlecht erfassen. Auch kann es durch den zeitlichen Versatz der Sequenzen zu einer Unterschätzung des erreichten Temperaturanstiegs kommen. In dieser Arbeit wurde daher eine Sequenz entwickelt, die MR-Thermometrie mit HF induziertem Heizen kombiniert. Hierzu wurde ein zusätzlicher off-resonanter HF Puls in die MR-Thermometriesequenz eingebaut, über den sich die eingestrahlte HF Leistung nahezu unabhängig von der Bildgebung steuern lässt. Diese Methode wurde an einem Kupferdraht im Gelphantom validiert und mit fiberoptisch gemessenen Temperaturanstiegen verglichen.

Die erste Vorstellung dieser Methode war zunächst lediglich auf die zweidimensionale Thermometrie beschränkt. Um diese Methode auch in drei Dimensionen sinnvoll anwenden zu können, war es notwendig, die Bildgebung deutlich zu beschleunigen. Ein Grund für die relativ lange Messzeit bei der PRF-Thermometrie sind lange Repetitionszeiten, die durch die für die Genauigkeit der Methode notwendigen langen Echozeiten bedingt sind. Um die Repetitionszeit (TR) bei unveränderter Echozeit reduzieren zu können, wurde sogenanntes *"Echo Shifting"* in die kombinierte MR-Thermometrie/-Heiz-Sequenz eingebaut. Beim Echo-Shifting wird das vom Anregungspuls erzeugte Signal erst in einem späteren TR ausgelesen. Dies führt zu dem ungewöhnlichen Fall das die Echozeit die Repetitionszeit übersteigt. Das Signal-zu-Rausch-Verhältnis (SNR) wurde durch den Einsatz einer dedizierten, im Gel platzierten, Messspule optimiert. Durch diese Verbesserungen gelang es eine dreidimensionale Temperaturkarte in der Umgebung des Kupferdrahtes im Gelphantom in hoher räumlicher und zeitlicher Auflösung aufzunehmen (1 mm isotrope Auflösung bei einer Messzeit von 15 s pro Temperaturkarte).

Part III

Appendix

BIBLIOGRAPHY

[1] Z.-P. Liang, P. Lauterbur, Principles of Magnetic Resonance Imaging: A Signal Processing Perspective, Wiley-IEEE Press, 1999.

[2] M. Bernstein, K. King, X. Zhou, Handbook of MRI Pulse Sequences, Academic Press, 2004.

[3] F. Bloch, Nuclear induction, Phys Rev 70 (7-8) (1946) 460–474.

[4] E. Purcell, H. Torrey, R. Pound, Resonance absorption by nuclear magnetic moments in a solid, Phys Rev 69 (1-2) (1946) 37–38.

[5] P. Zeeman, XXXII. On the influence of magnetism on the nature of the light emitted by a substance, Philosophical Magazine Series 5 43 (262) (1897) 226–239.

[6] H. Torrey, Bloch Equations with Diffusion Terms, Phys Rev 104 (3) (1956) 563–565.

[7] D. B. Twieg, The k-trajectory formulation of the NMR imaging process with applications in analysis and synthesis of imaging methods., Medical physics 10 (5) (1983) 610–21.

[8] A. Haase, J. Frahm, D. Matthaei, W. Hanicke, K. Merboldt, FLASH imaging. Rapid NMR imaging using low flip-angle pulses, J Magn Reson 67 (2) (1986) 258–266.

[9] A. P. Crawley, M. L. Wood, R. M. Henkelman, Elimination of transverse coherences in FLASH MRI., Magn Reson Med 8 (3) (1988) 248–60.

[10] Y. Zur, M. L. Wood, L. J. Neuringer, Spoiling of transverse magnetization in steady-state sequences., Magn Reson Med 21 (2) (1991) 251–63.

[11] J. H. Duyn, Steady state effects in fast gradient echo magnetic resonance imaging., Magn Reson Med 37 (4) (1997) 559–68.

[12] J. Hennig, Echoes – how to generate, recognize, use or avoid them in MR-imaging sequences (Part I), Concepts Magn Reson 3 (1991) 125–143.

[13] J. Hennig, Echoes – how to generate, recognize, use or avoid them in MR-imaging sequences (Part II), Concepts Magn Reson 3 (1991) 179–192.

[14] R. R. Ernst, G. Bodenhausen, A. Wokaun, Principles of nuclear magnetic resonance in one and two dimensions, Oxford : Clarendon Press, 1987, pp. 125–148.

[15] H. Carr, Steady-State Free Precession in Nuclear Magnetic Resonance, Phys Rev 112 (5) (1958) 1693–1701.

[16] A. Oppelt, R. Graumann, H. Barfuss, H. Fischer, W. Hartl, W. Shajor, FISP – a new fast MRI sequence, Electromedica 54 (1) (1986) 15–18.

[17] K. Scheffler, S. Lehnhardt, Principles and applications of balanced SSFP techniques., European radiology 13 (11) (2003) 2409–18.

[18] N. K. Bangerter, B. A. Hargreaves, S. S. Vasanawala, J. M. Pauly, G. E. Gold, D. G. Nishimura, Analysis of multiple-acquisition SSFP., Magn Reson Med 51 (5) (2004) 1038–47.

[19] Q. Xiang, H. M. N, Simple Cross-Solution for Banding Artifact Removal in bSSFP Imaging, in: Proc Soc ISMRM, 17th Annual Meeting, Honolulu, 2009.

[20] P. Lauterbur, Image formation by induced local interactions: examples employing nuclear magnetic resonance, Nature 242 (5394) (1973) 190–191.

[21] A. Kumar, D. Welti, R. Ernst, NMR Fourier zeugmatography, J Magn Reson 18 (1) (1975) 69–83.

[22] W. A. Edelstein, J. M. Hutchison, G. Johnson, T. Redpath, Spin warp NMR imaging and applications to human whole-body imaging., Phys Med Biol 25 (4) (1980) 751–6.

[23] V. Rasche, R. W. de Boer, D. Holz, R. Proksa, Continuous radial data acquisition for dynamic MRI., Magn Reson Med 34 (5) (1995) 754–761.

[24] S. Winkelmann, T. Schaeffter, T. Koehler, H. Eggers, O. Doessel, An optimal radial profile order based on the Golden Ratio for time-resolved MRI., IEEE Trans Med Imaging 26 (1) (2007) 68–76.

[25] C. A. Mistretta, O. Wieben, J. Velikina, W. Block, J. Perry, Y. Wu, K. Johnson, Highly constrained backprojection for time-resolved MRI., Magn Reson Med 55 (1) (2006) 30–40.

[26] M. Lustig, D. Donoho, J. M. Pauly, Sparse MRI: The application of compressed sensing for rapid MR imaging., Magn Reson Med 58 (6) (2007) 1182–95.

[27] N. Seiberlich, Advances in Non-Cartesian Parallel Magnetic Resonance Imaging Using the GRAPPA Operator, Ph.D. thesis, Universität Würzburg (2008).

[28] J. D. O'Sullivan, A fast sinc function gridding algorithm for fourier inversion in computer tomography., IEEE Trans Med Imaging 4 (4) (1985) 200–7.

[29] J. I. Jackson, C. H. Meyer, D. G. Nishimura, A. Macovski, Selection of a convolution function for Fourier inversion using gridding [computerised tomography application]., IEEE Trans Med Imaging 10 (3) (1991) 473–8.

[30] G. E. Sarty, R. Bennett, R. W. Cox, Direct reconstruction of non-Cartesian k-space data using a nonuniform fast Fourier transform., Magn Reson Med 45 (5) (2001) 908–15.

[31] J. A. Fessler, B. P. Sutton, Nonuniform fast fourier transforms using min-max interpolation, IEEE Trans Med Imaging 51 (2) (2003) 560–574.

[32] J. B. M. Warntjes, O. Dahlqvist, P. Lundberg, Novel method for rapid, simultaneous T1, T2*, and proton density quantification., Magn Reson Med 57 (3) (2007) 528–37.

[33] J. B. M. Warntjes, O. D. Leinhard, J. West, P. Lundberg, Rapid magnetic resonance quantification on the brain: Optimization for clinical usage., Magn Reson Med 60 (2) (2008) 320–9.

[34] C. L. Hoad, E. F. Cox, P. A. Gowland, Quantification of T(2) in the abdomen at 3.0 T using a T(2)-prepared balanced turbo field echo sequence., Magn Reson Med 63 (2) (2010) 356–64.

[35] T. C. Mamisch, S. Trattnig, S. Quirbach, S. Marlovits, L. M. White, G. H. Welsch, Quantitative T2 mapping of knee cartilage: differentiation of healthy control cartilage and cartilage repair tissue in the knee with unloading–initial results., Radiology 254 (3) (2010) 818–26.

[36] L. J. Anderson, S. Holden, B. Davis, E. Prescott, C. C. Charrier, N. H. Bunce, D. N. Firmin, B. Wonke, J. Porter, J. M. Walker, D. J. Pennell, Cardiovascular T2-star (T2*) magnetic resonance for the early diagnosis of myocardial iron overload., Eur Heart J 22 (23) (2001) 2171–9.

[37] J. Vymazal, A. Righini, R. A. Brooks, M. Canesi, C. Mariani, M. Leonardi, G. Pezzoli, T1 and T2 in the brain of healthy subjects, patients with Parkinson disease, and patients with multiple system atrophy: relation to iron content., Radiology 211 (2) (1999) 489–95.

[38] M. Brant-Zawadzki, H. Bartkowski, D. Ortendahl, L. Pitts, N. Hylton, M. Nishimura, L. Crooks, NMR in experimental cerebral edema: value of T1 and T2 calculations, Am J Neuroradiol 5 (2) (1984) 125.

[39] S. Riederer, S. Suddarth, S. Bobman, J. Lee, H. Wang, J. MacFall, Automated MR image synthesis: feasibility studies., Radiology 153 (1) (1984) 203.

[40] D. Ortendahl, N. Hylton, L. Kaufman, J. Watts, L. Crooks, C. Mills, D. Stark, Analytical tools for magnetic resonance imaging., Radiology 153 (2) (1984) 479.

[41] H. Iwaoka, T. Hirata, H. Matsuura, Optimal pulse sequences for magnetic resonance imaging-Computing accurate T1, T2, and proton density images, IEEE Trans Med Imaging 6 (4) (1987) 360–369.

[42] D. Feinberg, C. Mills, J. Posin, D. Ortendahl, Multiple spin-echo magnetic resonance imaging, Radiology 155 (2) (1985) 437–442.

[43] D. C. Look, D. R. Locker, Time Saving in Measurement of NMR and EPR Relaxation Times, Rev Sci Instrum 41 (2) (1970) 250–251.

[44] I. Kay, R. M. Henkelman, Practical implementation and optimization of one-shot T1 imaging., Magn Reson Med 22 (2) (1991) 414–24.

[45] E. K. Fram, R. J. Herfkens, G. Johnson, G. H. Glover, J. P. Karis, A. Shimakawa, T. G. Perkins, N. J. Pelc, Rapid calculation of T1 using variable flip angle gradient refocused imaging, Magn Reson Imaging 5 (3) (1987) 201–208.

[46] K. a. Christensen, D. M. Grant, E. M. Schulman, C. Walling, Optimal determination of relaxation times of fourier transform nuclear magnetic resonance. Determination of spin-lattice relaxation times in chemically polarized species, J Phys Chem 78 (19) (1974) 1971–1977.

[47] H. Carr, E. Purcell, Effects of Diffusion on Free Precession in Nuclear Magnetic Resonance Experiments, Phys Rev 94 (3) (1954) 630–638.

[48] S. Meiboom, D. Gill, Modified Spin-Echo Method for Measuring Nuclear Relaxation Times, Rev Sci Instrum 29 (8) (1958) 688.

[49] S. C. L. Deoni, B. K. Rutt, T. M. Peters, Rapid combined T1 and T2 mapping using gradient recalled acquisition in the steady state., Magn Reson Med 49 (3) (2003) 515–26.

[50] P. Schmitt, M. A. Griswold, P. M. Jakob, M. Kotas, V. Gulani, M. Flentje, A. Haase, Inversion recovery TrueFISP: quantification of T1, T2, and spin density., Magn Reson Med 51 (4) (2004) 661–7.

[51] K. Scheffler, On the transient phase of balanced SSFP sequences., Magn Reson Med 49 (4) (2003) 781–3.

[52] V. Gulani, P. Schmitt, M. A. Griswold, A. G. Webb, P. M. Jakob, Towards a single-sequence neurologic magnetic resonance imaging examination: multiple-contrast images from an IR TrueFISP experiment., Investigative radiology 39 (12) (2004) 767–74.

[53] J. Hennig, O. Speck, K. Scheffler, Optimization of signal behavior in the transition to driven equilibrium in steady-state free precession sequences., Magn Reson Med 48 (5) (2002) 801–9.

[54] D. C. Peters, J. A. Derbyshire, E. R. McVeigh, Centering the projection reconstruction trajectory: reducing gradient delay errors., Magn Reson Med 50 (1) (2003) 1–6.

[55] F. Trautwein, Analyse und Eliminierung von system- und messprozessbedingten Bildartefakten in der radialen Magnetresonanztomographie, Master thesis, Fachhochschule Furtwangen (2005).

[56] H. K. Song, L. Dougherty, k-space weighted image contrast (KWIC) for contrast manipulation in projection reconstruction MRI., Magn Reson Med 44 (6) (2000) 825–32.

[57] J. V. Hajnal, B. D. Coene, P. D. Lewis, C. J. Baudouin, F. M. Cowan, J. M. Pennock, I. R. Young, G. M. Bydder, High Signal Regions in Normal White Matter Shown by Heavily T2-Weighted CSF Nulled IR Sequences, J Comput Assist Tomogr 16 (4).

[58] V. Matschl, K. Jahns, A. Reykowsi, Novel Spine and Body Coil Designs Using Matrix Clusters And Mode Combiners, in: Proc Intl Soc Magn Reson Med, 11th Annual Meeting; Honolulu, USA, 2004, p. 1586.

[59] D. O. Walsh, a. F. Gmitro, M. W. Marcellin, Adaptive reconstruction of phased array MR imagery., Magn Reson Med 43 (5) (2000) 682–90.

[60] A. C. Larson, R. D. White, G. Laub, E. R. McVeigh, D. Li, O. P. Simonetti, Self-gated cardiac cine MRI., Magn Reson Med 51 (1) (2004) 93–102.

[61] A. C. S. Brau, J. H. Brittain, Generalized self-navigated motion detection technique: Preliminary investigation in abdominal imaging., Magnetic resonance in medicine : official journal of the Society of Magnetic Resonance in Medicine / Society of Magnetic Resonance in Medicine 55 (2) (2006) 263–70.

[62] O. Bieri, K. Scheffler, On the origin of apparent low tissue signals in balanced SSFP., Magn Reson Med 56 (5) (2006) 1067–74.

[63] O. Bieri, K. Scheffler, Optimized balanced steady-state free precession magnetization transfer imaging., Magn Reson Med 58 (3) (2007) 511–8.

[64] S. D. Wolff, R. S. Balaban, Magnetization transfer contrast (MTC) and tissue water proton relaxation in vivo., Magnetic resonance in medicine : official journal of the Society of Magnetic Resonance in Medicine / Society of Magnetic Resonance in Medicine 10 (1) (1989) 135–44.

[65] R. M. Henkelman, G. J. Stanisz, S. J. Graham, Magnetization transfer in MRI: a review., NMR in biomedicine 14 (2) (2001) 57–64.

[66] M. Gloor, K. Scheffler, O. Bieri, Quantitative magnetization transfer imaging using balanced SSFP., Magn Reson Med 60 (3) (2008) 691–700.

[67] O. Bieri, K. Scheffler, SSFP signal with finite RF pulses., Magn Reson Med 62 (5) (2009) 1232–41.

[68] R. K. Breger, A. A. Rimm, M. E. Fischer, R. A. Papke, V. M. Haughton, T1 and T2 measurements on a 1.5-T commercial MR imager., Radiology 171 (1) (1989) 273–6.

[69] E. Henderson, G. McKinnon, T. Y. Lee, B. K. Rutt, A fast 3D look-locker method for volumetric T1 mapping., Magn Reson Med 17 (8) (1999) 1163–71.

[70] R. Srinivasan, R. Henry, D. Pelletier, S. Nelson, Standardized, reproducible, high resolution global measurements of T1 relaxation metrics in cases of multiple sclerosis., Am J Neuroradiol 24 (1) (2003) 58–67.

[71] R. G. Steen, S. A. Gronemeyer, P. B. Kingsley, W. E. Reddick, J. S. Langston, J. S. Taylor, Precise and accurate measurement of proton T1 in human brain in vivo: validation and preliminary clinical application., J Magn Reson B 4 (5) (1994) 681–91.

[72] K. P. Whittall, A. L. MacKay, D. A. Graeb, R. A. Nugent, D. K. Li, D. W. Paty, In vivo measurement of T2 distributions and water contents in normal human brain., Magn Reson Med 37 (1) (1997) 34–43.

[73] C. S. Poon, R. M. Henkelman, Practical T2 quantitation for clinical applications., J Magn Reson Imaging 2 (5) (1992) 541–53.

[74] O. Bieri, An analytical description of balanced steady-state free precession with finite radio-frequency excitation., Magn Reson Med 65 (2) (2011) 422–31.

[75] O. Bieri, Superbalanced steady state free precession, Magnetic Resonance in Medicine (in press).

[76] T. S. Ibrahim, R. Lee, B. a. Baertlein, P. M. Robitaille, B1 field homogeneity and SAR calculations for the birdcage coil., Phys Med Biol 46 (2) (2001) 609–19.

[77] C. Ganter, Off-resonance effects in the transient response of SSFP sequences., Magn Reson Med 52 (2) (2004) 368–75.

[78] C. Armenean, E. Perrin, M. Armenean, O. Beuf, F. Pilleul, H. Saint-Jalmes, RF-induced temperature elevation along metallic wires in clinical magnetic resonance imaging: influence of diameter and length., Magn Reson Med 52 (5) (2004) 1200–1206.

[79] R. Luechinger, V. A. Zeijlemaker, E. M. Pedersen, P. Mortensen, E. Falk, F. Duru, R. Candinas, P. Boesiger, In vivo heating of pacemaker leads during magnetic resonance imaging., Eur Heart J 26 (4) (2005) 376–377.

[80] E. Mattei, M. Triventi, G. Calcagnini, F. Censi, W. Kainz, H. I. Bassen, P. Bartolini, Temperature and SAR measurement errors in the evaluation of metallic linear structures heating during MRI using fluoroptic probes., Physics in medicine and biology 52 (6) (2007) 1633–46.

[81] D. Levine, C. Zuo, C. B. Faro, Q. Chen, Potential heating effect in the gravid uterus during MR HASTE imaging., J Magn Reson Imaging 13 (6) (2001) 856–61.

[82] B. Qiu, A.-M. El-Sharkawy, V. Paliwal, P. Karmarkar, F. Gao, E. Atalar, X. Yang, Simultaneous radiofrequency (RF) heating and magnetic resonance (MR) thermal mapping using an intravascular MR imaging/RF heating system., Magn Reson Med 54 (1) (2005) 226–30.

[83] Y. Ishihara, A. Calderon, H. Watanabe, K. Okamoto, Y. Suzuki, K. Kuroda, A precise and fast temperature mapping using water proton chemical shift., Magn Reson Med 34 (6) (1995) 814–23.

[84] P. Ehses, F. Fidler, P. Nordbeck, E. D. Pracht, M. Warmuth, P. M. Jakob, W. R. Bauer, MRI thermometry: Fast mapping of RF-induced heating along conductive wires., Magn Reson Med 60 (2) (2008) 457–61.

[85] L. Zaremba, Guidance for industry and FDA staff: Criteria for significant risk investigations of magnetic resonance diagnostic devices, US Department of Health and Human Services, Food and Drug Administration 14.

[86] E. Kanal, An overview of electromagnetic safety considerations associated with magnetic resonance imaging., Ann N Y Acad Sci 649 (1992) 204–24.

[87] R. Buchli, P. Boesiger, D. Meier, Heating effects of metallic implants by MRI examinations., Magn Reson Med 7 (3) (1988) 255–61.

[88] B. Quesson, J. A. de Zwart, C. T. W. Moonen, Magnetic resonance temperature imaging for guidance of thermotherapy., J Magn Reson Imaging 12 (4) (2000) 525–533.

[89] V. Rieke, K. Butts Pauly, MR thermometry., J Magn Reson Imaging 27 (2) (2008) 376–90.

[90] R. M. Goldstein, H. A. Zebker, C. L. Werner, Satellite radar interferometry: Two-dimensional phase unwrapping, Radio Sci 23 (4) (1988) 713–720.

[91] D. C. Ghiglia, M. D. Pritt, Two-dimensional phase unwrapping: theory, algorithms, and software., John Wiley & Sons, New York, 1998.

[92] W. Kainz, Draft: SAR intercomparison protocol for 1.5 T MR systems., U.S. Food and Drug Administration, Center for Devices and Radiological Health, Office of Science and Engineering Laboratories & Office of Device Evaluation.

[93] J. Schenck, Others, The role of magnetic susceptibility in magnetic resonance imaging: MRI magnetic compatibility of the first and second kinds, Med Phys 23 (1996) 815–850.

[94] ASTM Standard F2182 - 11: Standard Test Method for Measurement of Radio Frequency Induced Heating Near Passive Implants During Magnetic Resonance Imaging (2011). `http://www.astm.org/Standards/F2182.htm`

[95] J. MacFall, D. Prescott, H. Charles, T. Samulski, H MRI phase thermometry in vivo in canine brain, muscle, and tumor tissue, Medical Physics 23 (1996) 1775.

[96] V. Rieke, K. K. Vigen, G. Sommer, B. L. Daniel, J. M. Pauly, K. Butts, Referenceless PRF shift thermometry., Magn Reson Med 51 (6) (2004) 1223–31.

[97] D. Gensler, F. Fidler, M. Warmuth, T. Reiter, O. Ritter, M. E. Ladd, H. H. Quick, P. M. Jakob, W. R. Bauer, Fast T1-Thermometry of the RF Induced Heating of Conductive Wires, Proc Intl Soc Magn Reson Med, 19th Annual Meeting; Montréal, Canada 60 (2) (2011) 3766–3766.

[98] M. K. Konings, L. W. Bartels, H. F. Smits, C. J. Bakker, Heating around intravascular guidewires by resonating RF waves., J Magn Reson Imaging 12 (1) (2000) 79–85.

[99] P. Ehses, M. A. Lopez, M. T. Friedrich, F. Fidler, P. Nordbeck, M. Warmuth, W. R. Bauer, 3D MRI thermometry of MR-induced heating of a wire and determination of total generated heat, in: Proc Intl Soc Mag Reson Med 17, 2009, p. 4795.

[100] C. T. W. Moonen, G. Liu, P. Van Gelderen, G. Sobering, A fast gradient-recalled MRI technique with increased sensitivity to dynamic susceptibility effects, Magn Reson Med 26 (1) (1992) 184–189.

[101] Y. C. Chung, J. L. Duerk, Signal formation in echo-shifted sequences., Magn Reson Med 42 (5) (1999) 864–75.

LIST OF FIGURES

Figure 1 A representation of the relationships between the image space and k-space domain. The field of view (FoV) of the image is proportional to the inverse of the distance between neighboring k-space points. If the chosen FoV becomes smaller than the object being imaged, i.e. the distance between k-space points becomes too high, aliasing occurs. The achievable resolution is proportional to the inverse of the maximum k-space point sampled. 16

Figure 2 Top: Basic Cartesian 2D GRE sequence. Periods of phase-encoding and read dephasing are indicated by (1), the acquisition window by (2). Bottom: The spatial encoding scheme can also be understood by looking at the k-space trajectory: The phase-encoding and read dephasing gradients move the k-space vector to the beginning of a k-space line (1). During signal acquisition, the readout gradient moves the trajectory in k_x direction to the end of the current k-space line (2). 19

Figure 3 2D Cartesian fully balanced steady-state free precession (bSSFP) sequence. Gradients on all axes are fully balanced in every TR. 20

Figure 4 Left: Frequency response of the bSSFP sequence (for three different flip angles). The frequency response is periodic with a periodicity of 2π. Right: Banding artifacts in cardiac bSSFP imaging (bandings indicated by white arrows). 22

Figure 5 Top: 2D Radial version of the bSSFP sequence (compare to Fig. 3). Bottom: Illustration of radial k-space sampling with 16 equiangular spaced projections and linear view-ordering. 24

Figure 6 Signal time course of an IR TrueFISP experiment. Following signal inversion, the signal approaches the bSSFP steady state exponentially during a continuous run of bSSFP acquisitions. 31

Figure 7 Simulation of the radial bSSFP sequence implemented in IDEA. In this example, signal inversion and a linear increasing flip angle preparation module are followed by a radial bSSFP acquisition with conventional linear ordering of projection angles. 33

Figure 8 Effect of gradient delays (denoted by τ_x, τ_y) on the timing of a radial bSSFP sequence (for better visualization, gradient delays are highly exaggerated compared to the duration of the acquisition window). The shaded areas correspond to the extra gradient moments in x- and y-direction that have accumulated at the intended echo position, which is equivalent to a shift in k-space. Resulting trajectory errors are illustrated in Figure 9. 34

Figure 9 Effect of gradient delays on a 2D radial trajectory with 16 projections (only the center part of k-space is shown). Left: Equal gradient delays in x and y direction lead to a shift between the time of the gradient-echo for each projection (indicated by circles) and the intended echo time in the center of k-space (indicated by a square). Right: Anisotropic gradient delays additionally shift the projections with respect to each other. As a result, the projections do not share a common intersection point anymore. This is the more realistic situation. 35

Figure 10 Illustration of data selection by temporal k-space filtering. Top: Following inversion, signal evolution towards the bSSFP steady state is observed using a radial readout with golden-ratio based profile order. In a first step towards reconstruction of a single time-frame, a number of projections is selected that sufficiently covers the entire k-space. Bottom: From these projections and depending on the k-space position in read direction (k_x), the filter selects only as many projections close to the chosen reconstruction time point as necessary according to Nyquist (selected projections are indicated in black). Thus, only a few projections need to be selected close to the center of k-space while more and more projections need to be included further out in k-space. This leads to the characteristic hourglass/tornado shape of the filter. Initially, following the inversion pulse, this filter is highly asymmetric, since there is no data from prior time points. Later, the filter becomes more and more symmetric. 38

Figure 11 Illustration of golden-ratio based radial profile order and filtering in k-space. Subsequent projections are spaced by an angle increment of π divided by the golden mean (five successive projections are color-coded from red to yellow). For k-space filtering, projections are grouped into rings. The central ring consists of eight projections that were acquired closest to the target time point. In order to fulfill the Nyquist criterion, the included number of projections jumps to the next Fibonacci number further out in k-space, thus forming the next ring. This results in a relatively uniform k-space sampling density. This figure also illustrates that in each ring, the angular distance between the next neighbors of a projection alternates between two possible values (denoted by $\Delta\phi_1$ and $\Delta\phi_2$ in red and blue, respectively). Thus, a density compensation function based on the Ram-Lak filter has to be corrected for this angular anisotropy. 39

Figure 12 Five representative time frames from the IR TrueFISP experiment with inversion times (TI) ranging from 48 ms to 6 s. 42

Figure 13 Proton density, T_1 and T_2 maps, determined from a fit to the reconstructed time series. 42

Figure 14 Artificially generated images compared to standard clinical MRI reference images. Although general contrast information is closely reproduced, there are some differences evident: Ventricles and venous sinuses appear brighter than in the standard images and gray/white matter contrast is a little different, especially apparent in the FLAIR and T_2-weighted images. 43

Figure 15 a) Unfiltered DC signal for all five coil channels. High-frequency signal components due to noise and trajectory errors are removed from this signal using low-pass filtering. The resulting filtered DC signal is shown in b). A biexponential version of Equation 3.1 is then fit to this time series, as shown by dotted lines in b). This fitted time course was then subtracted from the DC signal in order to remove the relaxation dynamics of the IR TrueFISP experiment. The remaining DC signal nicely shows signal fluctuations due to cardiac motion, as demonstrated in c) for one of the coil channels (#4). This cardiac self-gating DC signal shows a high correlation with the recorded ECG signal (d). The gating window was manually determined from this self-gating signal, as indicated by gray-shaded boxes in c) and d). Only projections that were acquired in the corresponding time intervals were included in the reconstruction of the time series (shown in Figure 16). 44

Figure 16 Representative time frames from the cardiac IR TrueFISP experiment. 46

Figure 17 Proton density, T_1 and T_2 maps, as obtained from a fit to the reconstructed time series of the cardiac IR TrueFISP experiment. 46

Figure 18 Illustration of synthetic imaging in MRI. Based on a full set of relaxometry data (proton density, T_1 and T_2), the user can retrospectively adjust image contrast by selecting repetition time (TR), echo time (TE) and inversion time (TI) that are then used for synthetic image generation. 47

Figure 19 Flow chart of the proposed corrections for IR TrueFISP quantification: After running three separate IR TrueFISP experiments with varying RF pulse durations and after performing fits to Equation 3.1, the steady state signal is extrapolated to the MT-free state. Using this extrapolation together with T_1^* from the scan that was least affected by MT, and S_0 from one of the scans (using S_0 from the scan with shortest TR reduces blurring), first estimates of T_1 and T_2 are obtained, that are iteratively corrected for slice profile imperfections using a lookup table in the following. Convergence is achieved when the mean change of the effective flip angle is below 1 % between iterations. 54

Figure 20 a) Simulated signal evolution for an IR TrueFISP experiment depending on slice position (T_1/T_2 = 600/60 [ms], sinc pulse with TBW = 2; slice thickness = 50 mm; nominal flip angle = 60°), b) sum over slice of simulated signal and exponential fit through simulated data points. 56

Figure 21 Phantom results: T_1 and T_2 values from all phantoms with and without correction for imperfect slice excitation over the corresponding reference values (for a better distinction of short T_2 species, see Table 2). Magnetization transfer plays no role in the phantom experiments, so there was no need for a MT correction. 56

Figure 22 a) Effective flip angle lookup table determined from the fit for different T_1, T_2 combinations. b) Iteratively determined map of effective flip angles for one of the volunteers (same scaling as b). 57

Figure 23 From top to bottom: steady state signal, T_1, and T_2 maps, as obtained from a 3-parameter fit, for three experiments with different rf-scaling factors β and thus MT levels (first three columns), as well as extrapolated to $\beta \rightarrow \infty$ (far right column). Short pulses (small β) lead to a severe attenuation of the steady state signal due to an increased MT effect, which translates into an overestimation of T_1, and underestimation of T_2. Quantification of M_0 is not affected by MT (and is thus not shown in this figure). 58

Figure 24 Parameter maps, corrected for slice profile and MT, for two of the normal volunteers. Regions of interest used for further analysis (see Table 3) are shown in the proton density maps in red; 1: CSF; 2: white matter; 3: gray matter. 59

Figure 25 Diagram of GRE heating sequence. To allow long echo times while keeping TR as short as possible, the heating pulse was included inside TE, directly after slice refocusing of the excitation pulse. Shaded areas represent spoiling moments in read and slice direction, respectively. 72

Figure 26 Left: Illustration and Right: Photo of the experimental setup. A copper wire was placed 40 mm from the left wall of a 20 l gel phantom. As a reference for temperature mapping, a fluoroptic temperature probe was positioned 5 mm in front of one of the wire tips. 73

Figure 27 Overlay of a scout image and the PRF shift temperature map after the 7-min heating period. Both images were interpolated to a matrix size of 384 x 1024 (two-fold interpolation of the scout and four-fold interpolation of the temperature map). Only temperature differences larger than 2°C and in an area 20 mm adjacent to the wire are shown. Pronounced hot spots are visible at both tips of the wire. 75

Figure 28 Temperature from the MRI temperature maps averaged over a two-pixel region of interest (in blue) in comparison to the readings from a fluoroptic probe (in black). The MRI measured temperature close to the wire tip is depicted on the right. The temperature was averaged over the two pixels in the region indicated by the white rectangle (approximately 4 mm beyond the tip of the wire). 75

Figure 29 Map of mean standard deviation, calculated pixel-wise from the set of phase-contrast images and translated into temperature values using Equation 5.5. 76

Figure 30 Diagram of the improved GRE heating/thermometry sequence (the 2D version is shown here for simplicity). Echo shifting is achieved by adequately dephasing the magnetization after excitation and rephasing it in the subsequent TR. The areas of gradients along the slice direction that are switched during the echo time are indicated in red and blue for gradients with positive and negative magnitude, respectively. The sum of these areas (and thus the corresponding gradient moment) is zero. Read and phase encoding gradients are fully balanced in every TR. 80
Figure 31 Experimental setup. In order to optimize SNR, a dedicated loop coil with a diameter of 7 cm was placed approximately 3 cm from the wire tip, directly into the gel. 81
Figure 32 3D depiction of the temperature increase close to the wire tip (interpolation), without (upper row) and with (lower row) correction for phase drifts. Without phase drift correction, the temperature in the periphery of the wire seems to decrease over time. Correcting the temperature maps with the help of a polynomial fit of the background phase leads to a visible improvement. Four out of sixteen reconstructed time frames are shown. 82
Figure 33 Heat and its first temporal derivative, i.e. heating power, at the wire tip, as calculated from a region of interest (with a volume of 4.2 ml around the wire tip). The observed heating power decreases over time, due to dissipation of heat outside of the chosen region of interest. 83

LIST OF TABLES

Table 1 Examples of measured gradient delays for three MRI systems at two locations. Note that these delays are only valid for a specific dwell time and for imaging sequences with similar timing. 36

Table 2 Phantom data: T_1 and T_2 for all seven phantom bottles, with and without correction for imperfect slice excitation, and corresponding reference values. (Mean ± SD). 57

Table 3 Volunteer data: Parameters obtained from ROIs positioned in different parts of the brain (Mean ± SD over six volunteers / 5 volunteers in case of CSF), corrected for slice profile inaccuracies and magnetization transfer. References for previously reported T_1 values are: [37, 49, 68, 69, 70, 71, 72]; and for T_2: [37, 49, 72, 73]. 60

Table 4 List of FDA recommended SAR Limits during an MRI scan [85]. 68

Table 5 Comparison of different MRI temperature mapping techniques [88]. Note that the PRF shift method, as well as spectroscopic MRI thermometry rely both on the temperature dependence of the chemical shift of water. 70

PUBLICATIONS

PAPERS

- *Ehses P,* Seiberlich N, Ma D, Breuer FA, Jakob PM, Griswold MA, Gulani V. IR TrueFISP with a Golden-Ratio based Radial Readout: Fast Quantification of T1, T2, and Proton Density. Submitted to Magn Reson Med.
- Seiberlich N, Lee G, *Ehses P*, Duerk JL, Gilkeson R, Griswold MA. Improved Temporal Resolution in Cardiac Imaging Using Through-Time Spiral GRAPPA. Magn Reson Med. 2011 Dec;66(6):1682-8.
- Seiberlich N, *Ehses P*, Duerk JL, Gilkeson R, Griswold MA. Improved Radial GRAPPA Calibration for Real-Time Free-Breathing Cardiac Imaging. Magn Reson Med. 2011 Feb;65:492–505.
- Lopez MA, *Ehses P*, Breuer FA, Ponce IP, Gareis D, Jakob PM. A Four-Channel Hole-Slotted Phased Array at 7 Tesla. Concepts Magn. Reson. 2010 Okt; 37B(4):226–236.
- Seiberlich N, Breuer FA, *Ehses P*, Moriguchi H, Blaimer M, Jakob PM, Griswold MA. Using the GRAPPA operator and the generalized sampling theorem to reconstruct undersampled non-Cartesian data. Magn Reson Med. 2009 Mar;61(3):705-15.
- Nordbeck P, Weiss I, *Ehses P*, Ritter O, Warmuth M, Fidler F, Herold V, Jakob PM, Ladd ME, Quick HH, Bauer WR. Measuring RF-induced currents inside implants: Impact of device configuration on MRI safety of cardiac pacemaker leads. Magn Reson Med. 2009 Mar;61(3):570-8.
- Nordbeck P, Fidler F, Weiss I, Warmuth M, Friedrich MT, *Ehses P*, Geistert W, Ritter O, Jakob PM, Ladd ME, Quick HH, Bauer WR. Spatial distribution of RF-induced E-fields and implant heating in MRI. Magn Reson Med. 2008 Aug;60(2):312-9.
- *Ehses P*, Fidler F, Nordbeck P, Pracht ED, Warmuth M, Jakob PM, Bauer WR. MRI thermometry: Fast mapping of RF-induced heating along conductive wires. Magn Reson Med. 2008 Aug;60(2):457-61.
- Ceymann A, Horstmann M, *Ehses P*, Schweimer K, Paschke AK, Steinert M, Faber C. Solution structure of the Legionella pneumophila Mip-rapamycin complex. BMC Struct Biol. 2008 Mar 17;8:17.

- Horstmann M, *Ehses P*, Schweimer K, Steinert M, Kamphausen T, Fischer G, Hacker J, Rösch P, Faber C. Domain motions of the Mip protein from Legionella pneumophila. Biochemistry. 2006 Oct 10;45(40):12303-11.

ORAL PRESENTATIONS

- Ott M, Breuer FA, *Ehses P*, Jakob PM, Blaimer M. Cross-solution for robust T2-quantification with phase cycled bSSFP. Proceedings of the ESMRMB 2011, Leipzig. #72.
- *Ehses P*, Gulani V, Breuer FA, Yutzy S, Seiberlich N, Jakob PM, Griswold MA. Parameterquantifizierung mit radialem IR-TrueFISP und Einfluß von Magnetisierungstransfer und finiter Pulslänge. 12. Jahrestagung der Deutschen Sektion der ISMRM (2009), Basel, #V05.
- Lopez MA, *Ehses P*, Breuer FA, Gareis D, Jakob PM. Hole-Slotted Phased Array at 7 Tesla. Proc Intl Soc Mag Reson Med 17 (2009), #109.
- Seiberlich N, *Ehses P*, Breuer FA, Blaimer M, Jakob PM, Griswold MA. Reconstruction of Undersampled Non-Cartesian Data using GROG-Facilitated Random Blipped Phase Encoding. Proc Intl Soc Mag Reson Med 16 (2008), #7.
- Nordbeck P, Weiss I, *Ehses P*, Warmuth M, Fidler F, Jakob PM, Ladd ME, Quick HH, Bauer WR. Measuring RF-Induced Currents inside Implants: Impact of Device Configuration on MRI Safety of Cardiac Pacemaker Leads. Proc Intl Soc Mag Reson Med 16 (2008), #899.
- *Ehses P*, Fidler F, Nordbeck P, Pracht ED, Warmuth M, Jakob PM, Bauer WR. Fast Mapping of RF-Induced Heating Along Conductive Wires by MRI Thermometry. E-poster oral presentation, Proc Intl Soc Mag Reson Med 15 (2007), #735.
- Nordbeck P, Fidler F, Warmuth M, *Ehses P*, Weiss I, Friedrich MT, Geistert W, Jakob PM, Ladd ME, Quick HH, Bauer WR. Hot Spots im MRT: Erwärmung elektrischer Implantate im Körper-Phantom. 73. Jahrestagung der Deutschen Gesellschaft für Kardiologie Herz- und Kreislaufforschung e.V., p. NA.
- *Ehses P*, Fidler F, Bauer WR, Jakob PM. MRI thermometry: fast mapping of rf induced heating in implants. Proceedings of the ESMRMB 2006, Warsaw, #263.

POSTER PRESENTATIONS

- Weick S, *Ehses P*, Blaimer M, Breuer FA, Jakob PM. Improved Retrospective Self-Gated Human Lung Imaging Using a Quasi Random Sampling Scheme. Proc Intl Soc Mag Reson Med 19 (2011), #924.

- Völker M, Breuer FA, *Ehses P*, Triphan SM, Blaimer M, Jakob PM. Fast T2 Mapping of the Lung Within One Breathhold Using Radial TSE Acquisition and PCA Aided Image Reconstruction. Proc Intl Soc Mag Reson Med 19 (2011), #934.
- *Ehses P*, Helluy X, Völker M, Gulani V, Seiberlich N, Griswold MA, Jakob PM, Breuer FA. Improved Single-shot MR Relaxometry using Principal Component Analysis. Proc Intl Soc Mag Reson Med 19 (2011), #2738.
- Seiberlich N, Ma D, *Ehses P*, Gulani V, Griswold MA. Orthogonal Matching Pursuit for Improved Relaxation Parameter Estimation. Proc Intl Soc Mag Reson Med 19 (2011), #2742.
- Cao Z, Sica CT, *Ehses P*, Oh S, Ryu YC, Collins CM, Griswold MA. Phase Constrained Compressed Sensing with Applications for PRF Temperature Mapping. Proc Intl Soc Mag Reson Med 19 (2011), #2842.
- Hoffmann F, *Ehses P*, Völker M, Breuer FA, Blaimer M, Jakob PM. Improved Through Slice Resolution in Continuously Moving Table MRI by Using a Modified Helical Trajectory. Proc Intl Soc Mag Reson Med 19 (2011), #4361.
- Breuer FA, A. Fischer A, N. Seiberlich N, *Ehses P*, Blaimer M, Neumann D, Jakob PM, Griswold MA. Improved Compressed Sensing Reconstruction in Dynamic Contrast Enhanced MR Angiography by Means of Principal Component Analysis (PCA). Proc Intl Soc Mag Reson Med 19 (2011), #4379.
- Seiberlich N, Lee G, *Ehses P*, Duerk JL, Griswold MA. Through-Time Spiral GRAPPA for Real-Time Cardiac Imaging. Proc Intl Soc Mag Reson Med 19 (2011), #4392.
- Choli M, Blaimer M, Breuer FA, *Ehses P*, Bartsch AJ, Jakob PM. SAR reduced neuro-imaging using TSE-EPI hybrid sequence at 3 T. Proceedings of the ESMRMB 2011, Leipzig, #619.
- Hopfgartner AJ, Tymofiyeva O, *Ehses P*, Rottner K, Boldt J, Richter EJ, Jakob PM. Real-Time Imaging of the Temporomanibular Joint Motion Based on Golden Ratio Radial MRI. Proc Intl Soc Mag Reson Med 18 (2010), #895.
- Völker M, *Ehses P*, Blaimer M, Breuer FA, Jakob PM. High Resolution T2 Weighted Lung Imaging with a Radial Turbo Spin-Echo Sequence. Proc Intl Soc Mag Reson Med 18 (2010), #2509.
- Triphan S, *Ehses P*, Blaimer M, Kreutner J, Breuer FA, Jakob PM. Fast, High Resolution T1-Mapping of the Human Lung Using an Inversion Recovery Radial Golden Angle Acquisition. Proc Intl Soc Mag Reson Med 18 (2010), #2517.

- Weick S, *Ehses P*, Blaimer M, Breuer FA, Jakob PM. DC Gated High Resolution 3D MRI of the Human Lung Under Free Breathing. Proc Intl Soc Mag Reson Med 18 (2010), #2525.
- *Ehses P*, Gulani V, Jakob PM, Griswold MA, Breuer FA. Rapid 3D Relaxation Time and Proton Density Quantification Using a Modified Radial IR TrueFisp Sequence. Proc Intl Soc Mag Reson Med 18 (2010), #2952.
- *Ehses P*, Gulani V, Yutzy SR, Seiberlich N, Jakob PM, Griswold MA. Single-Shot Proton Density, T1 and T2 Quantification with Radial IR TrueFISP: Effect of Magnetization Transfer and Long RF Pulses. Proc Intl Soc Mag Reson Med 18 (2010), #2969.
- Kunth M, Seiberlich N, *Ehses P*, Gulani V, Griswold MA. Improvement of Quantitative MRI Using Radial GRAPPA in Conjunction with IR-TrueFISP. Proc Intl Soc Mag Reson Med 18 (2010), #2895.
- Seiberlich N, *Ehses P*, Duerk JL, Gilkeson R, Griswold MA. Application of Hybrid Through-Time/k-Space Radial GRAPPA Calibration to Real-Time Cardiac Imaging. Proc Intl Soc Mag Reson Med 18 (2010), #4904.
- Blaimer M, Fischer A, *Ehses P*, Seiberlich N, Griswold MA, Jakob PM, Breuer FA. Simplified Iterative GRAPPA for fast and robust parallel MRI with arbitrary trajectories. Proc Intl Soc Mag Reson Med 17 (2009), #2713.
- *Ehses P*, Seiberlich N, Blaimer M, Breuer FA, Bauer WR, Jakob PM. Cartesian Quasi-Random Sampling for Multiple Contrasts and Dynamic Imaging. Proc Intl Soc Mag Reson Med 17 (2009), #2625.
- Nordbeck P, Ritter O, Friedrich MT, Maxfield M, Warmuth M, *Ehses P*, Weiss I, Hiller KH, Jakob P, Ladd ME, Quick HH, Bauer WR. Fluoroptic Measurements of MRI-related Heating at Cardiac Pacemaker Leads in Vivo: Initial Results. Proc Intl Soc Mag Reson Med 17 (2009), #4784.
- *Ehses P*, Lopez MA, Friedrich MT, Fidler F, Nordbeck P, Warmuth M, Jakob PM, Bauer WR. 3D MRI thermometry of MR-induced heating of a wire and determination of total generated heat. Proc Intl Soc Mag Reson Med 17 (2009), #4795.
- Breuer FA, Darji N, *Ehses P*, Jakob PM, Blaimer M. Rapid high-resolution relaxation time and spin-density quantification using a modified segmented IR-TrueFisp sequence. Proceedings of the ESMRMB 2009, Antalya, #183.
- Hopfgartner AJ, Tymofiyeva O, *Ehses P*, Rottner K, Boldt J, Richter EJ, Jakob PM. Radial dynamic MRI of the temporomandibular joint. Proceedings of the ESMRMB 2009, Antalya, #630.

- *Ehses P*, Seiberlich N, Nordbeck P, Fidler F, Jakob PM, Bauer WR. Multi-spiral MRI for cardiac T2-star determination. Proc Intl Soc Mag Reson Med 16 (2008), #1015.

- Fidler F, Hippmann T, Warmuth M, *Ehses P*, Nordbeck P, Friedrich MT, Geistert W, Kullmann W, Jakob PM, Bauer WR. MRI safety: Quantitative comparison of RF-heating on different MR scanners based on the high frequency B1-field. Proc Intl Soc Mag Reson Med 16 (2008), #1055.

- Seiberlich N, *Ehses P*, Nielles-Vallespin S, Breuer FA, Blaimer M, Jakob PM, Griswold MA. Self-Calibrating Gridding for 3D Radial Trajectories Using GRAPPA Operator Gridding (GROG). Proc Intl Soc Mag Reson Med 16 (2008), #1281.

- Fidler F, HippmannT, Warmuth M, *Ehses P*, Nordbeck P, Friedrich M, Geistert W, Kullmann W, Jakob PM, Bauer WR. MRI safety: Quantitative comparison of RF-heating on different MR scanners based on the high frequency B1-field. Proceedings of the ESMRMB 2008, Valencia, #811.

- Nordbeck P, Fidler F, Weiss I, Warmuth M, Friedrich MT, *Ehses P*, Geistert W, Jakob PM, Ladd ME, Quick HH, Bauer WR. RF-Induced Electromagnetic Fields and Implant Heating in MRI. Proc Intl Soc Mag Reson Med 15 (2007), #1091.

- Fidler F, Nordbeck P, Warmuth M, *Ehses P*, Hiller KH, Weiss I, Maxfield M, Jakob PM, Bauer WR. MR Safety: Investigation on a worst case implant heating protocol - a simple solution for radio frequency induced heating sequences. Proceedings of the ESMRMB 2006, Warsaw, #723.

DANKSAGUNG

Als erstes möchte ich mich bei meinem Doktorvater Prof. Peter Jakob bedanken, für die Möglichkeit an diesem Lehrstuhl an sehr interessanten Themen zu promovieren und für die stetige Unterstützung, besonders auch bei meinem kurzzeitigen "Ausflug" nach Cleveland. Seine Tür war bei Fragen und Problemen immer offen für mich.

Prof. Wolfgang Bauer danke ich für die Unterstützung und Zusammenarbeit während des BFS-Projektes. Ebenso gilt mein Dank meinen anderen Kollegen im Projekt: Florian Fidler, Peter Nordbeck und Marcus Warmuth sowie den zahlreichen Kooperationspartnern aus Essen und Berlin.

Mark Griswold, Vikas Gulani, Jeff Duerk und Nicole Seiberlich danke ich dafür, dass sie sich sehr dafür eingesetzt haben, dass ich kurzfristig für einige Zeit in ihrer Arbeitsgruppe am Case Center for Imaging Research arbeiten durfte. Außerdem danke ich ihnen für viele anregende Diskussionen, für die gemeinsame Arbeit an spannenden Projekten und für eine tolle Zeit in Cleveland!

Felix Breuer danke ich für die tolle Zusammenarbeit und Betreuung, besonders nach meiner Rückkehr nach Würzburg. Hoffentlich werden wir auch in Zukunft noch Zeit finden gemeinsam an spannenden Projekten zu arbeiten.

Florian Fidler und Eberhard Pracht danke ich dafür, dass sie sich besonders zu Beginn meiner Doktorarbeit viel Zeit für mich genommen haben und mich in die "Geheimnisse" der Sequenzprogrammierung am Vision einweihten.

Besonderer Dank gilt auch Marcos Lopez der mein MR-Hardware-Wissen von Null auf ein bißchen steigern konnte und sogar zwei Spulen extra für mich angefertigt hat!

Ich danke auch meinen zahlreichen Zimmergenossen, mit denen ich in den letzten Jahren wahrscheinlich mehr Zeit verbracht habe als mit sonst jemandem (nach Einzugsdatum): Marcos Lopez, Peter Nordbeck, Marcus Warmuth, Daniel Weber, Nicole Seiberlich, Morwan Choli und Stefan Weick.

Zudem gibt es noch unzählige andere die mich in meiner Zeit bei EP5 unterstützt haben, vielen Dank EP5!

Ganz besonderer Dank gilt meinen Eltern, meiner Schwester Sarah und meinen Freunden. Ohne ihre Unterstützung und ihr großes Verständnis wäre diese Arbeit nicht möglich gewesen.

ERKLÄRUNG

Gemäß §5, Abs. 2, Ziff. 2 und 5

der Promotionsordnung der

Fakultät für Physik und Astronomie der

Universität Würzburg

Hiermit erkläre ich an Eides statt, dass ich die Dissertation eigenständig, d.h. insbesondere selbständig und ohne Hilfe eines kommerziellen Promotionsberaters angefertigt und keine anderen als die von mir angegebenen Quellen und Hilfsmittel verwendet habe.

Die Dissertation wurde bisher weder in gleicher noch in anderer Form in einem anderen Prüfungsfach vorgelegt.

Am 23. Oktober 2005 wurde mir von der Bayerischen Julius-Maximilians-Universität Würzburg der akademische Grad Diplom-Physiker Univ. verliehen. Weitere akademische Grade habe ich weder erworben noch versucht zu erwerben.

Würzburg, den 14. Dezember 2011

Philipp Ehses